STABILITY OF HAPTIC RENDERING FOR DEFORMABLE OBJECTS

Mehrdad Hosseini-Zadeh

A Thesis

in

The Department

of

Electrical and Computer Engineering

Presented in Partial Fulfillment of the Requirements

for the Degree of Master of Applied Science at

Concordia University

Montreal, Quebec, Canada

August 2004

© Mehrdad Hosseini-Zadeh, 2004

Library and Archives Canada

Published Heritage Branch

395 Wellington Street
Ottawa ON K1A 0N4
Canada

Bibliothèque et Archives Canada

Direction du Patrimoine de l'édition

395, rue Wellington
Ottawa ON K1A 0N4
Canada

Your file Votre référence
ISBN: 0-612-94700-9
Our file Notre référence
ISBN: 0-612-94700-9

The author has granted a non-exclusive license allowing the Library and Archives Canada to reproduce, loan, distribute or sell copies of this thesis in microform, paper or electronic formats.

L'auteur a accordé une licence non exclusive permettant à la Bibliothèque et Archives Canada de reproduire, prêter, distribuer ou vendre des copies de cette thèse sous la forme de microfiche/film, de reproduction sur papier ou sur format électronique.

The author retains ownership of the copyright in this thesis. Neither the thesis nor substantial extracts from it may be printed or otherwise reproduced without the author's permission.

L'auteur conserve la propriété du droit d'auteur qui protège cette thèse. Ni la thèse ni des extraits substantiels de celle-ci ne doivent être imprimés ou aturement reproduits sans son autorisation.

In compliance with the Canadian Privacy Act some supporting forms may have been removed from this thesis.

Conformément à la loi canadienne sur la protection de la vie privée, quelques formulaires secondaires ont été enlevés de cette thèse.

While these forms may be included in the document page count, their removal does not represent any loss of content from the thesis.

Bien que ces formulaires aient inclus dans la pagination, il n'y aura aucun contenu manquant.

Canada

ABSTRACT

STABILITY OF HAPTIC RENDERING FOR DEFORMABLE OBJECTS

Mehrdad Hosseini-Zadeh

Stable and robust point-based haptic rendering interaction and sliding with and on various types of deformable elastic objects, ranging from low-stiffness (soft) to high-stiffness (rigid), is one of the main technical challenges in the field of virtual environments and force feedback haptic displays. The methods proposed in this work offer a high-fidelity 3D force reflecting haptic model to guarantee a stable interaction and sliding of deformable objects. Consequently, one is able to maintain a continuous force feedback field over the surface of polygonal-based deformable bodies with different normal stiffnesses in each polygonal mesh. Several control strategies are developed and investigated for maintaining and improving on the stability margins and achievable performances for haptic rendering intended for interacting with virtual deformable objects. Two specific classes of control strategies are investigated in this thesis. The first is a Lead-Lag compensator design based on classical control theory and the second scheme is a Linear-Quadratic-Gaussian (LQG) controller designed according to modern control theory. A detailed comparative evaluation of the proposed control strategies are presented to illustrate the performance of the resulting controlled haptic display when applied to deformable objects.

Dedicated to Fariba

ACKNOWLEDGMENTS

I would like to express my gratitude and appreciation to my advisor Professor Dr. Khashayar Khorasani for all his thoughtful guidance, invaluable assistance, support and encouragement throughout my graduate research at Concordia University. I also thank him for reading and editing my dissertation. I also thank professors Dr. Packirisamy, Dr. Khendek, Dr. Kahrizi and Dr. Wang for serving on my thesis dissertation committee.

Past and present fellow students in Control and Robotic group gave me a pleasant time around the lab. The valuable inputs and helpful discussions from them were much appreciated. I also thank Wojciech in helping me with installing and fixing the required softwares. I also thank Diane, Kathryne and Kim.

I thank my parents for their life time support and I also thank my brothers and sister for their endless inspiration towards my graduate studies. I am very grateful to their supports. I also thank my friend, Sasan, who has helped me proof read my thesis.

I would also like to express my special thanks to my wife, Fariba, and my beautiful daughter, Parastou, for their love, patience and understanding during the hard work of my graduate study.

TABLE OF CONTENTS

LIST OF FIGURES

LIST OF TABLES

Chapter 1

INTRODUCTION

1.1 Preamble

One of the fastest-growing applications in Human Computer Interaction (HCI) field is that of haptic rendering of deformable objects. In this application domain guaranteeing stability and maintaining the highest quality of interaction are among the main challenges for creating a truly realistic interface between the user and the virtual deformable bodies. These issues are rather critical in the case of surgical simulators and training applications. In this thesis, the modeling of deformable objects is studied and the solutions for the problems of interaction and sliding motion with the haptic point (end-effector of the haptic device) are investigated. PHANToM ™ haptic device (model 1.5) developed by SensAble Technologies is used here, as this device is one of the most popular haptic displays that are utilized by researchers in this domain [1].

1.2 Literature Review

Several important techniques for modeling deformable objects in computer graphics and haptics are reviewed. Furthermore, the work in the literature on design and analysis of stable haptic displays in general, and particularly for haptic rendering of deformable objects are surveyed.

1.2.1 Modeling of Deformable Objects in Computer Graphics

The knowledge on the modeling techniques of deformable objects in computer graphics is an essential prior to the study of the haptic displays for deformable objects. Modeling of deformation has a long history in computer graphics for various applications such as animation, surgery training and image analysis. In reference [35] a detailed survey of the modeling of deformable objects in computer graphics is provided. From their point of view, the models are divided into two main categories of non-physical and physically-based models. Non-physical models use geometric techniques that strictly depend on the skill of the designer to construct the deformable object. Deformation using splines and patches and free-form deformation are among the most well-known technique in this category [35]. In spite of the low-cost of computing and fast rendering of deformation by using non-physical models, these techniques are not suitable for representing the physically-based behavior of force-reflecting deformable objects in most of haptic applications. As discussed in the next section, a technique [39] is presented that certain non-physical models for rendering the physically-based behavior of deformable objects. Consequently, most of the physically based models are considered for rendering in the force feedback applications. Physically-based models utilize physical principles to compute the deformation of objects. Furthermore, the physically-based models are classified into two categories: mass-spring and continuum models. In mass-spring modeling, the deformable object is considered as a lattice of masses connected by springs and dampers. The Newton's second law is employed to define the motion of a single mass due to the applied forces. The equations of the motion for the surface deformations are collected from the motions of all the mass points in the mass-spring-damper network. Modeling the various behaviors of deformable objects is easy to accomplish using mass-spring models with linear and nonlinear springs. However, the difficulties with modeling different material characteristics and the major approximations of the deformation as compared to the actual (continuous) deformable

objects are the drawbacks of this type of deformable modeling. A detailed discussion and overview of various applications of modeling deformable objects using the mass-spring approach are presented in [35].

Continuum models, on the other hand are based on a system of equations that are related to the displacements and forces of a discrete set of points of an object. To solve the continuum mechanical equations for the object, the equations are determined using computational methods and physical principles governing a continuum domain in defining the continuum equations. The reader is referred to [36] for more detail about definition of several engineering materials to predict the mechanical behavior of a variety of real materials for a range of deformation. Two of the most common methods for constructing continuum models are Finite Element Method (FEM) and Boundary Element Method (BEM). Finite element method approximates the continuum equations over the domain, but the boundary element method only approximates the boundary conditions. On the other hand, the boundary element method can not directly handle the nonlinear deformation of the object [37]. Many results are available in the literature for modeling of deformable objects using FEM [9],[12]. Also, the authors in [38] have utilized the boundary element method to offer an accurate rendering of a deformable object.

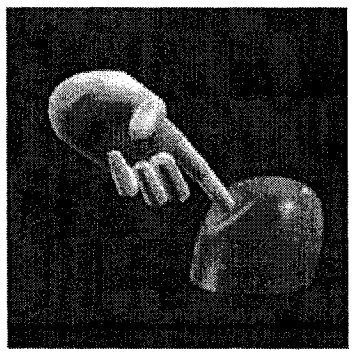

Figure 1.1: Deformable Object in computer graphics [38]

1.2.2 Haptic Display of Deformable Objects

To develop a suitable haptic display for interacting with deformable objects not only the properties for the rigid object like position, geometry, texture and surface frictions [4],[8] should be described, but also the kind of object material should be taken into account. There are various methods for creating geometry of the virtual deformable objects to make the haptic and graphics rendering realistic. In reference [39] similar to that of [35] the authors have categorized the modeling of deformable objects into geometric-based and physically-based deformation models. The geometric-based method is divided into spline-based and vertex-based and the physically-based method is divided into Finite Element Method and Particle-based deformation models. They have also suggested defining a force interaction model for the geometric-based models to solve the problem with lack of physical behaviors of force-reflecting deformable objects. The direction and magnitude of the force vector is computed and is reflected to the user. In physically-based modeling, the model automatically computes the magnitude and direction of the forces applied to each node. Furthermore, the finite element method and its variants are developed and used to display the deformable objects [9]-[12]. The main problem with the finite element based methods is the low-speed rendering. Another approach that has been developed in the literature [13]-[18] uses (pre-calculation) off-line processing of interaction responses with deformable object and use the information for an actual haptic rendering in a real time synthesize. One of the best geometric-based ways to create a virtual object is to use the polygonal mesh. Using this approach, modeling of the object and interaction properties, calculating the force feedback and defining the object texture and material become relatively easy to accomplish. Furthermore, this modeling approach corresponds to

graphics rendering of the scene in many cases [19]-[20]. From a practical perspective, the haptic rendering software of the PHANToM™ haptic devices, known as GHOST API also supports triangular polygons. This software provides the haptic interaction and scene graph support for triangular polygons [7]. In order to achieve a stable interaction Zilles and Salisbury [4] offered a "god-object" approach, which interacts with the haptic device through a virtual couple. In this approach, the virtual couple is modeled as a dashpot and a spring connected in parallel. In addition, the Surface Contact Point (SCP) approach which maintains the contact state and the device end-effector position has also been proposed [4],[7]. In the case of a contact, SCP stays on the surface of the virtual object and the device position point represents the current position of the device end-effector through the object. The displacement between the two points is equal to the deflection in surface of the deformable object on that contact point. This model of interaction is shown in Figure 1.1.

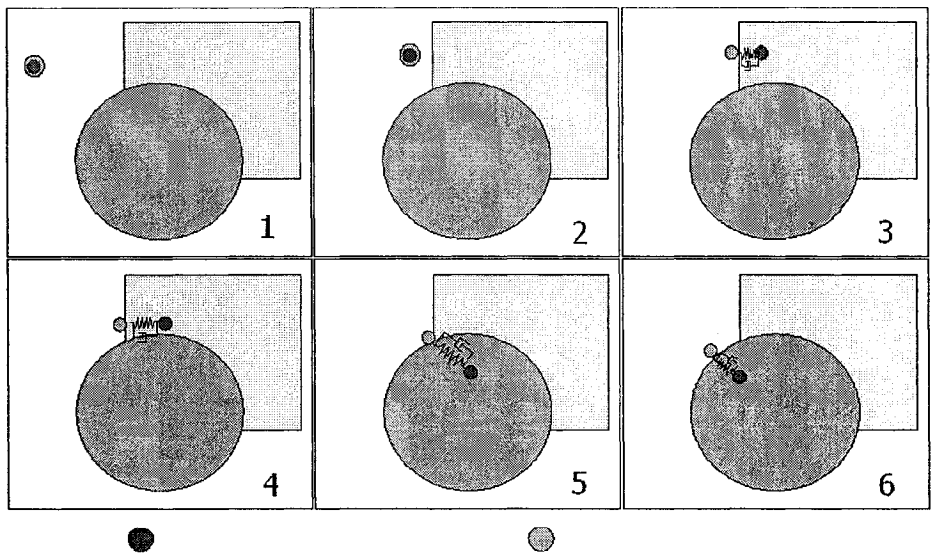

Figure 1.2: The model of interaction with virtual objects in GHOST API. The darker point is the device position and the other point is SCP.

1.2.3 Stability of Haptic Displays

Stability is one of the main issues in force-reflecting control systems. Instability might cause an undesirable feeling to the user and unrealistic interaction with the virtual environment. Stability and achievable performance of a haptic system are among the fundamental indexes for evaluation of a high-precision stable haptic rendering. Many researchers have been working in this field and several approaches have been offered for designing and analyzing the stability properties of haptic displays.

1.2.3.1 Design of Stable Haptic Displays

One of the most important approaches for designing a stable haptic display is passivity-based (energy-based) approach. The extracted energy from the virtual environment can cause unrealistic feelings with severe destabilizing effects. The authors in [26],[27] have used a passivity-based model to design stable haptic displays. They described the design of a virtual wall and the conditions that should be satisfied to ensure a passive haptic display. They also utilized the virtual couple to stabilize the haptic rendering and showed the effects of increasing sampling rate and inherent damping on the passivity. The authors in [28] have used passivity-based model to analyze nonlinear virtual environments. They studied how nonlinear mass/spring/damper virtual environments can be designed to guarantee a stable behavior in the force feedback presented to the user. They considered delayed and non-delayed implementation of the mass/spring/damper virtual environment to discover the behavior of the model with regard to the allowable local stiffness. Overall, the most important aspect of using passivity-based concept comes from the fact that virtual environments are assumed to be passive. Furthermore, the authors in [40]-[43] have employed a two-port network formulation from circuit theory to model the virtual coupling

network. This model is used for both impedance and admittance types of haptic interface and satisfy the conditions for Lewellyn's absolute stability. Finally, the authors in [4] have used a simplified virtual coupling network to design a haptic display to satisfy the passivity conditions for PHANToM ^{TM} haptic device.

A control algorithm was proposed in [29] to avoid instability in a virtual wall. To solve the problem with the zero order hold effect, a half-sample prediction technique and specific digital domain design techniques were proposed. Efficient control algorithms are proposed in [29] to implement stiff virtual walls. They developed an analysis of the complete coupled system comprising controller, interface device, and user's finger to develop an algorithm for the design of a virtual wall to be compatible for specific user impedance. Also, they modeled a typical user's finger as static second order impedance to observe the disparity in time scales between contact instability and volitional control. They used deadbeat control to periodically eliminate the destabilizing effects of asynchronous wall on/off switching times. The authors in [30] have offered a numerical method to reduce the error in force feedback for improving the performance of a haptic display. They focused on one of the important problems in the field of haptic displays and telerobotics as poor force reflection of contact, particularly of contact with stiff surfaces. They expressed the possible sources of poor performance, including poor contact models, sampling errors, and delays due to computation or data transmission. Also, they examined effects due to sample-and-hold, which is a fundamental property of both the discrete domain and also of the sensors and power amplifiers used in a haptic-interface system. They suggested that the sample-and-hold concept be generalized to sample-estimate-hold and presented why ordinary zero-order hold generates an active contact interface, and provided ways of improving the

feeling of the interface. Their numerical method of digitally processing force data improved the performance of haptic presentation of surfaces. There is also some work in the literature in the area of multi-rate haptic rendering. The authors in [31] have investigated the problem arising from the difference between the sampling rate requirements of haptic interfaces and the lower update rates of the physical models. They offered a multi-rate haptic rendering simulation to improve the stability of the haptic interaction with deformable objects using a local linear approximation of the haptic device model. The authors in [46] have proposed a technique that multiple users are able to have stable interaction with a set of deformable slowly-simulated objects. Their technique guarantee the stability of interaction in the case of haptic interaction with slowly simulated virtual environments including the highly precise deformable objects. They stated that the method is particularly useful in case of surgical simulation with force feedback, where precision is a key issue and where complexity can reach high levels. They proposed techniques that are based on the concepts of the local model for haptic interaction that allows multiple users to have a stable interaction with the same object while feeling the influence of other users on that object. Also, they used PHANToM haptic device to simulate their techniques. The authors in [21] have studied the quantitative measurements of the loop gain of a haptic interface for a typical haptic device. Various kinds of traditional classical controllers were also tried to verify the control law performance to improve the stability margin of the closed-loop system. The authors in [22] have designed a compensator to improve the closed loop force bandwidth and stability margin of a haptic device. The authors in [5] have modeled the PHANToM ^{TM} haptic device by studying its mechanical and electrical properties and obtained its kinematics and dynamics representations. Furthermore, they have modified the

device to meet the requirements of achieving a high performance control in some applications. The authors in [33] have utilized a two-port network analysis for a haptic interface in a closed loop force control configuration.

1.2.3.2 Performance Analysis for the Haptic Displays

A number of researchers have considered the problem of analysis of stability of the haptic systems. To analyze the performance of haptic rendering and ensure the quality of the haptic interface, different measurement tools have been suggested in the literature. The authors in [26] have offered Z-Width to address the haptic display performance. Z-Width is the dynamic rang of achievable impedances that can be used as a measure of performance of the haptic display. They have further described some of the contributing parameters on the Z-Width that may consist of inherent interface dynamics, sample and hold, displacement sensor quantization, and velocity filtering. Another performance measurement method suggested in [23] is transparency for a bilateral teleoperation system. This method is also a suitable measurement tool for haptic rendering system. The authors in [25] have used the transparency measures in a teleoperation system. The authors in [32] have used the Lyapunov stability and Routh-Hurwitz criterion to study the limit of stable performance for a haptic manipulator. The authors in [34] have used the Jury stability test to analyze the contact stability of a virtual wall. It was shown that the stability was increased when increasing the sampling rate and increasing the viscous damping friction. Finally, the authors in [24] have detailed the existing performance measures available in the literature for a haptic display. The authors in [48] have suggested the maximum stiffness of the virtual surfaces as one metric of haptic display. With respect to this fact that the PHANToM^{TM} can reflect a maximum stiffness of about 3.5 N/mm, they have found that

most users can be convinced to consider the stiffness of a virtual surface with a stiffness of at least 2 N/mm as a solid and immovable wall. Also, they found that the maximum obtainable stiffness depends not only on the natural frequencies of the device but also on the resolution of the sensors and actuators and the servo rate.

1.3 Thesis Outline

To develop a haptic display system that can work with deformable objects through the PHANToM^{TM} haptic device, in Chapter 2 we first develop a nonlinear model of the haptic device kinematics and dynamics equations of motion along the lines developed in [5]. In Chapter 3 we obtain an experimental linear model of the haptic device by utilizing model-based system identification techniques. An experimental model of the haptic device, consisting of nonlinear kinematics, nonlinear force/torque transformations, virtual object and haptic controllers is developed as a basis for our future investigations of the haptic system. Here our objective is to estimate the device friction (damping) factors and then fix these friction coefficients in the nonlinear model to test the validity of our estimated parameters according to the observed and experimental data. In Chapter 4 with (a) the known friction parameters, (b) the combined nonlinear kinematics and force/torque transformations and (c) the nonlinear device model, an integrated nonlinear model of the system is obtained. Subsequently, this model is then linearized for the purpose of control design. Utilizing two different control strategies position/force feedback linear controllers are designed and their performances are compared when applied to both the linear and the nonlinear haptic device models. Our objective here is to investigate the robustness and the performance capabilities of the purposed algorithms with respect to the changes in the

applied force and deformable object properties and stiffnesses. Finally, in Chapter 5, our objective is to develop a methodology for guaranteeing a stable contact during sliding over the deformable object with discrete normal forces. The conclusions and directions of future research are included in Chapter 6.

1.4 Contributions of the Thesis

The main contributions of the thesis are as follows:

1.4.1 A Suitable Model for Haptic Rendering

To achieve a stable haptic display, a model was presented by adding (and subsequently estimating) friction (damping factors) to the nonlinear open loop model of the haptic device. The response of the system with these damping parameters is shown to converge to the set of equilibrium points of the system and the resulting improved model of the PHANToM^{TM} system guarantee a stable behavior around these equilibrium points. Consequently, the estimated friction coefficients as a set of valid parameters along with the corresponding mathematical nonlinear PHANToM^{TM} model result in appropriate operation of the device under various scenarios.

1.4.2 Stable Interaction with Deformable Objects Having Various Material Properties

It was shown that the model of the system along with the proposed force/position control algorithm can ensure and maintain the desirable forces that are operating subject to interaction with virtual deformable objects with different materials properties (stiffness).

1.4.3 Desirable Performance Results with Sliding on Deformable Object

We have shown that our proposed algorithms and techniques ensure and maintain desirable forces on the deformable object surface and guarantee a stable contact during sliding over the deformable object with discrete normal forces for a typical polygonal mesh deformable object.

Chapter 2

PHANTOM™ PREMIUM 1.5A HAPTIC DEVICE

2.1 Introduction

Haptic devices are mechanical interfaces that establish communication between user and computer in a virtual environment. By using a haptic device, a user is able to touch, feel and manipulate the 3D objects in a virtual environment or a tele-operated system. The user's physical manipulations as input can produce feeling sensations as output. One of the best-known haptic devices is the PHANToM™ made by SensAble Technologies Inc. They developed five distinct models of PHANToM™ device each for a different application. These devices are designed for a vast variety of applications including medical, scientific and industrial. In general, some of the advantages of PHANToM™ devices are their high-fidelity 3D force-feedback, the ability to operate in an office or desktop environment, compatibility with standard PCs and a universal design for a broad range of applications.

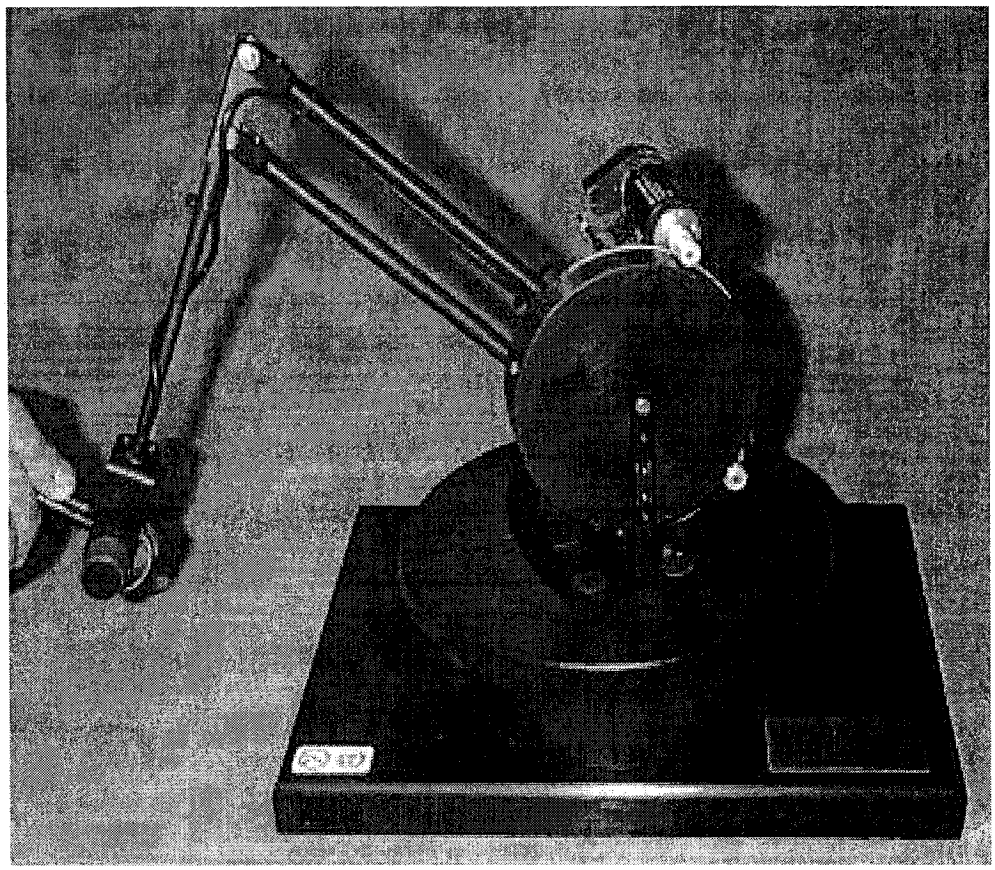

Figure 2.1: PHANToM™ Premium 1.5A Haptic Device [2] .

PHANToM™ Premium 1.5A Haptic Device, shown in Figure 2.1, has a large workspace, suitable for a large range of hand motions, stiffness and motor force to meet the specific requirements of different research projects. The PHANToM™ Haptic interface has a Stylus Grip that is used to grab objects by the user who is in interaction with the virtual environment. This device is connected to a PC through a PCI interface card and there are three degrees of freedom positional measurement system. It supports various platforms including Windows XP, 2000, NT and RedHat Linux 7.2 [1]. Reader is referred to Table

2.1 for more detail about the device specifications. It should be noted that the units in this chapter are in MKS (Meter-Kilogram-Second) unless otherwise specified.

2.2 Kinematics

2.2.1 Forward Kinematics

In this section, position and orientation of the end-effector or Haptic point are shown in terms of joint variables in equilibrium position. The following matrix H represents a conversion from homogeneous coordinates to the Euclidean coordinates.

$$\mathrm{H} = \begin{bmatrix} & 0 \\ I_{3x3} & 0 \\ & 0 \end{bmatrix} \tag{2.1}$$

With reference to Figure 2.2, the following unit vectors of the frame axes and points specify the kinematic configuration of the device [3].

$$w_1 = [0 \quad 1 \quad 0]^{\mathrm{T}} \tag{2.2}$$

$$w_2 = w_3 = [-1 \quad 0 \quad 0]^{\mathrm{T}} \tag{2.3}$$

$$q_1 = [0 \quad 0 \quad -l_1]^{\mathrm{T}} \tag{2.4}$$

$$q_2 = q_3 = [0 \quad l_2 \quad -l_1]^{\mathrm{T}} \tag{2.5}$$

$$\xi_i = \begin{bmatrix} -w_i \times q_i \\ w_i \end{bmatrix}, \ \mathrm{i} = 1,2,3. \tag{2.6}$$

Table 2.1: PHANToM™ Premium 1.5 A specifications [1].

Nominal position resolution	0.03 mm
Workspace	19.5 cm * 27 cm * 37.5 cm
Back drive friction	0.04 N
Maximum exertable force	8.5 N
Continuous exertable force (24 hrs)	1.4 N
Stiffness	3.5 N/mm
Inertia (apparent mass at tip)	< 75 g
Footprint	25 * 33 cm
Force feedback	3 degrees of freedom (x, y, z)
Position sensing	Standard: 3 degrees of freedom (x, y, z) standard with encoder stylus option: 6 degrees of freedom (x, y, z, yaw, pitch, roll)
Minimum System Requirements	
Intel and AMD based PCs	Windows XP, Windows 2000, Windows NT 4.0 SP6, or Red Hat Linux 7.2 300 MHz Pentium processor 64 MB RAM 30 MB free disk space Hardware graphics accelerator

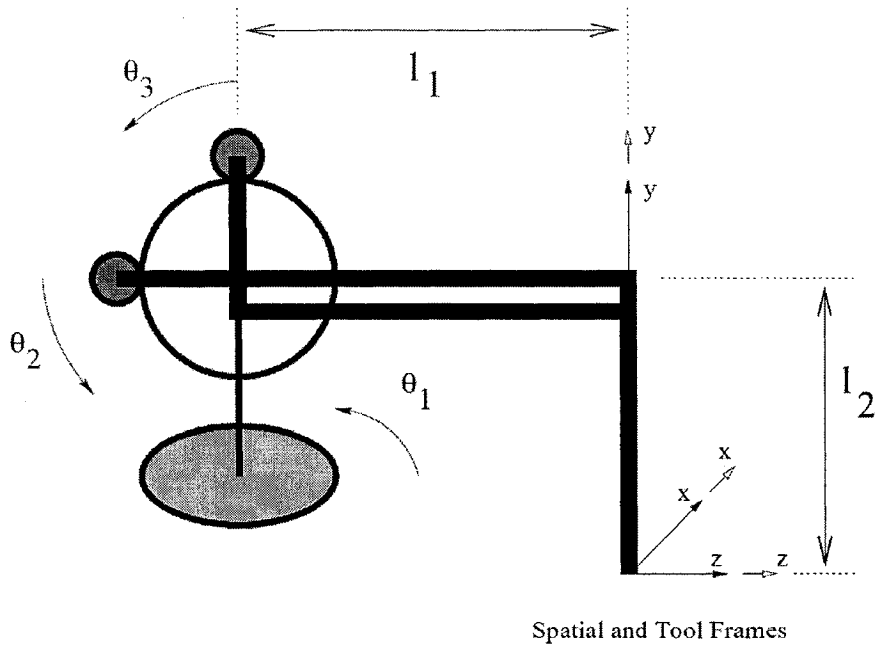

Figure 2.2: The equilibrium position of the device [3].

The homogeneous matrix of the device can be defined by considering a transition vector $p(\theta)$ and a 3x3 rotation matrix $R(\theta)$ to represent the position and orientation of the device (end-effector) with respect to the base frame that, where θ is the joint angular position vector of the device. According to Figure 2.3 that shows the side and top views of the device, the forward kinematic map is represented as

$$g_{st}(\theta) = \begin{bmatrix} R(\theta) & p(\theta) \\ 0\ 0\ 0 & 1 \end{bmatrix} \tag{2.7}$$

where

$$R(\theta) = e^{\hat{w}_1\theta_1} e^{\hat{w}_3\theta_3} I_{3\times 3} \tag{2.8}$$

and

$$p(\theta) = \mathrm{H}\left(e^{\hat{\xi}_1 \theta_1} e^{\hat{\xi}_2 \theta_2} \begin{bmatrix} 1 & 0 & 0 & 0 \\ 0 & 1 & 0 & l_2 \\ 0 & 0 & 1 & 0 \\ 0 & 0 & 0 & 1 \end{bmatrix} \begin{bmatrix} 0 \\ 0 \\ 0 \\ 1 \end{bmatrix} + \begin{bmatrix} R(\theta) \begin{bmatrix} 0 \\ -l_2 \\ 0 \end{bmatrix} \\ 0 \end{bmatrix} \right) \tag{2.9}$$

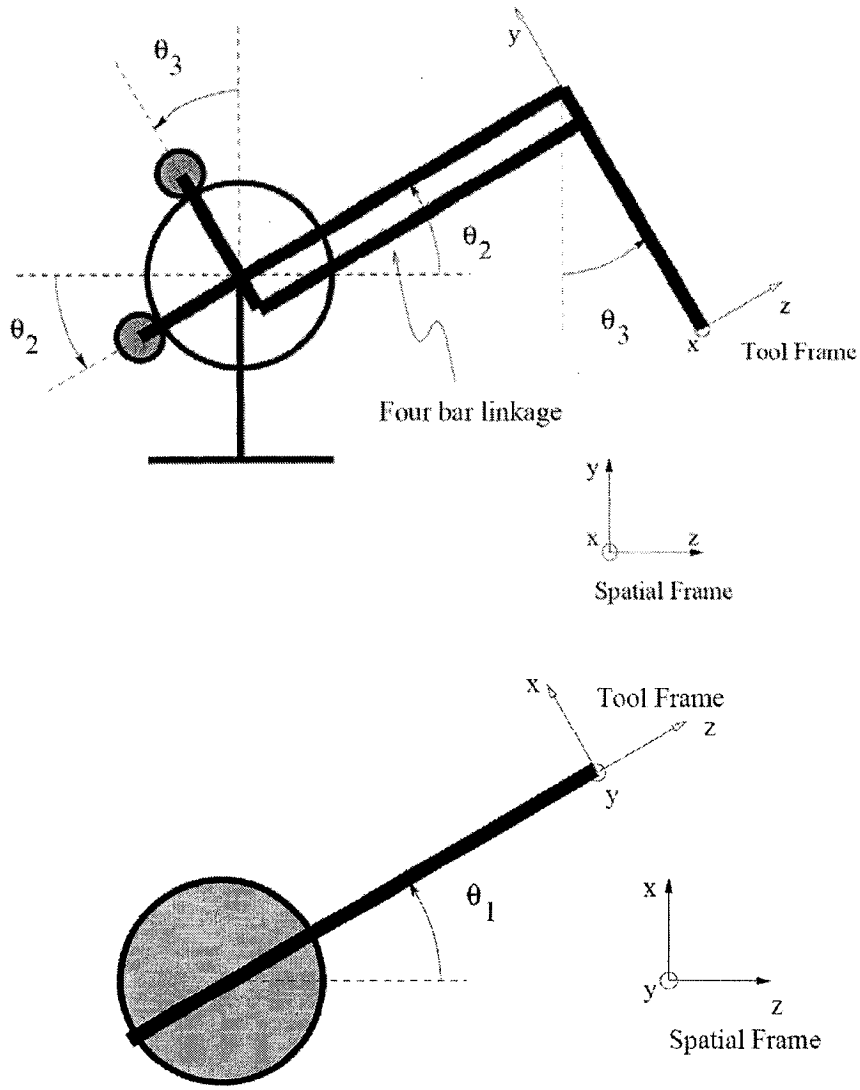

Figure 2.3: Side and top views of the device [3].

According to Figure 2.3, the closed form of the forward kinematics of the device can be given by [3]

$$g_{st}(\theta) =$$

$$\begin{bmatrix} \cos(\theta_1) & -\sin(\theta_1)\sin(\theta_3) & \cos(\theta_3)\sin(\theta_1) & \sin(\theta_1)(l_1\cos(\theta_2)+l_2\sin(\theta_3)) \\ 0 & \cos(\theta_3) & \sin(\theta_3) & l_2 - l_2\cos(\theta_3)+l_1\sin(\theta_2) \\ -\sin(\theta_1) & -\cos(\theta_1)\sin(\theta_3) & \cos(\theta_1)\cos(\theta_3) & -l_1+\cos(\theta_1)(l_1\cos(\theta_2)+l_2\sin(\theta_3)) \\ 0 & 0 & 0 & 1 \end{bmatrix} \quad (2.10)$$

2.2.2 Inverse Kinematics

In this section, we determine the joint variables in terms of position and orientation of the end-effector (Haptic point). Following the specifications provided in Figures 2.3 and 2.4 the equations are obtained as follows [3] :

$$\theta_1 = a\tan 2(p_{0x}, p_{0z} + l_1). \quad (2.11)$$

$$\theta_2 = \gamma + \beta. \quad (2.12)$$

$$\theta_3 = \theta_2 + \alpha - \frac{\pi}{2}. \quad (2.13)$$

where

$$\beta = a\tan 2(p_{0y} - l_2, R), \quad \gamma = \cos^{-1}\left(\frac{l_1^2 + r^2 - l_2^2}{2l_1 r}\right) \quad \text{and} \quad \alpha = \cos^{-1}\left(\frac{l_1^2 + l_2^2 - r^2}{2l_1 l_2}\right).$$

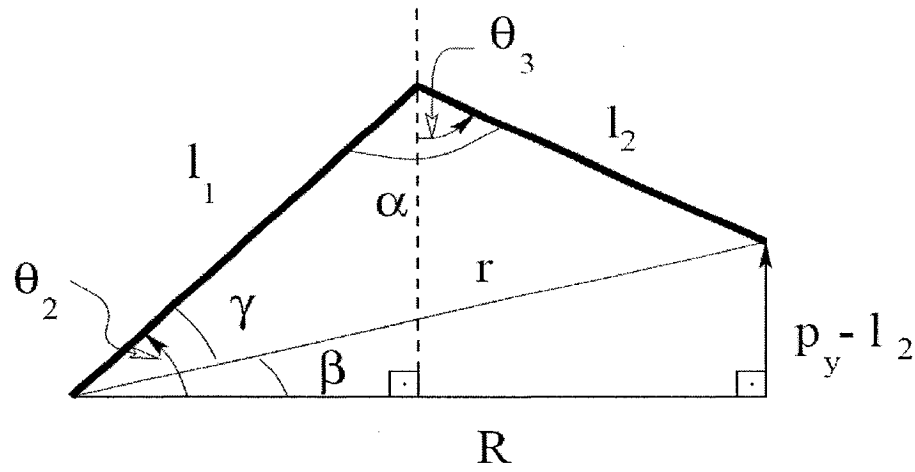

Figure 2.4: Device side view for inverse kinematics calculations [3].

2.3 Manipulator Jacobian

In the previous section, the forward and inverse kinematics of the device was presented to establish the relationship between the end-effector position and orientation and the angular joint positions. In this section, the relationship between the joint velocities and the corresponding end-effector linear and angular velocity is described according to the manipulator Jacobian matrix. The Jacobian matrix will be used for deriving the dynamic equations of motion in the following sections. The relationship between the linear and angular velocities of the end-effector to the joint velocities of the device are governed by the following Jacobian matrix

$$J_0^n = \begin{bmatrix} l_1\cos(\theta_2)+l_2\sin(\theta_3) & 0 & 0 \\ 0 & l_1\cos(\theta_2-\theta_3) & 0 \\ 0 & -l_1\sin(\theta_2-\theta_3) & l_2 \\ 0 & 0 & -1 \\ \cos(\theta_3) & 0 & 0 \\ \sin(\theta_3) & 0 & 0 \end{bmatrix} \tag{2.14}$$

For details refer to [47].

2.4 Dynamics of the Device

Dynamic equations of the device are derived by using the Lagrangian formulation. To analyze the system dynamics, the device is divided into six segments A to G as shown in Figure 2.5. For each segment, or combinations of segments, the rotational and positional vectors of the rigid body transformation between the body and the spatial frames are calculated and the kinetic and potential energies of each segment and the corresponding inertial parameters will be determined. To simplify the calculations, the spatial frame in Figure 2.5 is centered at a point that is different from that in the kinematical analysis. Therefore, the following new points and vectors describe the configuration after changing of coordinate frames.

$$w_1 = [0 \quad 1 \quad 0]^T \tag{2.15}$$

$$w_2 = w_3 = [-1 \quad 0 \quad 0]^T \tag{2.16}$$

$$q_1 = q_2 = q_3 = [0 \quad 0 \quad 0]^T \tag{2.17}$$

$$\xi_i = \begin{bmatrix} -w_i \times q_i \\ w_i \end{bmatrix}, \quad i = 1,2,3 \tag{2.18}$$

It is assumed that each segment material is made of aluminum with a mass density of 1750 kg/m^3 and the actuators/motors are Maxon RE-025-055035. The geometrical parameters of the arms are measured to be

$$l_1 = 0.215 \text{ (M)} \tag{2.19}$$

$$l_2 = 0.170 \text{ (M)} \tag{2.20}$$

$$l_3 = 0.0325 \text{ (M)} \tag{2.21}$$

As stated earlier, in the following subsections, the inertial parameters, the potential and the kinetic energies of the haptic device are presented for each segment. For detailed information refer to [3].

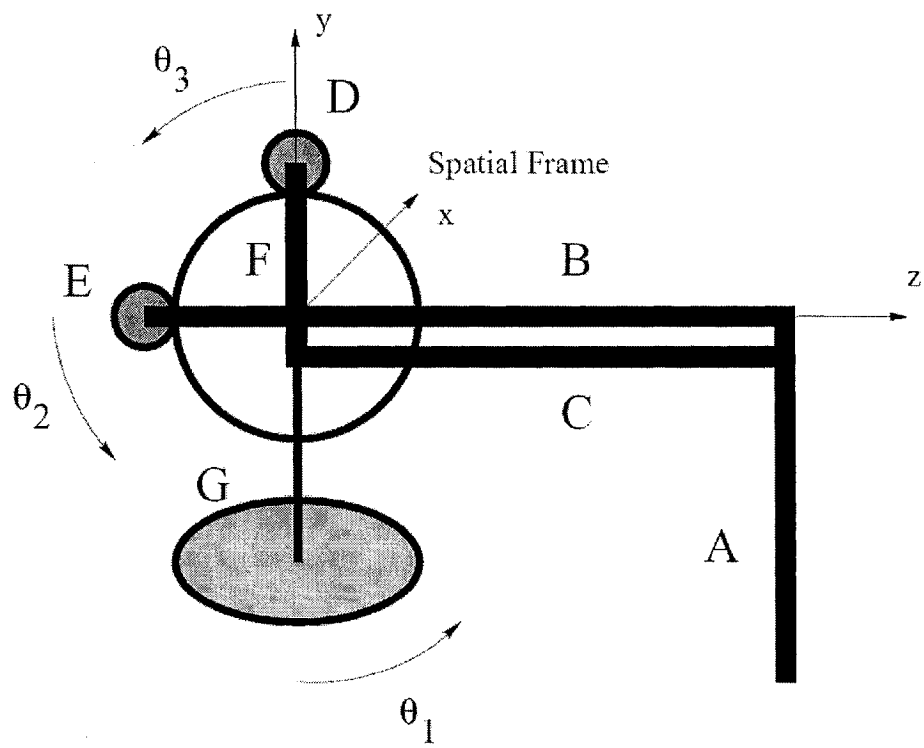

Figure 2.5: Segments A to G of the device for dynamic analysis [3].

2.4.1 Segment A

To obtain the potential and the kinetic energies of the segment A, the rigid body transformation between the body frame of segment A (refer to Figure 2.6) and the spatial frame are given by

$$R_a(\theta) = e^{\hat{w}_1\theta_1} e^{\hat{w}_3\theta_3} I_{3\times 3} \tag{2.22}$$

$$p_a(\theta) = \mathrm{H}\left(e^{\hat{\xi}_1\theta_1} e^{\hat{\xi}_2\theta_2} \begin{bmatrix} 1 & 0 & 0 & 0 \\ 0 & 1 & 0 & 0 \\ 0 & 0 & 1 & l_1 \\ 0 & 0 & 0 & 1 \end{bmatrix} \begin{bmatrix} 0 \\ 0 \\ 0 \\ 1 \end{bmatrix} + \begin{bmatrix} R_a(\theta) \begin{bmatrix} 0 \\ -l_2/2 \\ 0 \end{bmatrix} \\ 0 \end{bmatrix} \right) \tag{2.23}$$

The potential and the kinetic energies of the segment A are given by

$$V_a(\theta) = m_a g p_{ay}(\theta) \tag{2.24}$$

$$T_a(\theta) = \frac{1}{2}(v_a^{sT} M_a v_a^s + w_a^{bT} I_a w_a^b), \tag{2.25}$$

where y in $p_{ay}(\theta)$ denotes the axis of transformation, $M_a = m_a I_{3\times 3}$ and I_a are respectively the translation and rotational inertia matrices and v_a^s and w_a^b are linear and angular velocities.

2.4.1.1 Inertial Parameters of Segment A

The mass of segment A and its rotational inertia matrix are:

$$m_a = 0.0202 \text{ (Kg)} \tag{2.27}$$

$$I_a = \begin{bmatrix} I_{axx} & 0 & 0 \\ 0 & I_{ayy} & 0 \\ 0 & 0 & I_{azz} \end{bmatrix} \tag{2.28}$$

$$I_{axx} = 0.4864\times 10^{-4},\ I_{ayy} = 0.001843\times 10^{-4},\ I_{azz} = 0.4864\times 10^{-4} \text{ (Kg. M}^2\text{)} \tag{2.29}$$

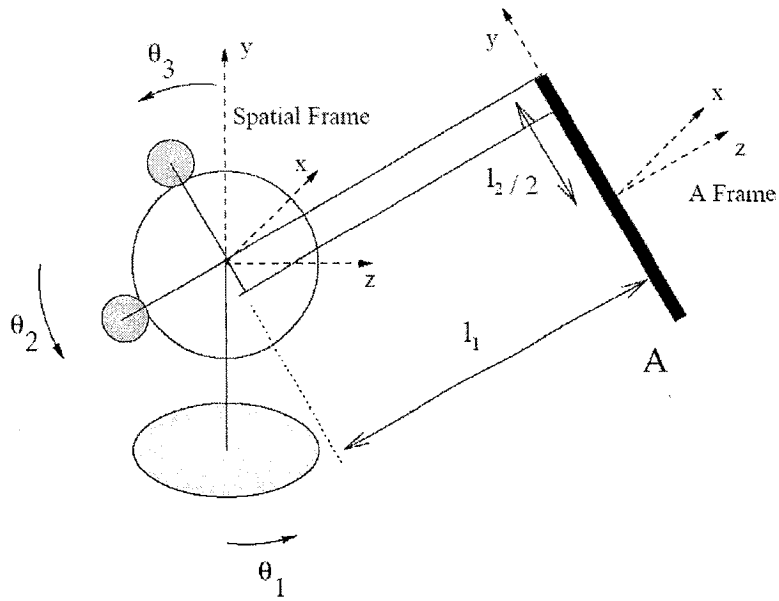

Figure 2.6: Segment A [3].

2.4.2 Segment C

To obtain the potential and kinetic energies of the segment C, the rigid body transformation between the body frame of segment C (refer to Figure 2.7) and the spatial frame are given by

$$R_c(\theta) = e^{\hat{w}_1\theta_1} e^{\hat{w}_3\theta_2} I_{3\times 3} \tag{2.30}$$

$$p_c(\theta) = \mathrm{H}\left(e^{\hat{\xi}_1\theta_1} e^{\hat{\xi}_2\theta_3} \begin{bmatrix} 1 & 0 & 0 & 0 \\ 0 & 1 & 0 & -l_3 \\ 0 & 0 & 1 & 0 \\ 0 & 0 & 0 & 1 \end{bmatrix} \begin{bmatrix} 0 \\ 0 \\ 0 \\ 1 \end{bmatrix} + \begin{bmatrix} R_c(\theta) \begin{bmatrix} 0 \\ 0 \\ -l_1/2 \end{bmatrix} \\ 0 \end{bmatrix} \right) \tag{2.31}$$

The potential and the kinetic energies of the segment C are given by

$$V_c(\theta) = m_c g p_{cy}(\theta) \tag{2.32}$$

$$T_c(\theta) = \frac{1}{2}(v_c^{sT} M_c v_c^s + w_c^{bT} I_c w_c^b), \tag{2.33}$$

where y in $p_{cy}(\theta)$ denotes the axis of transformation, $M_c = m_c I_{3\times3}$ and I_c are the translation and rotational inertia matrices, respectively and v_c^s and w_c^b are the linear and the angular velocities.

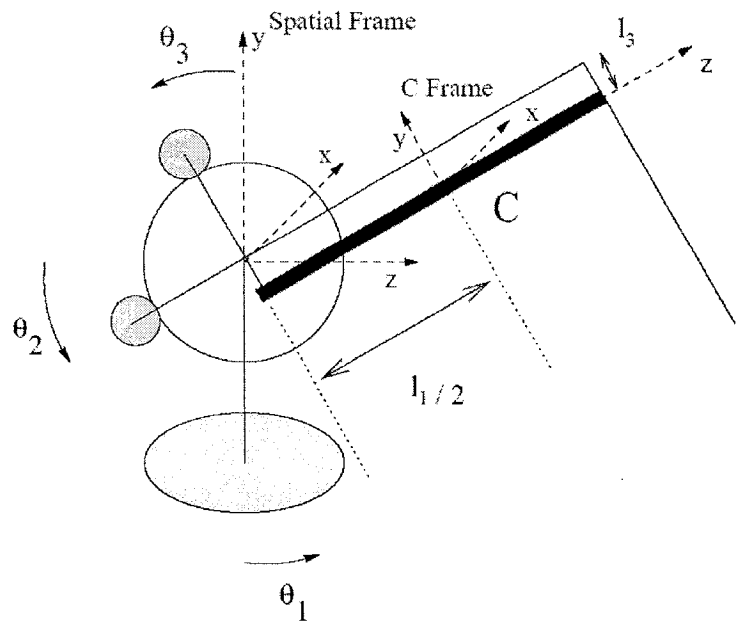

Figure 2.7: Segment C [3].

2.4.2.1 Inertial Parameters for Segment C

The mass of segment C and its rotational inertia matrix are given by

$$m_c = 0.0249 \text{ (Kg)} \tag{2.36}$$

$$I_c = \begin{bmatrix} I_{cxx} & 0 & 0 \\ 0 & I_{cyy} & 0 \\ 0 & 0 & I_{czz} \end{bmatrix} \tag{2.37}$$

$$I_{cxx} = 0.959 \times 10^{-4}, I_{cyy} = 0.959 \times 10^{-4} I_{czz} = 0.0051 \times 10^{-4} \text{ (Kg. M}^2\text{)} \tag{2.38}$$

2.4.3 Segments BE

To obtain the potential and kinetic energies of the segment BE, the rigid body transformation between the body frame of segment BE (refer to Figure 2.8) and the spatial frame are given by

$$R_{be}(\theta) = e^{\hat{w}_1 \theta_1} e^{\hat{w}_2 \theta_2} I_{3\times3} \tag{2.39}$$

$$p_{be}(\theta) = 0 \tag{2.40}$$

The potential and the kinetic energies of the segments BE are given by

$$V_{be}(\theta) = m_{be} g \sin(\theta_2) l_5 \tag{2.41}$$

$$T_{be}(\theta) = \frac{1}{2}(w_{be}^{bT} I_{be} w_{be}^{b}), \tag{2.42}$$

where m_{be} is the mass of segment BE, I_{be} is its rotational inertia matrix and w_{be}^{b} is the angular velocity.

2.4.3.1 Inertial Parameters for Segments BE

The mass of segments BE and its rotational inertia matrix are given by

$$m_{be} = 0.2359 \text{ (Kg)} \tag{2.44}$$

$$I_{be} = \begin{bmatrix} I_{bexx} & 0 & 0 \\ 0 & I_{beyy} & 0 \\ 0 & 0 & I_{bezz} \end{bmatrix} \tag{2.45}$$

$$I_{bexx} = 11.09 \times 10^{-4},\ I_{beyy} = 10.06 \times 10^{-4},\ I_{bezz} = 0.591 \times 10^{-4} \text{ (Kg. M}^2\text{)} \tag{2.46}$$

The location of the center of mass of the segments BE is calculated as

$$l_5 = -36.8(mm) \tag{2.47}$$

2.4.4 Segments D and F

To obtain the potential and kinetic energies of the segment DF, the rigid body transformation between the body frame of segment DF (refer to Figure 2.9) and the spatial frame are given by

$$R_{df}(\theta) = e^{\hat{w}_1 \theta_1} e^{\hat{w}_3 \theta_3} I_{3\times 3} \tag{2.48}$$

$$p_{df}(\theta) = 0 \tag{2.49}$$

The potential and the kinetic energies of the segment DF are given by

$$V_{df}(\theta) = m_{df} g \cos(\theta_3) l_6 \tag{2.50}$$

$$T_{df}(\theta) = \frac{1}{2}(w_{df}^{bT} I_{df} w_{df}^{b}), \tag{2.51}$$

where I_{df} is rotational inertia matrix and w_{df}^{b} is the angular velocity.

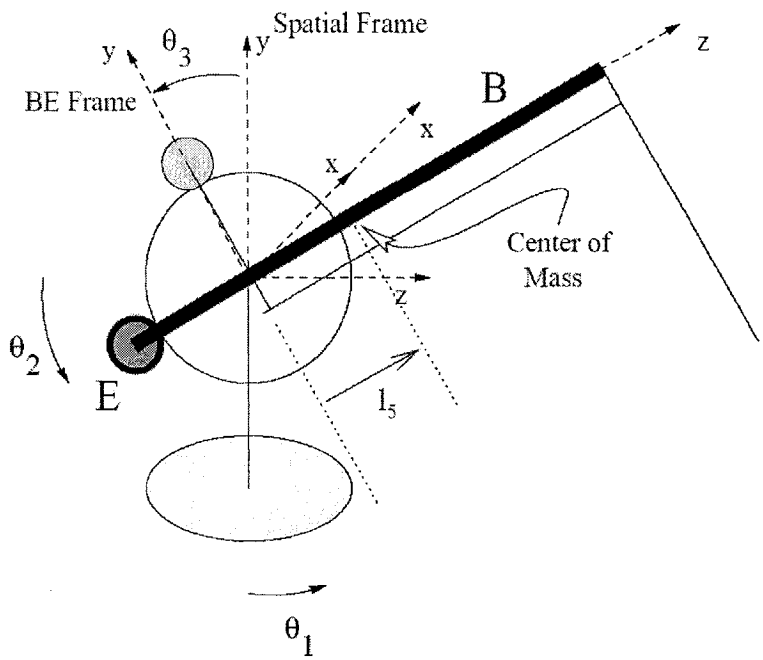

Figure 2.8: Segments BE [3].

2.4.4.1 Inertial Parameters for Segments D and F

The mass of segment DF and its rotational inertia matrix are given by

$$m_{df} = 0.1906 \text{ (Kg)} \tag{2.53}$$

$$I_{df} = \begin{bmatrix} I_{dfxx} & 0 & 0 \\ 0 & I_{dfyy} & 0 \\ 0 & 0 & I_{dfzz} \end{bmatrix} \tag{2.54}$$

$$I_{dfxx} = 7.11\times10^{-4},\ I_{dfyy} = 0.629\times10^{-4},\ I_{dfzz} = 6.246\times10^{-4}\ (\text{Kg. M}^2) \tag{2.55}$$

The center of mass location for segment DF is calculated as

$$l_6 = 52.7(mm) \tag{2.56}$$

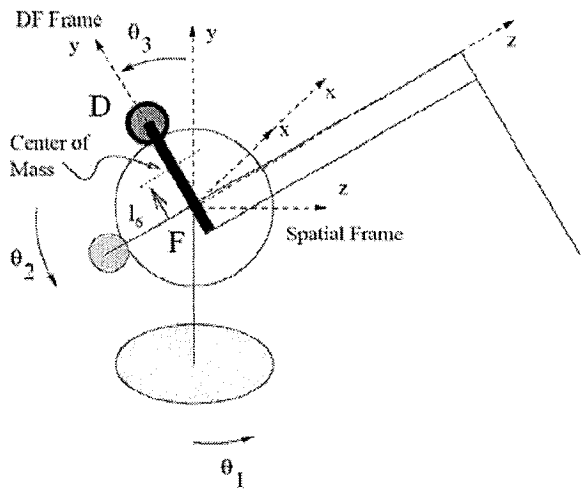

Figure 2.9: Segments D and F [3].

2.4.5 Segment G – the Base

The potential energy of base (refer to Figure 2.2) is zero, and its kinetic energy is given by

$$V_{base} = \frac{1}{2}\dot{\theta}_1 I_{baseyy}\dot{\theta}_1 \tag{2.57}$$

where I_{baseyy} is the rotational inertia matrix.

2.4.5.1 Inertial Parameters for Segment G

Only the rotational inertia matrix should be calculated which is given as

$$I_{baseyy} = 11.87 \times 10^{-4} \text{ (Kg. M}^2\text{)} \tag{2.58}$$

2.5 Dynamic Equations of Motion

The Lagrange equation for the device is expressed [3] as

$$L = T - V$$

$$= (T_a + T_c + T_{be} + T_{df} + T_{base}) - (V_a + V_c + V_{be} + V_{df} + V_{base}) \tag{2.59}$$

and the resulting dynamic equations are given by

$$\frac{d}{dt}\frac{\partial L}{\partial \dot{\theta}_i} - \frac{\partial L}{\partial \theta_i} = \tau_i, \quad i = 1,2,3. \tag{2.60}$$

or equivalently,

$$\begin{bmatrix} M_{11} & 0 & 0 \\ 0 & M_{22} & M_{23} \\ 0 & M_{32} & M_{33} \end{bmatrix} \begin{bmatrix} \ddot{\theta}_1 \\ \ddot{\theta}_2 \\ \ddot{\theta}_3 \end{bmatrix} + \begin{bmatrix} C_{11} & C_{12} & C_{13} \\ C_{21} & 0 & C_{23} \\ C_{31} & C_{32} & 0 \end{bmatrix} \begin{bmatrix} \dot{\theta}_1 \\ \dot{\theta}_2 \\ \dot{\theta}_3 \end{bmatrix} + \begin{bmatrix} 0 \\ N_2 \\ N_3 \end{bmatrix} = \begin{bmatrix} \tau_1 \\ \tau_2 \\ \tau_3 \end{bmatrix} \tag{2.61}$$

where the joint angles are denoted by $[\theta_1 \theta_2 \theta_3]^T$, the input torques are denoted by $[\tau_1 \tau_2 \tau_3]^T$, the inertia matrix is denoted by M, the centrifugal and Coriolis forces is

denoted by the matrix C and the vector of gravitational forces is denoted by N. The specificc description for the terms in the above dynamical equations are

$$M_{11} = \Big(\tfrac{1}{8}(4I_{ayy} + 4I_{azz} + 8I_{baseyy} + 4I_{beyy} + 4I_{bezz} + 4I_{cyy} + 4I_{czz} + 4I_{dfyy} + 4I_{dfzz} + 4l_1^2 m_a + l_2^2 m_a + l_1^2 m_c + 4l_3^2 m_c) + \tfrac{1}{8}(4I_{beyy} - 4I_{bezz} + 4I_{cyy} - 4I_{czz} + l_1^2(4m_a + m_c))\cos(2\theta_2) + \tfrac{1}{8}(4I_{ayy} - 4I_{azz} + 4I_{dfyy} - 4I_{dfzz} - l_2^2 m_a - 4l_3^2 m_c)\cos(2\theta_3) + l_1(l_2 m_a + l_3 m_c)\cos(\theta_2)\sin(\theta_3)\Big) \quad (2.62)$$

$$M_{22} = \tfrac{1}{4}(4(I_{bexx} + I_{cxx} + l_1^2 m_a) + l_1^2 m_c) \quad (2.63)$$

$$M_{23} = \tfrac{1}{2} l_1 (l_2 m_a + l_3 m_c)\sin(\theta_2 - \theta_3) \quad (2.64)$$

$$M_{32} = \tfrac{1}{2} l_1 (l_2 m_a + l_3 m_c)\sin(\theta_2 - \theta_3) \quad (2.65)$$

$$M_{33} = \tfrac{1}{4}(4I_{axx} + 4I_{dfxx} + l_2^2 m_a + 4l_3^2 m_c) \quad (2.66)$$

$$C_{11} = \tfrac{1}{8}(-2\sin(\theta_2)((4I_{beyy} - 4I_{bezz} + 4I_{cyy} - 4I_{czz} + 4l_1^2 m_a + l_1^2 m_c)\cos(\theta_2) + 2l_1(l_2 m_a + l_3 m_c)\sin(\theta_3))\dot{\theta}_2 + 2\cos(\theta_3)(2l_1(l_2 m_a + l_3 m_c)\cos(\theta_2) + (-4I_{ayy} + 4I_{azz} - 4I_{dfyy} + 4I_{dfzz} + l_2^2 m_a + 4l_3^2 m_c)\sin(\theta_3))\dot{\theta}_3) \quad (2.67)$$

$$C_{12} = -\tfrac{1}{8}((4I_{beyy} - 4I_{bezz} + 4I_{cyy} - 4I_{czz} + l_1^2(4m_a + m_c))\sin(2\theta_2) + 4l_1(l_2 m_a + l_3 m_c)\sin(\theta_2)\sin(\theta_3))\dot{\theta}_1 \quad (2.68)$$

$$C_{13} = -\tfrac{1}{8}(-4l_1(l_2 m_a + l_3 m_c)\cos(\theta_2)\cos(\theta_3) - (-4I_{ayy} + 4I_{azz} - 4I_{dfyy} + 4I_{dfzz} + l_2^2 m_a + 4l_3^2 m_c)\sin(2\theta_3))\dot{\theta}_1 \quad (2.69)$$

$$C_{21} = -C_{12} \quad (2.70)$$

$$C_{23} = \tfrac{1}{2} l_1 (l_2 m_a + l_3 m_c)\cos(\theta_2 - \theta_3)\dot{\theta}_3 \quad (2.71)$$

$$C_{31} = -C_{13} \quad (2.72)$$

$$C_{32} = \tfrac{1}{2} l_1 (l_2 m_a + l_3 m_c) \cos(\theta_2 - \theta_3) \dot{\theta}_2 \tag{2.73}$$

$$N_2 = \tfrac{1}{2} g (2 l_1 m_a + 2 l_5 m_{be} + l_1 m_c) \cos(\theta_2) \tag{2.74}$$

$$N_3 = \tfrac{1}{2} g (l_2 m_a + 2 l_3 m_c - 2 l_6 m_{df}) \sin(\theta_3) \tag{2.75}$$

2.6 Modeling of the Haptic Device

The above representation of the haptic device in configuration space can be expressed equivalently in the state space representation as shown by the following set of equations

$$\dot{x}_1 = x_2 \tag{2.76}$$

$$\dot{x}_2 = -\frac{1}{M_{11}} (C_{11} x_2 + C_{12} x_4 + C_{13} x_6) + \frac{1}{M_{11}} \tau_1 \tag{2.77}$$

$$\dot{x}_3 = x_4 \tag{2.78}$$

$$\dot{x}_4 = -\frac{1}{M_{22} M_{33} - M_{23}^2} (M_{33} (\tau_2 - N_2 - C_{21} x_2 - C_{23} x_6)$$

$$- M_{23} (\tau_3 - N_3 - C_{31} x_2 - C_{32} x_4)) \tag{2.79}$$

$$\dot{x}_5 = x_6 \tag{2.80}$$

$$\dot{x}_6 = -\frac{1}{M_{22} M_{33} - M_{23}^2} (-M_{23} (\tau_2 - N_2 - C_{21} x_2 - C_{23} x_6)$$

$$+ M_{22} (\tau_3 - N_3 - C_{31} x_2 - C_{32} x_4)) \tag{2.81}$$

where $x_1 = \theta_1$, $x_2 = \dot{\theta}_1$, $x_3 = \theta_2$, $x_4 = \dot{\theta}_2$, $x_5 = \theta_3$ and $x_6 = \dot{\theta}_3$, are the states of the haptic system, and M_{ij}, C_{ij} are also re-written in terms of the states $x_1 - x_6$, accordingly.

2.6.1 Nonlinear Analysis

Due to the nonlinear nature of the haptic device model, stability of the equilibrium points of the system should be investigated. To obtain the stationary or the equilibrium points of the model, one has to set the derivatives of the angular positions to zero. However, by setting the derivatives of the angular positions to zero in equations (2.76) – (2.81) in the previous section, one obtains $\tau_1(t) = 0$. This implies that the set $\{\theta_1 = x_1 = \text{constant, and } \dot{\theta}_1 = x_2 = 0\}$ represents the equilibrium set for the first link joint angle. The equilibrium conditions for θ_2 and θ_3 results in the following equations

$$N_2 = \tau_2 = \text{Constant}, \quad \dot{\theta}_2 = x_4 = 0 \tag{2.82}$$

$$N_3 = \tau_3 = \text{Constant}, \quad \dot{\theta}_3 = x_6 = 0 \tag{2.83}$$

By substituting $\tau_2 = 0.01$ and $\tau_3 = 0.01$ corresponding to "very small" torque commands in above equations, the system equilibrium points are obtained as

$$\theta_2 = 2.2305 \text{ (rad)} \quad \text{and} \quad \theta_3 = 3.2776 \text{ (rad)}. \tag{2.84}$$

2.7 Open-Loop Computer Simulation

The Simulink software package is used to simulate the mathematical model presented in the previous section. The block diagram of the system is shown in Figure 2.10 and its Simulink schematic layout is presented in Figure A.1. As it is shown in the layout, there are

three torque inputs and three angular position outputs. The response of the system to the torque inputs given in (2.85) is presented in Figures 2.11 and 2.12 for various sets of initial conditions.

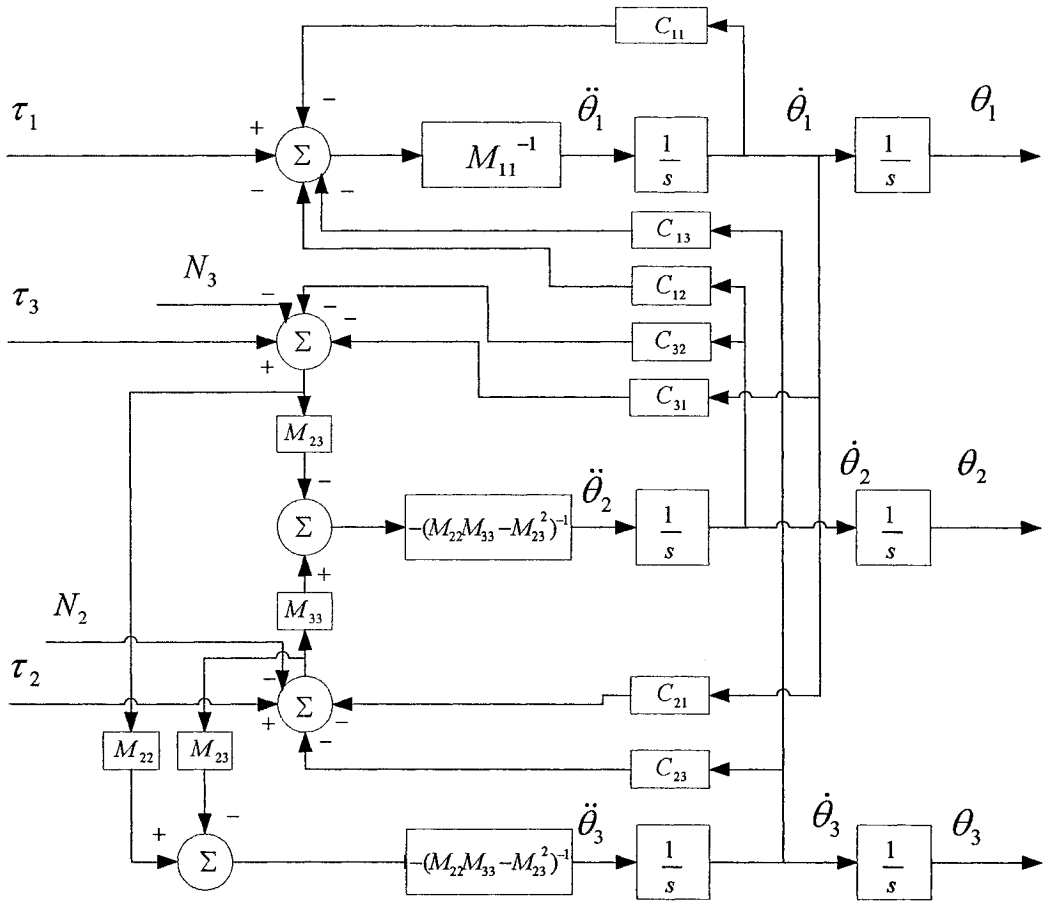

Figure 2.10: Block diagram of the open-loop PHANToM™ haptic device

The angular position outputs of the system presented in Figure 2.11 are based on the input torque commands given in (2.85) and the initial conditions in (2.86) and (2.87).

$$\tau_1 = 0.01(\text{Pulse}); \tau_2 = 0.01;\ \tau_3 = 0.01\ (\text{Nm}) \tag{2.85}$$

$$\dot{\theta}_1(0) = 0;\ \dot{\theta}_2(0) = 0.1;\ \dot{\theta}_3(0) = 0.1 \text{ (rad/s)} \tag{2.86}$$

$$\theta_1(0) = 1;\ \theta_2(0) = 1;\ \theta_3(0) = 1 \text{ (rad)} \tag{2.87}$$

It is obvious from Figure 2.11 that the system outputs (joint angular positions) are unstable and approach to infinity for even a very small value of the applied torques. In the second case, the initial conditions are selected very close to the equilibrium points with the same input torque commands given in (2.85):

$$\dot{\theta}_1(0) = 0;\ \dot{\theta}_2(0) = 0.1;\ \dot{\theta}_3(0) = 0.1 \text{ (rad/s)} \tag{2.88}$$

$$\theta_1(0) = 1;\ \theta_2(0) = 3;\ \theta_3(0) = 4 \text{ (rad)} \tag{2.89}$$

It is again obvious from Figure 2.12 that the system outputs (joint angular positions) do not tend to the system equilibrium points given in the previous section.

Consequently, we can conclude that open-loop haptic device has an unstable equilibrium points (sets). This conclusion may also be verified by performing a Taylor's series expansion of the nonlinear dynamics of the system to obtain a linear time invariant (LTI) state space model of the haptic device. It is shown in the Figure 2.13 that some of the eigen values of the open loop system are in the right half plane or on imaginary axis, implying that the system is unstable.

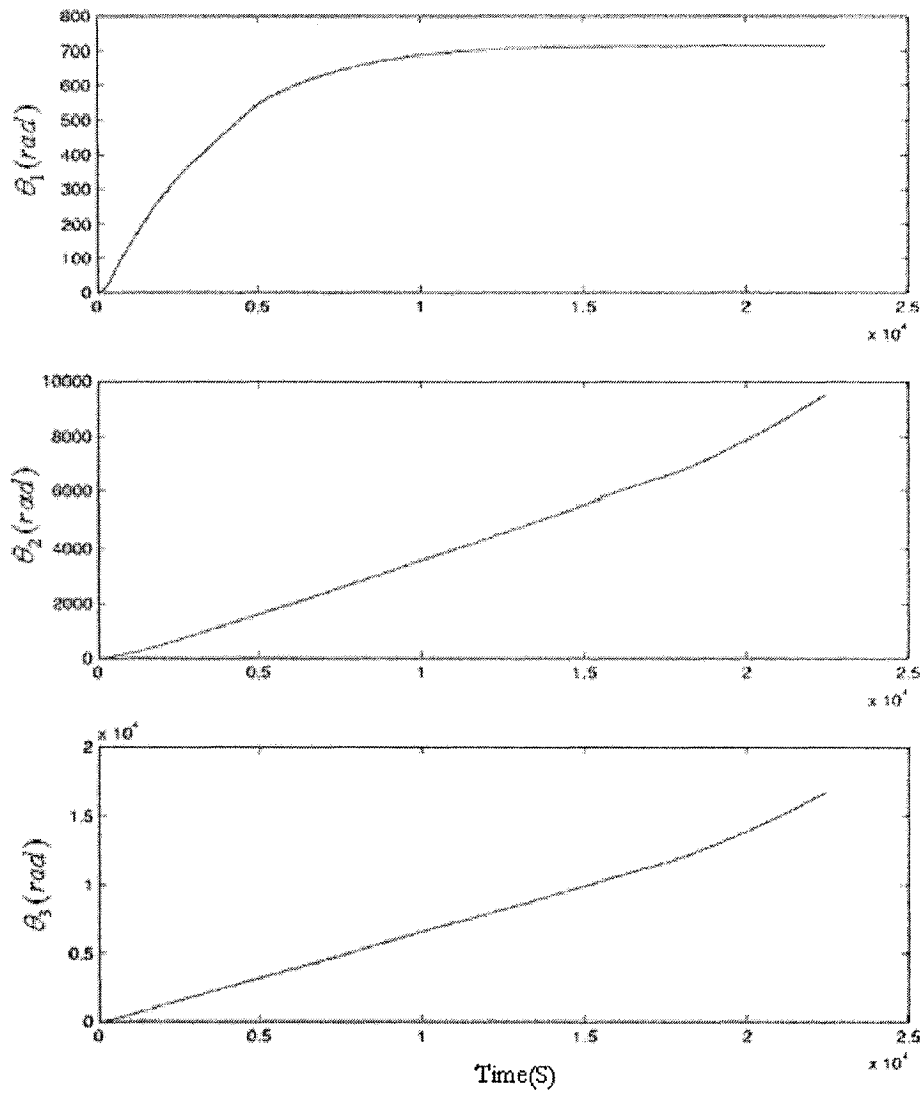

Figure 2.11: Haptic device response to the torques given in (2.85) and the initial condition given in (2.86) and (2.87).

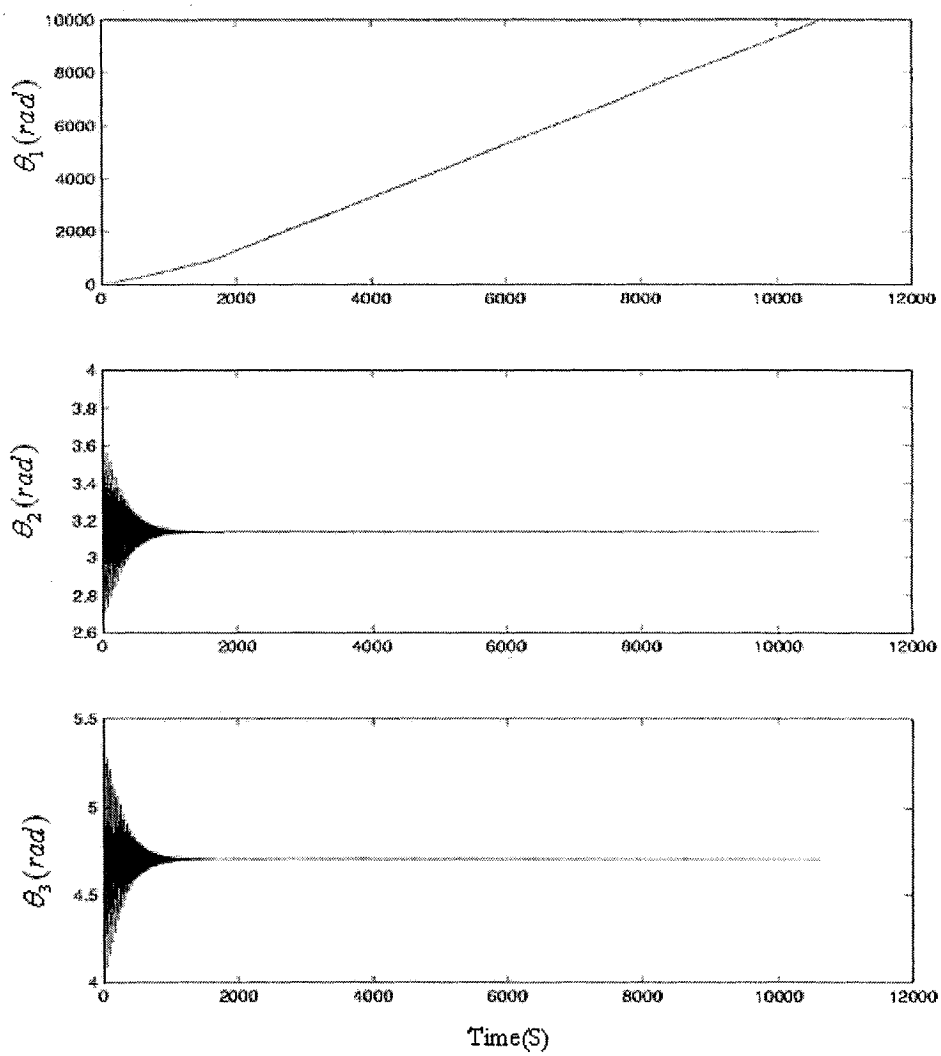

Figure 2.12: Haptic device response to the torques given in (2.85) and the initial conditions given in (2.88), (2.89).

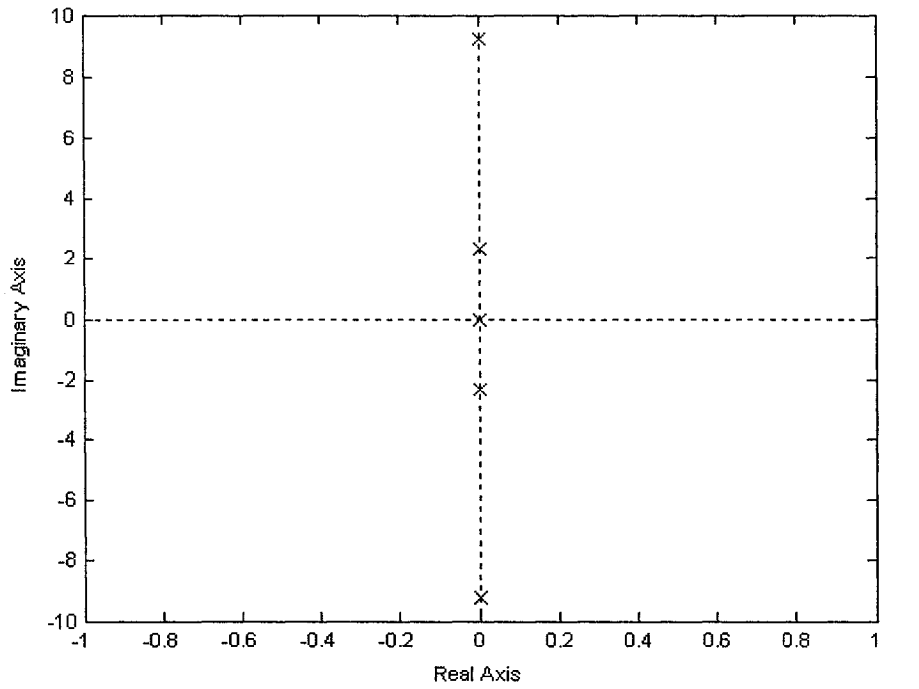

Figure 2.13: The eigen values of the open-loop system

2.8 Conclusions

In this Chapter, the PHANToM^{TM} Premium 1.5A haptic device was considered. In order to analyze, study and evaluate the performance and behavior of the device both the kinematics and dynamics equations of the motion were obtained and nonlinear state space and configurations space models were developed. The open loop system response of the device with different sets of initial conditions was presented. It was concluded that the system responses are unbounded and consequently the trajectories of the haptic device do not approach to its equilibrium points. In the next Chapter, a closed loop model of the haptic device will be presented by incorporating friction (damping factors) to the model through rate feedback control.

Chapter 3

MODELING OF THE HAPTIC SYSTEM WITH FRICTION

3.1 Introduction

According to the results obtained in the previous chapter, the system response is not bounded for the model that was developed. In this chapter, in order to accomplish a bounded and stable response, three friction (damping) parameters are added to the nonlinear open loop model of the haptic device by incorporating an effective rate feedback control. An experimental linear model of the device is also obtained by utilizing system identification techniques. The haptic system model considered here consists of three inputs and three outputs. The resulting haptic system model contains an experimental linear model of the haptic device, nonlinear kinematics, nonlinear force/torque transformations, virtual objects and haptic controllers. The device friction (damping) factors are first estimated experimentally and the resulting friction coefficients are fixed in the nonlinear model to test the validity of these estimated parameters. The behavior of the system with corresponding damping parameters will be analyzed in this Chapter. Furthermore, the system stability is also investigated with respect to a set of equilibrium points. Furthermore, various possible configurations for modeling of the haptic system using both mathematical and experimental linear models are proposed and discussed. This set of various modeling assumptions will be examined subject to different controllers in next chapter.

3.2 Equations of Motion with Friction Factors

Below we have added three damping parameters to the nonlinear model in (2.61) to obtain a model that is closer to an actual device. The revised model is then given by

$$\begin{bmatrix} M_{11} & 0 & 0 \\ 0 & M_{22} & M_{23} \\ 0 & M_{32} & M_{33} \end{bmatrix} \begin{bmatrix} \ddot{\theta}_1 \\ \ddot{\theta}_2 \\ \ddot{\theta}_3 \end{bmatrix} + \begin{bmatrix} C_{11}+k_1 & C_{12} & C_{13} \\ C_{21} & k_2 & C_{23} \\ C_{31} & C_{32} & k_3 \end{bmatrix} \begin{bmatrix} \dot{\theta}_1 \\ \dot{\theta}_2 \\ \dot{\theta}_3 \end{bmatrix} + \begin{bmatrix} 0 \\ N_2 \\ N_3 \end{bmatrix} = \begin{bmatrix} \tau_1 \\ \tau_2 \\ \tau_3 \end{bmatrix} \tag{3.1}$$

where k_1, k_2 and k_3 are the damping coefficients/terms that are added to the open-loop model of the system. This in effect corresponds to adding rate feedback control laws for the control commands τ_1 - τ_3.

3.3 Modeling of the Haptic Device with Friction Factors

The representation of the haptic device given in (3.1) is in configuration space which can be expressed equivalently in the state space representation as shown in the following set of equations

$$\dot{x}_1 = x_2 \tag{3.2}$$

$$\dot{x}_2 = -\frac{1}{M_{11}}(C_{11}x_2 + C_{12}x_4 + C_{13}x_6) + \frac{1}{M_{11}}(\tau_1 - k_1 x_2) \tag{3.3}$$

$$\dot{x}_3 = x_4 \tag{3.4}$$

$$\dot{x}_4 = -\frac{1}{M_{22}M_{33} - M_{23}^2}(M_{33}((\tau_2 - k_2 x_4) - N_2 - C_{21}x_2 - C_{23}x_6)$$

$$-M_{23}((\tau_3 - k_3 x_6) - N_3 - C_{31} x_2 - C_{32} x_4)) \tag{3.5}$$

$$\dot{x}_5 = x_6 \tag{3.6}$$

$$\dot{x}_6 = -\frac{1}{M_{22}M_{33} - M_{23}^2}(-M_{23}((\tau_2 - k_2 x_4) - N_2 - C_{21} x_2 - C_{23} x_6)$$

$$+M_{22}((\tau_3 - k_3 x_6) - N_3 - C_{31} x_2 - C_{32} x_4)) \tag{3.7}$$

where $x_1 = \theta_1$, $x_2 = \dot{\theta}_1$, $x_3 = \theta_2$, $x_4 = \dot{\theta}_2$, $x_5 = \theta_3$ and $x_6 = \dot{\theta}_3$, are the states of the haptic system, and M_{ij}, C_{ij} are also re-written in terms of the states x_1 *to* x_6, accordingly.

3.4 Schematic Layout of the Haptic Device with Friction Factors

The block diagram of the system with friction (damping) parameters based on the equations given in the previous section is shown in Figure 3.1 and its Simulink schematic layout is shown in Figure A.2. The three damping parameters k_1, k_2 and k_3 are added to the open loop model as in the previous section.

3.5 Linearization of the Parametric Nonlinear Haptic Device Model

A multivariable discrete-time linear model is now developed which would clearly determine the order and pure time-delay of the system. Also the linear model of the haptic device should be associated to the nonlinear system developed in the previous section. First, a standard Taylor's series linearization approach is applied to this model corresponding to the input torque commands as $\tau_1 = 0.01, \tau_2 = 0.01$ and $\tau_3 = 0.01$, and a corresponding set of equilibrium points as given by

$$\theta_2 = 2.2305 \text{ (rad)} \quad , \quad \theta_3 = 3.2776 \text{ (rad)} \tag{3.8}$$

where θ_1 can be taken as any constant value.

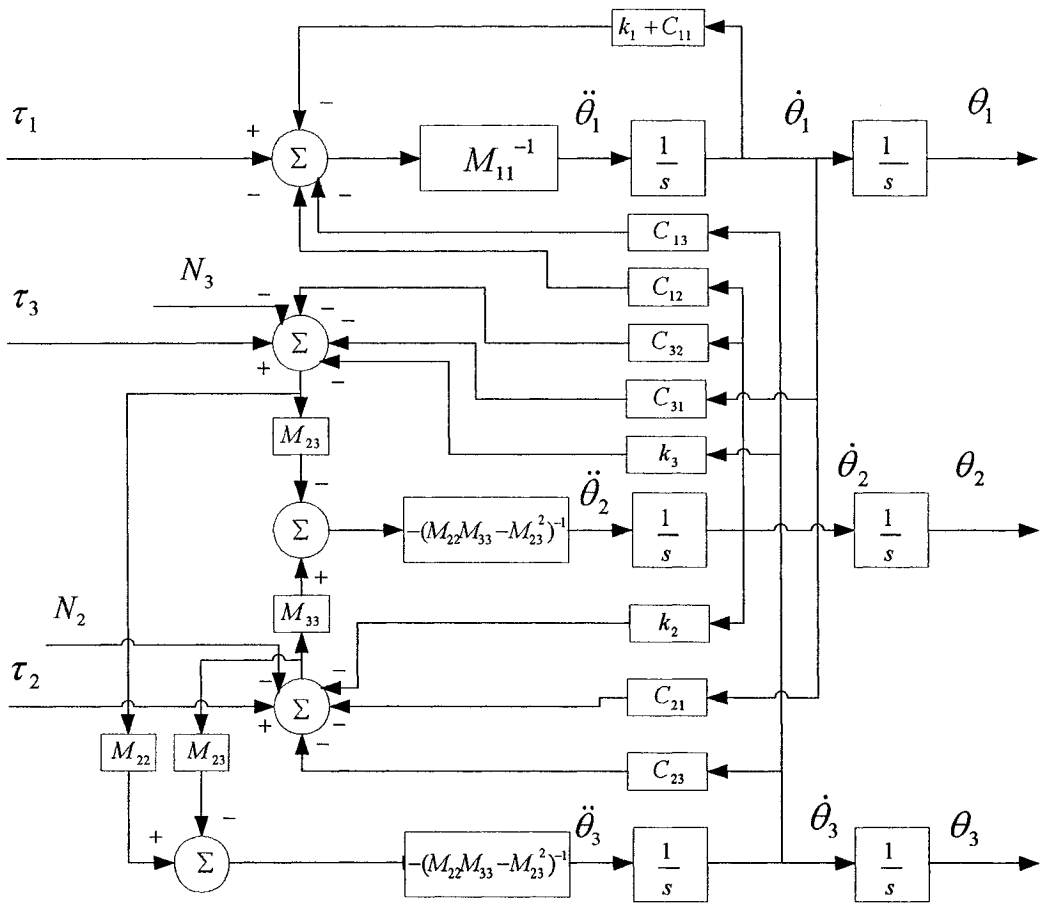

Figure 3.1: Block diagram of PHANToM™ model with damping factors

The resulting linearized continuous-time model is given by

$$\dot{x} = A_c x + B_c u_\tau$$
$$y = C_c x + D_c u_\tau \tag{3.9}$$

where the input torques are denoted by u_τ and

$$A_c = \begin{bmatrix} 0 & 0 & 0 & 1 & 0 & 0 \\ 0 & 0 & 0 & 0 & 1 & 0 \\ 0 & 0 & 0 & 0 & 0 & 1 \\ 0 & 0 & 0 & -444.4k_1 & 0 & 0 \\ 0 & -5.7-358.2k_2-407.8k_3 & 13.7-84.5k_2+595.5k_3 & 0 & .04k_2 & -.1k_3 \\ 0 & 2.4-89.9k_2+323.4k_3 & -84.2+277.5k_2-1476k_3 & 0 & -.26k_2 & .04k_3 \end{bmatrix}$$

$$B_c = \begin{bmatrix} 0 & 0 & 0 \\ 0 & 0 & 0 \\ 0 & 0 & 0 \\ 444.4 & 0 & 0 \\ 0 & 442.7 & -187.6 \\ 0 & -187.6 & 1152.6 \end{bmatrix}, \quad C_c = \begin{bmatrix} 1 & 0 & 0 & 0 & 0 & 0 \\ 0 & 1 & 0 & 0 & 0 & 0 \\ 0 & 0 & 1 & 0 & 0 & 0 \end{bmatrix}, \quad D_c = \begin{bmatrix} 0 & 0 & 0 \\ 0 & 0 & 0 \\ 0 & 0 & 0 \end{bmatrix}$$

The transfer function of the continuous-time model is then obtained by

$$T(s) = C_c (sI - A_c)^{-1} B_c + D_c \tag{3.10}$$

or equivalently according to the expressions above,

$$T(s) = \begin{bmatrix} t_{11} & 0 & 0 \\ 0 & t_{22} & t_{23} \\ 0 & t_{32} & t_{33} \end{bmatrix} \tag{3.11}$$

To discretize the above continuous-time model, the following efficient computational procedure that is described in [44] is used. The following series defined as

$$\psi = I + A_c T/2\left[I + A_c T/3(I + A_c T/4(I + ...(I + A_c T/N)))\right] \tag{3.12}$$

where T is denoted the sampling period and is set to 0.0005 (s), and the series is approximated to the 4^{th} step in the nested sequence (N = 4).

The above series representation is now utilized to obtain the desired discrete-time approximations of the continuous-time system model. The state space representation of the discrete-time system is now given by

$$\begin{aligned} x[n+1] &= A_d x[n] + B_d u_\tau[n] \\ y[n] &= C_d x[n] + D_d u_\tau[n] \end{aligned} \tag{3.13}$$

where the input torques are denoted by u_τ and

$$A_d = I + A_c T\psi \ , \ B_d = T\psi B_c \ , \ C_d = C_c \ \text{ and } \ D_d = D_c$$

Consequently, the discrete-time transfer funtion of the system is obtained [44] from

$$H(z) = C_d\,[zI - A_d]^{-1}\,B_d + D_d \tag{3.14}$$

Based on the information provided in the above transfer function, the discrete-time parametric linear transfer matrix model is given by (3.15). The terms in the transfer matrixes given in (3.15) are a function of the damping factors k_1, k_2 and k_3, namely

$$H(z) = \begin{bmatrix} h_{11} & 0 & 0 \\ 0 & h_{22} & h_{23} \\ 0 & h_{32} & h_{33} \end{bmatrix} \tag{3.15}$$

where

$$h_{ij}(z) = \frac{b_{ij1}z^4 + b_{ij2}z^3 + b_{ij3}z^2 + b_{ij4}z + b_{ij5}}{z^6 + a_{ij1}z^5 + a_{ij2}z^4 + a_{ij3}z^3 + a_{ij4}z^2 + a_{ij5}z + a_{ij6}} \quad \text{for i = 1, 2, 3 and j = 1, 2, 3} \tag{3.16}$$

with $a_{ijk} = a_{ijk}(k1, k2, k3)$.

3.6 Haptic Device Identification

In this section a system identification technique is used to determine the unknown damping coefficients in the linear model (3.15). A multivariable Auto-Regressive with eXogenous inputs (ARX) model is first developed based on the order and pure time-delay of the system given in (3.16).

3.6.1 Structure of ARX Model

The linear difference equation for the Multivariable ARX model structure [45] is presented below by (3.17). Since the white noise $e(t)$ enters as a direct error in this equation, this model is also called as equation error model.

$$A(q)y(t) = B(q)u(t) + e(t) \tag{3.17}$$

Where A(q) and B(q) contain the adjustable parameters. The matrix polynomial A(q) is an ny x ny matrix that is given by

$$A(q) = I_{ny} + A_1 q^{-1} + \ldots + A_{na} q^{-na} \tag{3.18}$$

or equivalently

$$A(q) = \begin{bmatrix} a_{11}(q) & a_{12}(q) & \cdots & a_{1ny}(q) \\ a_{21}(q) & a_{22}(q) & \cdots & a_{2ny}(q) \\ \cdots & \cdots & \cdots & \cdots \\ a_{ny1}(q) & a_{ny2}(q) & \cdots & a_{nyny}(q) \end{bmatrix} \tag{3.19}$$

where the entries a_{kj} are polynomials in the delay operator q^{-1}:

$$a_{kj}(q) = \delta_{kj} + a_{kj}^{1} q^{-1} + \ldots + a_{kj}^{na_{kj}} q^{-na_{kj}} \tag{3.20}$$

with δ_{kj} denoting the Kronecker-delta such that $\delta_{kk} = 1$, otherwise $\delta_{kj} = 0$, $k \neq j$. In the same manner the matrix polynomial B(q) is an ny x ny matrix that is given by

$$B(q) = B_0 + B_1 q^{-1} + \ldots + B_{nb} q^{-nb} \tag{3.21}$$

or equivalently

$$B(q) = \begin{bmatrix} b_{11}(q) & b_{12}(q) & \cdots & b_{1ny}(q) \\ b_{21}(q) & b_{22}(q) & \cdots & b_{2ny}(q) \\ \cdots & \cdots & \cdots & \cdots \\ b_{ny1}(q) & b_{ny2}(q) & \cdots & b_{nyny}(q) \end{bmatrix} \tag{3.22}$$

With

$$b_{kj}(q) = b_{kj}^{1} q^{-nk_{kj}} + \ldots + b_{kj}^{nb_{kj}} q^{-na_{kj}-nb_{kj}+1} \tag{3.23}$$

The delay from the input component j to the output component k is nk_{kj}. To associate the structural definition in terms of na, nb, nk, the kj-element of the na matrix is na_{kj}, while the kj-elements of nb and nk are nb_{kj} and nk_{kj} respectively. For the model in (3.15) the na, nb and nk are given by

$$\text{na} = \begin{bmatrix} 6 & 0 & 0 \\ 0 & 5 & 0 \\ 0 & 0 & 5 \end{bmatrix}, \quad \text{nb} = \begin{bmatrix} 5 & 0 & 0 \\ 0 & 4 & 4 \\ 0 & 4 & 4 \end{bmatrix} \text{ and nk} = \begin{bmatrix} 2 & 0 & 0 \\ 0 & 2 & 2 \\ 0 & 2 & 2 \end{bmatrix} \tag{3.24}$$

3.6.2 Experimental Linear Model

The unknown coefficients (a's and b's) in (3.15)-(3.16) are estimated using the least-squares method by applying the experimental data that was obtained from the haptic device. The experimental data corresponding to the joint angles (θ_1, θ_2 and θ_3) and applied torques (τ_1, τ_2 and τ_3) are recorded during the execution of the device associated with different sets of trajectories and scenarios. The transfer function of the experimental linear model is then obtained experimentally as shown below

$$\text{H}_{\text{exp}}(\text{z}) = \begin{bmatrix} h_{11} & 0 & 0 \\ 0 & h_{22} & h_{23} \\ 0 & h_{32} & h_{33} \end{bmatrix} \tag{3.25}$$

where

$$h_{11}(z)=\frac{-0.01z^4+0.0002z^3+.0013z^2+.0002z+-0.0022}{z^6-1.037z^5-.0022z^4+.0009z^3-.001z^2-.0002z+.04} \tag{3.26}$$

$$h_{22}(z)=\frac{.0228z^4-.0029z^3+.0011z^2+.016z}{z^6-z^5-.002z^4-.0003z^3+.0012z^2+.0007z} \tag{3.27}$$

$$h_{23}(z)=\frac{.0188z^4-.0025z^3-.0005z^2+.0111z}{z^6-z^5-.002z^4-.0003z^3+.0012z^2+.0007z} \tag{3.28}$$

$$h_{32}(z)=\frac{.0242z^4+.0001z^3-.0073z^2-.0169z}{z^6-1.1472z^5-1.1428z^4-.0192z^3+.0814z^2+.2278z} \tag{3.29}$$

$$h_{33}(z)=\frac{.0082z^4-.0008z^2-.0072z}{z^6-1.1472z^5-1.1428z^4-.0192z^3+.0814z^2+.2278z} \tag{3.30}$$

Also, the state space representation of the above model is given by

$$\begin{aligned} x[n+1] &= A_e x[n]+B_e u_\tau[n] \\ y[n] &= C_e x[n]+D_e u_\tau[n] \end{aligned} \tag{3.31}$$

where the input torques are denoted by u_τ and

$$A_e =$$

$$\begin{bmatrix}
1.04 & 0.001 & -0.0004 & 0.0005 & 0.0002 & -0.158 & 0 & 0 & 0 & 0 & 0 & 0 & 0 & 0 & 0 & 0 & 0 & 0 \\
2 & 0 & 0 & 0 & 0 & 0 & 0 & 0 & 0 & 0 & 0 & 0 & 0 & 0 & 0 & 0 & 0 & 0 \\
0 & 1 & 0 & 0 & 0 & 0 & 0 & 0 & 0 & 0 & 0 & 0 & 0 & 0 & 0 & 0 & 0 & 0 \\
0 & 0 & 1 & 0 & 0 & 0 & 0 & 0 & 0 & 0 & 0 & 0 & 0 & 0 & 0 & 0 & 0 & 0 \\
0 & 0 & 0 & 0.5 & 0 & 0 & 0 & 0 & 0 & 0 & 0 & 0 & 0 & 0 & 0 & 0 & 0 & 0 \\
0 & 0 & 0 & 0 & 0.25 & 0 & 0 & 0 & 0 & 0 & 0 & 0 & 0 & 0 & 0 & 0 & 0 & 0 \\
0 & 0 & 0 & 0 & 0 & 0 & 0 & 0 & 0 & 0 & 0 & 0 & 0 & 0 & 0 & 0 & 0 & 0 \\
0 & 0 & 0 & 0 & 0 & 0 & 0 & 0 & 0 & 0 & 0 & -0.0014 & 0 & 0 & 0 & 0 & 0 & 0 \\
0 & 0 & 0 & 0 & 0 & 0 & 0 & 0.5 & 0 & 0 & 0 & -0.0012 & 0 & 0 & 0 & 0 & 0 & 0 \\
0 & 0 & 0 & 0 & 0 & 0 & 0 & 0 & 0.5 & 0 & 0 & 0.0001 & 0 & 0 & 0 & 0 & 0 & 0 \\
0 & 0 & 0 & 0 & 0 & 0 & 0 & 0 & 0 & 1 & 0 & 0.001 & 0 & 0 & 0 & 0 & 0 & 0 \\
0 & 0 & 0 & 0 & 0 & 0 & 0 & 0 & 0 & 0 & 2 & 1 & 0 & 0 & 0 & 0 & 0 & 0 \\
0 & 0 & 0 & 0 & 0 & 0 & 0 & 0 & 0 & 0 & 0 & 0 & 0 & 0 & 0 & 0 & 0 & 0 \\
0 & 0 & 0 & 0 & 0 & 0 & 0 & 0 & 0 & 0 & 0 & 0 & 0 & 0 & 0 & 0 & 0 & -0.2278 \\
0 & 0 & 0 & 0 & 0 & 0 & 0 & 0 & 0 & 0 & 0 & 0 & 0 & 0.5 & 0 & 0 & 0 & -0.0407 \\
0 & 0 & 0 & 0 & 0 & 0 & 0 & 0 & 0 & 0 & 0 & 0 & 0 & 0 & 1 & 0 & 0 & 0.0096 \\
0 & 0 & 0 & 0 & 0 & 0 & 0 & 0 & 0 & 0 & 0 & 0 & 0 & 0 & 0 & 1 & 0 & 0.0714 \\
0 & 0 & 0 & 0 & 0 & 0 & 0 & 0 & 0 & 0 & 0 & 0 & 0 & 0 & 0 & 0 & 2 & 1.1472
\end{bmatrix}$$

$$C_e = \begin{bmatrix}
0 & -0.01 & 0.0002 & 0.0013 & 0.0004 & -0.0176 & 0 & 0 & 0 & 0 & 0 & 0 & 0 & 0 & 0 & 0 & 0 & 0 \\
0 & 0 & 0 & 0 & 0 & 0 & 0 & 0 & 0 & 0 & 0 & 0.5 & 0 & 0 & 0 & 0 & 0 & 0 \\
0 & 0 & 0 & 0 & 0 & 0 & 0 & 0 & 0 & 0 & 0 & 0 & 0 & 0 & 0 & 0 & 0 & 0.5
\end{bmatrix}$$

$$D_e = \begin{bmatrix}
0 & 0 & 0 \\
0 & 0 & 0 \\
0 & 0 & 0
\end{bmatrix}$$

$$B_e = \begin{bmatrix} 0.5 & 0 & 0 \\ 0 & 0 & 0 \\ 0 & 0 & 0 \\ 0 & 0 & 0 \\ 0 & 0 & 0 \\ 0 & 0 & 0 \\ 0 & 0 & 0 \\ 0 & 0.064 & 0.0444 \\ 0 & 0.0022 & -0.001 \\ 0 & -0.0029 & -0.0025 \\ 0 & 0.0228 & 0.0188 \\ 0 & 0 & 0 \\ 0 & 0 & 0 \\ 0 & -0.0338 & -0.0144 \\ 0 & -0.0073 & -0.0008 \\ 0 & 0.0001 & 0 \\ 0 & 0.0242 & 0.0082 \\ 0 & 0 & \end{bmatrix}$$

3.7 Estimation of Haptic Device Friction Factors

In the previous sections, two models are developed for the PHANToM™ haptic device. The first model is a parametric nonlinear model and the second one is an experimental linear model. The device frictional coefficients are estimated by matching the response of the experimental linear model with that of the mathematical nonlinear model (3.1) subject to the same haptic servo loop. In this section, two closed-loop haptic systems corresponding to the proposed haptic servo loop (Figure 3.2) is formed with the only difference being in the haptic device model. The closed-loop haptic system representation is shown in Figure 3.2 which contains an identified experimental linear model of the haptic device (3.25), the nonlinear forward kinematics, the nonlinear force/torque transformations,

the virtual couples, the virtual objects and the haptic controllers as described in details below. The multivariable control system must be guaranteed to operate under same desired performance specifications (stability) in order for one is able to estimate the friction factors

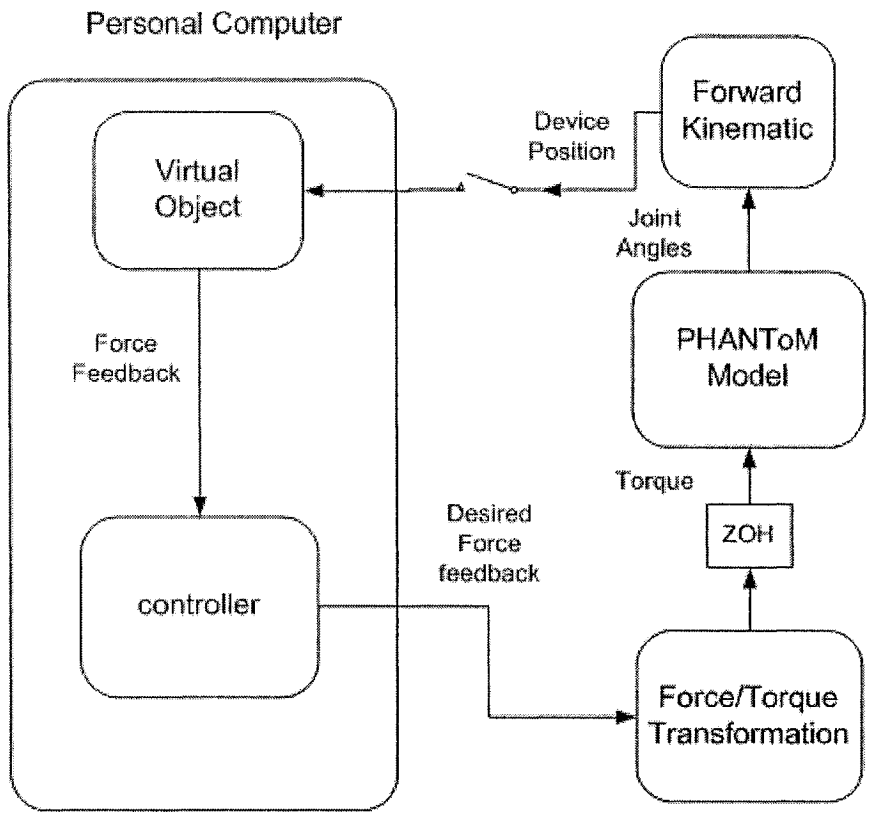

Figure 3.2: The Proposed closed-loop control haptic system

that are close to the actual device friction factors. In the following subsections, all the above components for the closed-loop haptic system will be explained individually.

3.7.1 Haptic Controller

A simple Lead-Lag controller is used as a haptic controller to determine the friction coefficients of the haptic device by comparing the experimental linear model with that of

the mathematical nonlinear models steady state error responses. The simplicity of the considered compensator implementation is the main reason behind choosing this classical control algorithm. Two simple discrete-time first order lead-lag compensator blocks are used in two out of the three force control loops as shown in Figures 3.3 and 3.4 and the Simulink schematic layout of these block diagrams are showing in Figures A.3 and A.4, respectively. The adjustment of the compensator gains, or equivalently its pole and zero locations was a time consuming process since unfortunately there is no direct way to optimally select these parameters. The finally designed compensator is selected to operate under the maximum stiffness of 3.5 N/mm (from device specifications in Table 2.1).

3.7.2 Nonlinear Forward Kinematics

The forward kinematics of the haptic device is described in details in Chapter 2. In the models used in Figures 3.4 and 3.5, the transitional part of the forward kinematics is extracted from $g_{st}(\theta)$ in (2.10) and is given by

$$p(\theta) = \begin{bmatrix} \sin(\theta_1)(l_1\cos(\theta_2) + l_2\sin(\theta_3)) \\ l_2 - l_2\cos(\theta_3) + l_1\sin(\theta_2) \\ -l_1 + \cos(\theta_1)(l_1\cos(\theta_2) + l_2\sin(\theta_3)) \end{bmatrix} \tag{3.32}$$

where $p(\theta) = [p_x\ p_y\ p_z]^T$ denotes the vector of the haptic device position movement respect to the origin and the joint angles as before are denoted by $[\theta_1\ \theta_2\ \theta_3]^T$.

3.7.3 Nonlinear Force/Torque Transformation

The Force/Torque transformation is obtained by using the Jacobian in (2.14). The relationship between the torque vector and force vector [5] is given by

$$\tau = \mathrm{J}^{\mathrm{T}} \begin{bmatrix} R^T & 0 \\ 0 & R^T \end{bmatrix} \mathrm{F} \tag{3.33}$$

where R is the rotation matrix, J is Jacobian of the haptic device, $F = [f_x\ f_y\ f_z]^T$ is the input force vector and the applied torques on the motors are denoted as before by $\tau = [\tau_1\ \tau_2\ \tau_3]^T$.

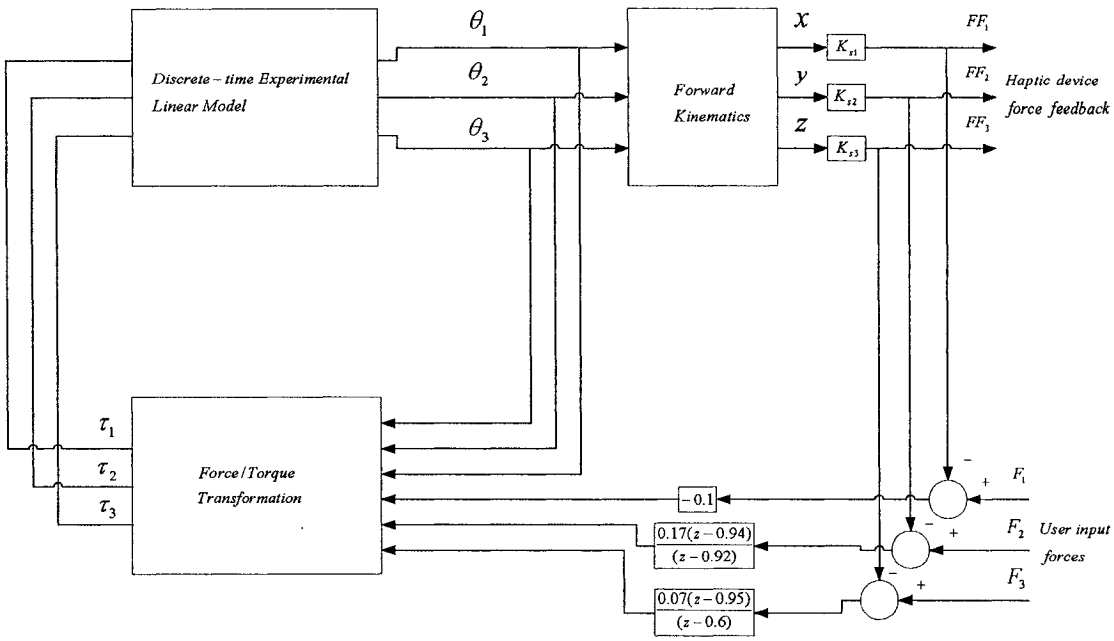

Figure 3.3: The Position/Force feedback control loop with experimental linear haptic device model

3.7.4 Virtual Couple

The virtual couple is modeled as a dashpot and a spring connected in parallel [4] (refer to Figures A.3 and A.4). The spring constant is the stiffness of the god-object and the constantdashpot constant plays the same role as that of the damping factor in case of interaction. The virtual couple is discretized using bilinear transformation and is mathematically expressed as

$$K - \frac{2 \times F_{vc} \times C \times (z-1)}{(z+1)} \tag{3.34}$$

where K, C and F_{vc} denote spring constant, dashpot constant and the sampling frequency, respectively. The sampling frequency is set to 1000 Hz that the sampling frequency rates of haptic servo loop in GHOST API as default value.

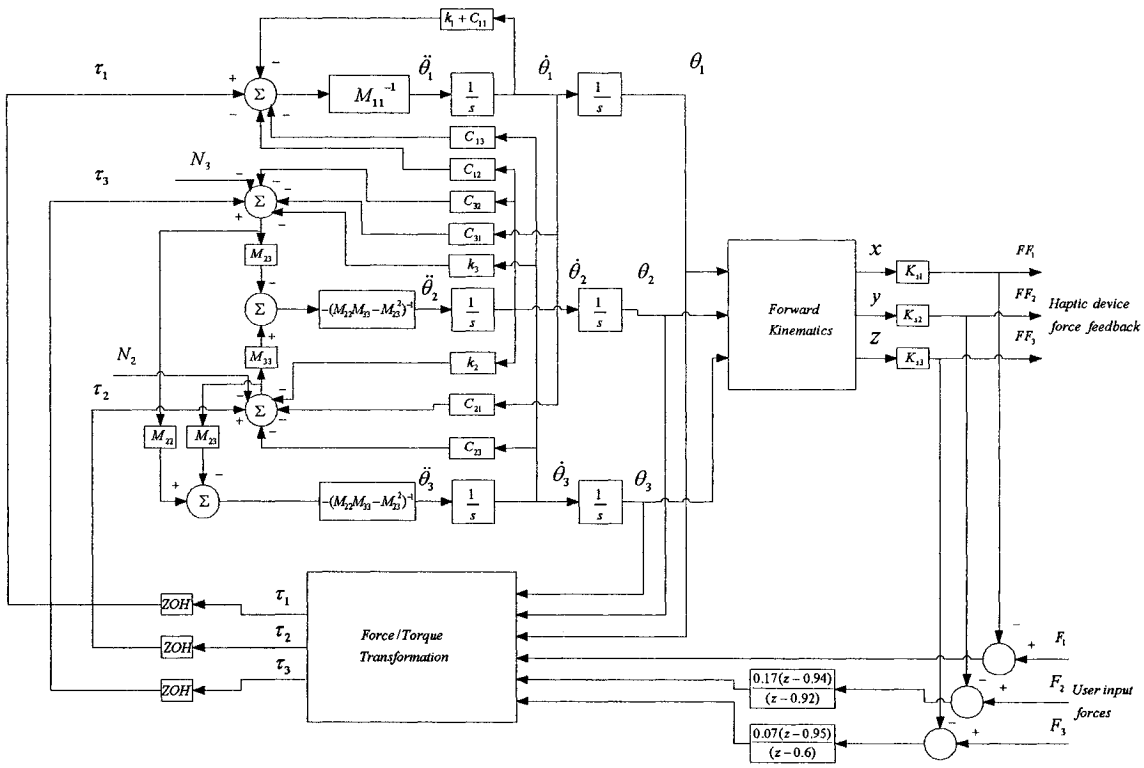

Figure 3.4: The Position/Force feedback control loop with the mathematical nonlinear haptic device model

3.7.5 Virtual Object

The virtual object represents any kind of geometry associated with the deformable virtual object. The virtual object considered in this work is a cube that the haptic point is interacting with on one side of it. The starting point of interaction between the haptic point and the surface of the object is considered as the origin in the 3D space.

3.8 Desirable Performance Specifications

The desirable performance specifications of the haptic interaction are determined based on the default values specified in the GHOST^{TM} API and the device specifications. The default value of the dashpot damping constant in the virtual couple is set to zero. Therefore, to maintain a desirable exertable force (F_e) on an object with K stiffness, the desirable displacement (the device position displacement with respect to the object surface) is determined by

$$\Delta x = \frac{F_e}{K} \tag{3.35}$$

According to the device characteristics provided in Table 2.1, the maximum exertable force is 8.5 N and the maximum stiffness is 3.5 N/mm for a virtual object. Consequently, there should be a 2.42 (mm) displacement of the haptic point to maintain 8.5 N as an exerted force on the surface of the virtual object. In the work in this thesis, the position steady state errors for the above values of the exerted force and object stiffness are examined and are shown in Table 3.1.

3.9 The Device Friction Coefficients

The device friction coefficients are estimated by matching the response of the experimental linear model (3.25) with that of the mathematical nonlinear model (3.1) subject to the same controller (the lead-lag controller). The responses of the experimental linear model and the mathematical nonlinear models are shown in Figure 3.5. The steady state errors for both models are compared and are shown in Table 3.1. The estimated friction factors are given by

$$k_1 = 0.05\ ,\ k_2 = 0.001 \text{ and } k_3 = 0.01 \text{ (N/rad/s)} \tag{3.36}$$

The estimated friction coefficients for the PHANToM ^{TM} haptic device are then substituted by the friction coefficients of the nonlinear mathematical model (3.1). The response of the system is now shown in Figure 3.6 without utilizing a closed loop controller. Clearly, it follows from Figure 3.6 that θ_2 and θ_3 tend to the equilibrium points given in (3.8) by using $\tau_1 = 0.01$, $\tau_2 = 0.01$ and $\tau_3 = 0.01$ as the input torques.

Table 3.1: Steady state errors of the device position (mm) for the linear and nonlinear models using the Lead-Lag compensator.

	Linear Model	Nonlinear Model
X	0.03	~0.0
Y	~0.0	0.3
Z	0.02	0.31

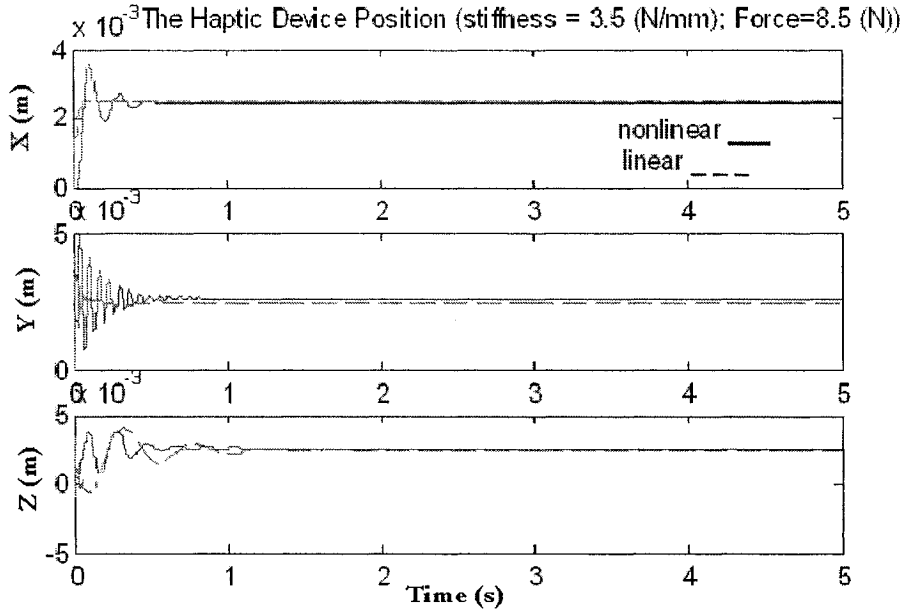

Figure 3.5: Comparing of the experimental linear and mathematical nonlinear models to obtain friction factors using the Lead-Lag compensator

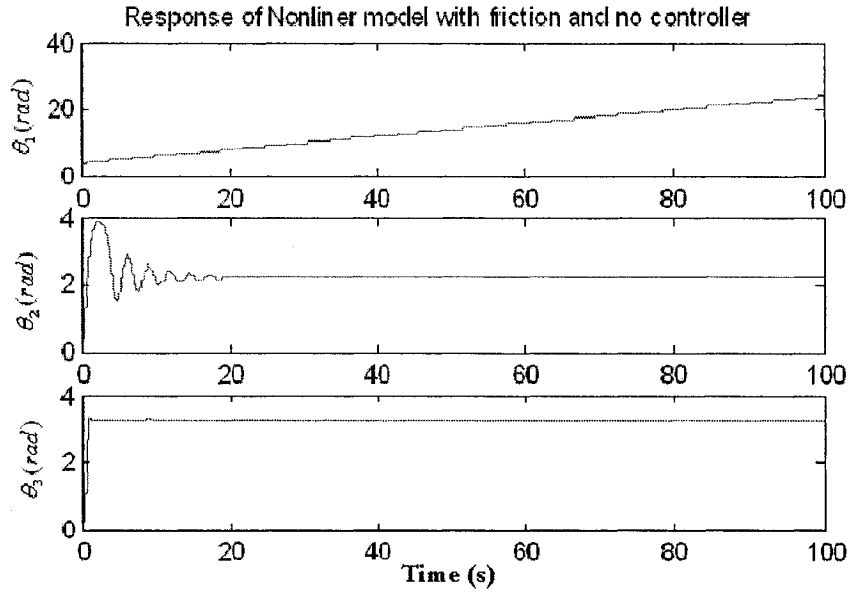

Figure 3.6: Response of the nonlinear model with the friction, without a closed-loop compensator

3.10 Modeling of the Proposed Configurations of the Haptic System

In the previous sections, the friction factors of the parametric model were obtained. By fixing the friction factors in the mathematical (original) nonlinear model of the haptic device and the mathematical linear model, one obtains two linear models, the first an experimental linear model and the second a mathematical linear model. To setup up a linear control design framework, a linear model is required that would correspond to the original nonlinear model of the haptic device. Also, the haptic control loop contains nonlinear forward kinematics and nonlinear force/torque transformation. In this section, various possible configurations for modeling of the haptic system using both linear and nonlinear models are proposed and discussed. The following modeling assumptions will be examined subject to different controllers in the next chapter. The performance of these models will be examined by comparing their results with the original nonlinear model that is subjected to the same controller design.

3.10.1 Case A: Using Experimental Linear Model as PHANToM^{TM} Device

The first model considered is formed by using an experimental linear model, nonlinear kinematics, nonlinear force/torque transformations and haptic controller as shown in Figure 3.3 and its Simulink schematic layout is shown in Figure A.3. In this case, the controllers that need to be designed based on the state space representation of model are designed only based on the experimental linear model and the effects of the nonlinear kinematics and nonlinear force/torque transformation are neglected. However, to design the lead-lag controller the effects of the nonlinear part are taken into account.

3.10.2 Case B: Using Mathematical Linear Model as PHANToM^{TM} Device

The second model considered is formed by the mathematical linear model, nonlinear kinematics and nonlinear force/torque transformations as shown in Figure 3.7 and its Simulink schematic layout is shown in Figure A.5. In this case, the controllers that need to be designed based on the state space representation of model are designed only based on the experimental linear model and the effects of the nonlinear kinematics and nonlinear force/torque transformation are neglected. However, to design the lead-lag controller the effects of the nonlinear part are taken into account.

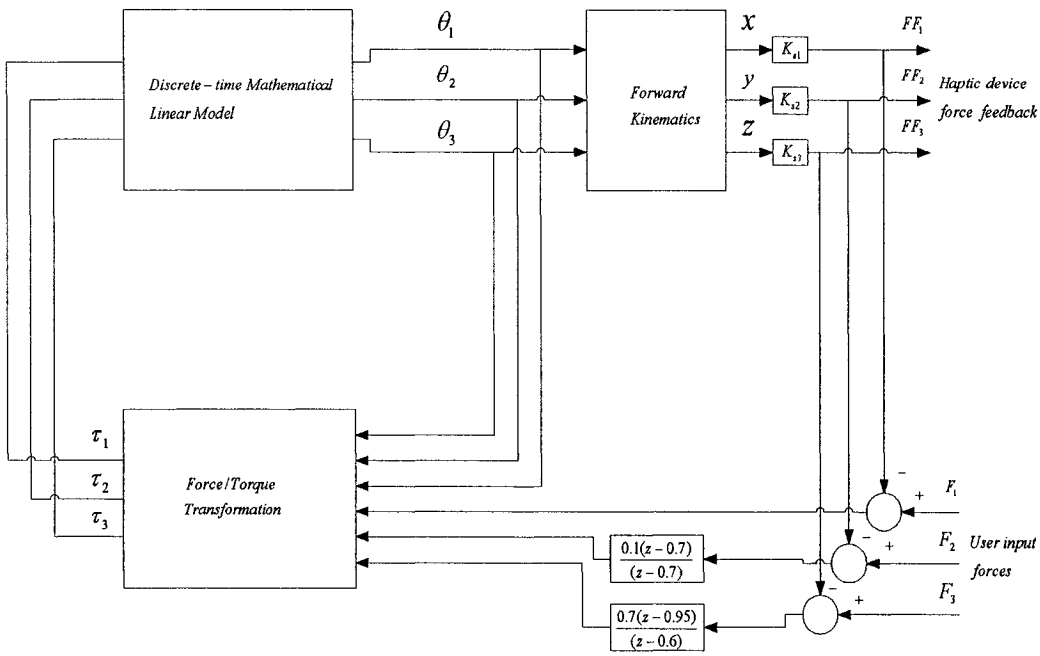

Figure 3.7: The Position/Force feedback control loop with the mathematical linear haptic device model in case B using lead-lag controller

3.10.3 Case C: Linearized Kinematics and Experimental Linear Model

The third model considered is formed by the experimental linear model in (3.35) combined with linearized kinematics, linearized force/torque transformations and haptic controllers as shown in Figure 3.8 and its Simulink schematic layout is shown in Figure A.6. In this case, the controller is designed only based on the new linear model. For notational simplicity, the term $\mathrm{J}^{\mathrm{T}}\begin{bmatrix} R^T & 0 \\ 0 & R^T \end{bmatrix}$ in equation (3.33) is denoted by $\overline{F}(\theta,u)$. To obtain an equivalent linear model, the derivation of $\overline{F}(\theta,u)$ is determined and for the sake of notational simplicity, we denoted $\frac{\partial \overline{F}}{\partial \theta} = \overline{F}_\theta$ and $\frac{\partial \overline{F}}{\partial u} = \overline{F}_u$. The linearized force/torque transformations were obtained subject to the input force commands corresponding to $\tau_1 = 0$ (Nm), $\tau_2 = 0.01$ (Nm) and $\tau_3 = 0.01$ (Nm) and the set of equilibrium points obtained in Chapter 2 which are $\theta_1^e =$ 0 (rad), $\theta_2^e = 2.2305$ (rad), and $\theta_3^e = 3.2776$ (rad). Also, the derivative of the transitional part of the forward kinematics, $P(\theta)$ given in (3.32) at the above equilibrium points is denoted by $\overline{P}$. Consequently, the state space representation of the new linear model with combination of the above three parts is given by

$$\begin{aligned} x[n+1] &= A_{dl}x[n] + B_{dl}u_f[n] \\ y[n] &= C_{dl}x[n] + D_{dl}u_f[n] \end{aligned} \tag{3.37}$$

where

$$A_{dl} = A_e + B_e\overline{F}_\theta(\theta^e)C_e, \quad B_{dl} = B_e\overline{F}_u(\theta^e)$$

$$C_{dl} = diag[K_{s1}, K_{s2}, K_{s3}]\overline{P}(\theta^e)C_e, \quad \mathrm{D_{dl}} = \mathrm{D_e}$$

where the derivative of the transitional part of the forward kinematics, $P(\theta)$, is given in (3.32) at the above equilibrium points is denoted by $\overline{P}(\theta^e)$, the input forces are denoted by u_f and the stiffness is denoted by K_s. The resulting numerical discrete-time model is given by

$$A_{dl} =$$

$$\begin{bmatrix}
1.04 & 0.001 & -0.0004 & 0.0005 & 0.0002 & -0.158 & 0 & 0 & 0 & 0 & 0 & 0 & 0 & 0 & 0 & 0 & 0 & 0 & 0 & 0 \\
2 & 0 & 0 & 0 & 0 & 0 & 0 & 0 & 0 & 0 & 0 & 0 & 0 & 0 & 0 & 0 & 0 & 0 & 0 & 0 \\
0 & 1 & 0 & 0 & 0 & 0 & 0 & 0 & 0 & 0 & 0 & 0 & 0 & 0 & 0 & 0 & 0 & 0 & 0 & 0 \\
0 & 0 & 1 & 0 & 0 & 0 & 0 & 0 & 0 & 0 & 0 & 0 & 0 & 0 & 0 & 0 & 0 & 0 & 0 & 0 \\
0 & 0 & 0 & 0.5 & 0 & 0 & 0 & 0 & 0 & 0 & 0 & 0 & 0 & 0 & 0 & 0 & 0 & 0 & 0 & 0 \\
0 & 0 & 0 & 0 & 0.25 & 0 & 0 & 0 & 0 & 0 & 0 & 0 & 0 & 0 & 0 & 0 & 0 & 0 & 0 & 0 \\
0 & 0 & 0 & 0 & 0 & 0 & 0 & 0 & 0 & 0 & 0 & 0 & 0 & 0 & 0 & 0 & 0 & 0 & 0 & 0 \\
0 & 0 & 0 & 0 & 0 & 0 & 0 & 0 & 0 & 0 & 0 & -0.0017 & 0 & 0 & 0 & 0 & 0 & 0 & 0 & 0 \\
0 & 0 & 0 & 0 & 0 & 0 & 0 & 0.5 & 0 & 0 & 0 & -0.0012 & 0 & 0 & 0 & 0 & 0 & 0 & 0 & 0 \\
0 & 0 & 0 & 0 & 0 & 0 & 0 & 0 & 0.5 & 0 & 0 & 0.0002 & 0 & 0 & 0 & 0 & 0 & 0 & 0 & 0 \\
0 & 0 & 0 & 0 & 0 & 0 & 0 & 0 & 0 & 1 & 0 & 0.0009 & 0 & 0 & 0 & 0 & 0 & 0 & 0 & 0 \\
0 & 0 & 0 & 0 & 0 & 0 & 0 & 0 & 0 & 0 & 2 & 1 & 0 & 0 & 0 & 0 & 0 & 0 & 0 & 0 \\
0 & 0 & 0 & 0 & 0 & 0 & 0 & 0 & 0 & 0 & 0 & 0 & 0 & 0 & 0 & 0 & 0 & 0 & 0 & 0 \\
0 & 0 & 0 & 0 & 0 & 0 & 0 & 0 & 0 & 0 & 0 & 0.0001 & 0 & 0 & 0 & 0 & -0.2278 \\
0 & 0 & 0 & 0 & 0 & 0 & 0 & 0 & 0 & 0 & 0 & 0 & 0 & 0.5 & 0 & 0 & 0 & -0.0407 \\
0 & 0 & 0 & 0 & 0 & 0 & 0 & 0 & 0 & 0 & 0 & 0 & 0 & 0 & 1 & 0 & 0 & 0.0096 \\
0 & 0 & 0 & 0 & 0 & 0 & 0 & 0 & 0 & 0 & 0 & -0.0001 & 0 & 0 & 0 & 1 & 0 & 0.0714 \\
0 & 0 & 0 & 0 & 0 & 0 & 0 & 0 & 0 & 0 & 0 & 0 & 0 & 0 & 0 & 2 & 1.1472
\end{bmatrix}$$

$$B_{dl} = \begin{bmatrix} 0.0734 & 0 & 0 \\ 0 & 0 & 0 \\ 0 & 0 & 0 \\ 0 & 0 & 0 \\ 0 & 0 & 0 \\ 0 & 0 & 0 \\ 0 & 0 & 0 \\ 0 & -0.0095 & -0.0184 \\ 0 & -0.0003 & 0.0002 \\ 0 & 0.0004 & 0.0009 \\ 0 & -0.0034 & -0.007 \\ 0 & 0 & 0 \\ 0 & 0 & 0 \\ 0 & 0.0048 & 0.0082 \\ 0 & 0.001 & 0.0014 \\ 0 & 0 & 0 \\ 0 & -0.0034 & -0.0055 \\ 0 & 0 & 0 \end{bmatrix}$$

$$C_{dl} = \begin{bmatrix} 0 & 5.42 & -0.11 & -0.7 & -0.2 & 9.54 & 0 & 0 & 0 & 0 & 0 & 0 & 0 & 0 & 0 & 0 & 0 & 0 \\ 0 & 0 & 0 & 0 & 0 & 0 & 0 & 0 & 0 & 0 & 0 & -230.6 & 0 & 0 & 0 & 0 & 0 & -40.33 \\ 0 & 0 & 0 & 0 & 0 & 0 & 0 & 0 & 0 & 0 & 0 & -297.3 & 0 & 0 & 0 & 0 & 0 & -294.8 \end{bmatrix}$$

$$D_{dl} = \begin{bmatrix} 0 & 0 & 0 \\ 0 & 0 & 0 \\ 0 & 0 & 0 \end{bmatrix}$$

An approximation considered for the model in case C is that a discrete-time linear system is combined with two other continuous-time systems and the result is a discrete-time system as shown in Figure 3.8.

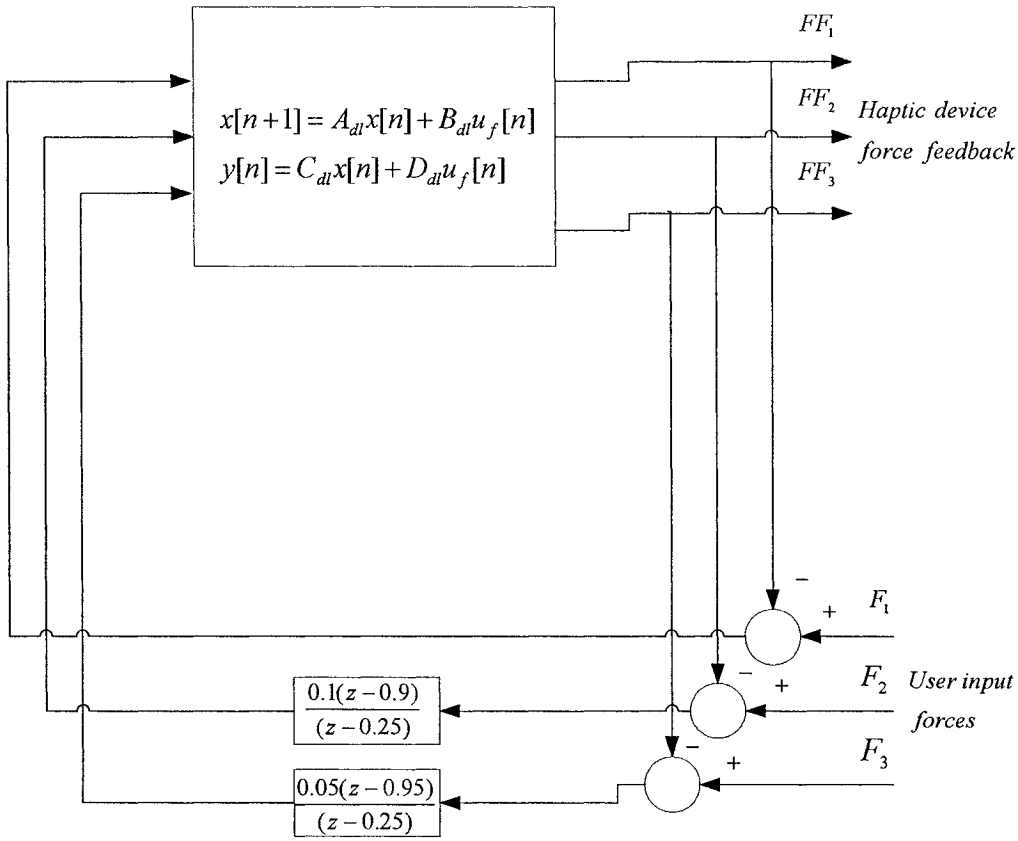

Figure 3.8: The Position/Force feedback control loop with the linear model in case C and Lead-Lag controller

3.10.4 Case D: Integrated Mathematical Linear Model

In order to achieve an integrated nonlinear model of the haptic device, force/torque transformations given in (3.33) is combined with the nonlinear model having three damping parameters given in (3.1). For notational simplicity, the term $J^T \begin{bmatrix} R^T & 0 \\ 0 & R^T \end{bmatrix}$ in equation (3.33) is denoted by $\overline{F}(\theta, u)$. The resulting equation is given by

$$M\ddot{\theta} + C\dot{\theta} + N = \overline{F}(\theta, u) \tag{3.38}$$

where the joint angles are denoted by the vector θ , the input forces are denoted by u, the inertia matrix by M, the matrix in the centrifugal and Coriolis forces by C and the vector of gravitational forces by N.

To obtain an equivalent linear model, the derivation of above equation is determined and is given by

$$\frac{\partial M}{\partial \theta}\ddot{\theta}\delta\theta + M\delta\ddot{\theta} + \frac{\partial C}{\partial \theta}\dot{\theta}\delta\theta + C\delta\dot{\theta} + \frac{\partial N}{\partial \theta}\delta\theta = \frac{\partial \overline{F}}{\partial \theta}\delta\theta + \frac{\partial \overline{F}}{\partial u}\delta u \tag{3.39}$$

where $\frac{\partial M}{\partial \theta}\ddot{\theta}\delta\theta = 0$ and $\frac{\partial C}{\partial \theta}\dot{\theta}\delta\theta = 0$ since $\ddot{\theta} = \dot{\theta} = 0$ at equilibrium condition. For the sake of notational simplicity, we denoted $\frac{\partial N}{\partial \theta} = \hat{n}$, $\frac{\partial \overline{F}}{\partial \theta} = \overline{F}_\theta$ and $\frac{\partial \overline{F}}{\partial u} = \overline{F}_u$.

The linear equation of motion was obtained subject to the input force commands corresponding to $\tau_1 = 0$ (Nm), $\tau_2 = 0.01$ (Nm) and $\tau_3 = 0.01$ (Nm) and the set of equilibrium points obtained in Chapter 2 which are $\theta_1^e = 0$ (rad), $\theta_2^e = 2.2305$ (rad), and $\theta_3^e =$ 3.2776 (rad). Specifically, the resulting linear equation of motion is given by

$$\overline{M}\delta\ddot{\theta} + \overline{C}\delta\dot{\theta} + \overline{n}\delta\theta = \hat{F}_\theta\delta\theta + \hat{F}_u\delta u \tag{3.40}$$

where $\overline{M} = M(\theta^e)$, $\overline{C} = C(\theta^e)$, $\overline{n} = \hat{n}(\theta^e)$, $\hat{F}_\theta = F_\theta(\theta^e, u)$ and $\hat{F}_u = F_u(\theta^e, u)$.

Consequently, the state space representation of the integrated linear model using forward kinematics (3.32) is given by

$$\dot{x} = A_{ci}x + B_{ci}u_f$$
$$y = C_{ci}x + D_{ci}u_f \tag{3.41}$$

where

$$A_{ci} = \begin{bmatrix} 0_{3x3} & I_{3x3} \\ -\overline{M}^{-1}(\overline{n} - \hat{F}_\theta) & -\overline{M}^{-1}\overline{C} \end{bmatrix}, \quad B_{ci} = \begin{bmatrix} 0_{3x3} \\ \overline{M}^{-1}\hat{F}_u \end{bmatrix}$$

$$C_{ci} = diag[K_{s1}, K_{s2}, K_{s3}] \times \overline{P}(\theta^e) \times [I_{3x3} \quad 0_{3x3}], \quad \mathrm{D_{ci}} = 0$$

where the derivative of the transitional part of the forward kinematics, $P(\theta)$ is given in (3.32), at the above equilibrium points is denoted by $\overline{P}(\theta^e)$, the input forces are denoted by u_f, and the stiffness is denoted by K_s. The resulting numerical continuous-time model is given by

$$\mathrm{A_{ci}} = \begin{bmatrix} 0 & 0 & 0 & 1 & 0 & 0 \\ 0 & 0 & 0 & 0 & 1 & 0 \\ 0 & 0 & 0 & 0 & 0 & 1 \\ 3.8814 & 0 & 0 & -22.22 & 0 & 0 \\ 0 & -9.2306 & 13.9947 & 0 & -0.4427 & 1.8765 \\ 0 & 3.9127 & -85.9628 & 0 & 0.1876 & -11.5263 \end{bmatrix}$$

$$\mathrm{B_{ci}} = \begin{bmatrix} 0 & 0 & 0 \\ 0 & 0 & 0 \\ 0 & 0 & 0 \\ 65.2545 & 0 & 0 \\ 0 & -54.0069 & -43.6007 \\ 0 & -1.842 & -162.2594 \end{bmatrix}$$

$$C_{ci} = \begin{bmatrix} -541.8694 & 0 & 0 & 0 & 0 & 0 \\ 0 & -461.1943 & -80.6751 & 0 & 0 & 0 \\ 0 & -594.6058 & -589.5053 & 0 & 0 & 0 \end{bmatrix}, \quad D_{ci} = \begin{bmatrix} 0 & 0 & 0 \\ 0 & 0 & 0 \\ 0 & 0 & 0 \end{bmatrix}$$

The above resulting continuous-time model is then discretized to obtain a discrete-time linear system. The discretized model as shown in Figure 3.9 and its Simulink schematic layout is shown in Figure A.7. The discretized model is given by

$$\begin{aligned} x[n+1] &= A_{di}x[n] + B_{di}u_f[n] \\ y[n] &= C_{di}x[n] + D_{di}u_f[n] \end{aligned} \tag{3.42}$$

where the input forces are denoted by u_f, the force feedback is denoted as output, y, and

$$A_{di} = \begin{bmatrix} 1 & 0 & 0 & 0.0005 & 0 & 0 \\ 0 & 1 & 0 & 0 & 0.0005 & 0 \\ 0 & 0 & 1 & 0 & 0 & 0.0005 \\ 0.0019 & 0 & 0 & 0.989 & 0 & 0 \\ 0 & -0.0046 & 0.007 & 0 & 0.9998 & 0.0009 \\ 0 & 0.002 & -0.0429 & 0 & 0.0001 & 0.9942 \end{bmatrix}$$

$$B_{di} = \begin{bmatrix} 0.0162 & 0 & 0 \\ 0 & -0.0135 & -0.0109 \\ 0 & -0.0005 & -0.0404 \\ 64.894 & 0 & 0 \\ 0 & 54.0018 & -43.6719 \\ 0 & -1.8392 & -161.7943 \end{bmatrix}$$

$$C_{di} = \begin{bmatrix} -0.2709 & 0 & 0 & -0.0001 & 0 & 0 \\ 0 & -0.2306 & -0.0403 & 0 & -0.0001 & 0 \\ 0 & -0.2973 & -0.2948 & 0 & -0.0001 & -0.0001 \end{bmatrix}$$

$$D_{di} = \begin{bmatrix} -0.0022 & 0 & 0 \\ 0 & 0.0016 & 0.0021 \\ 0 & 0.0021 & 0.0076 \end{bmatrix}$$

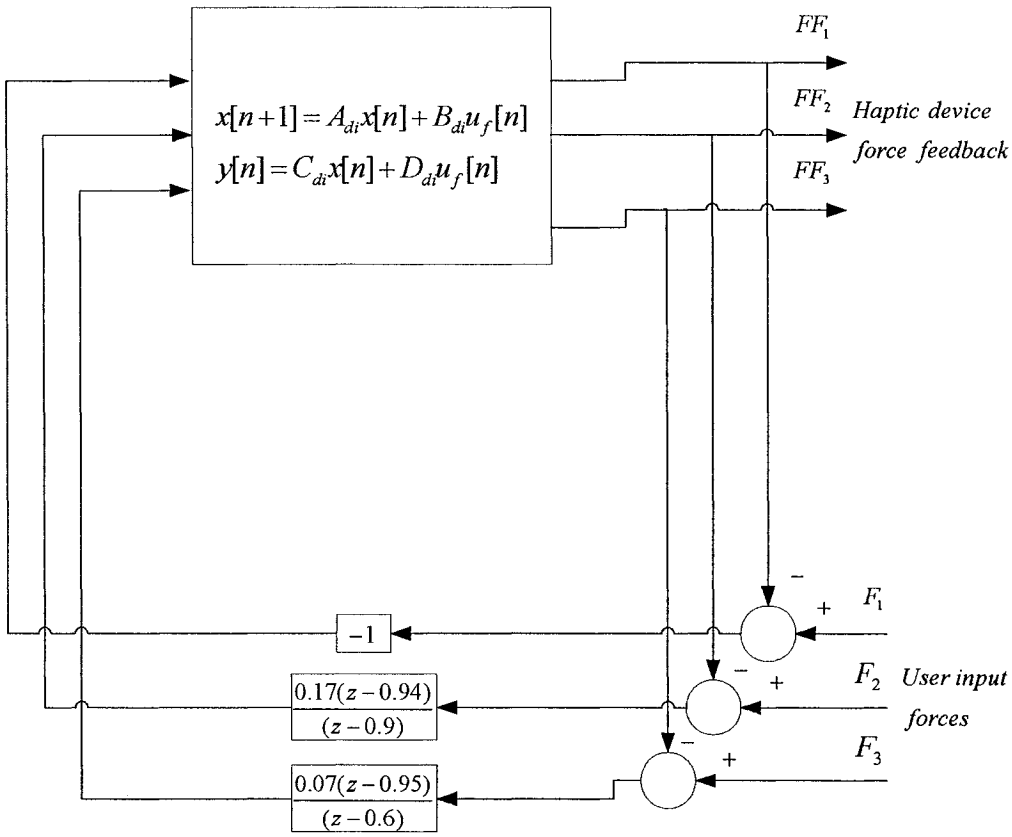

Figure 3.9: The Position/Force feedback control loop with the linear model in case D and Lead-Lag controller

3.11 Conclusions

In this chapter, three friction (damping) parameters were added to the nonlinear open loop model of the haptic device. An experimental linear model was then obtained by utilizing

system identification techniques. A Force/position control haptic loop was formed which contains an experimental linear model of the haptic device, nonlinear kinematics, nonlinear force/torque transformation, virtual object and a lead-lag controller. The device friction (damping) factors are estimated by comparing the response of the experimental linear model to that of the mathematical nonlinear model and the resulting friction coefficients are fixed in the nonlinear model. The response of the system with these damping parameters approached to the set of equilibrium points. Consequently, the estimated friction coefficients can be considered as a set of valid parameters for the haptic loop having the nonlinear mathematical PHANToM^{TM} model. Also, various possible configurations for modeling of the haptic system using both linear and nonlinear models were proposed and discussed. In the next chapter, several control strategies will be presented for maintaining and improving the achievable stability margins and resulting performances for the different modeling configurations proposed in this chapter for haptic system subject to interaction with deformable virtual objects.

Chapter 4

CONTROL STRATEGIES IN INTERACTION WITH VIRTUAL OBJECTS

4.1 Introduction

In the previous chapter, mathematical models are developed for haptic rendering of virtual objects. The haptic system representation shown in Figure 3.2 contains an experimental linear or mathematical nonlinear model of the haptic device, nonlinear kinematics, nonlinear force/torque transformations, virtual object and haptic controllers. With the known friction parameters, the combined nonlinear kinematics and force/torque transformations and the nonlinear device model shown in Figure 3.2, an integrated nonlinear model of the system is obtained. Subsequently, this model is then linearized and discretized for the purpose of control design. In this chapter, first the model of interacting with virtual object used in this work is presented. Furthermore, several control strategies are presented for maintaining and improving the achievable stability margins and resulting possible performances for a haptic rendering system subject to interaction with virtual objects. Two classes of control strategies are investigated here. The first is a Lead-Lag compensator designed based on classical control theory and the second scheme is a Linear-Quadratic-Gaussian (LQG) controller designed according to modern control theory. Position/force feedback linear controllers are developed utilizing two different strategies and their performances are compared to one another when applied to the linear haptic

system models (cases A, B and C). Also, the performances of both linear controllers are examined for the case D (the linearized integrated linear model) developed in last chapter to the nonlinear (original) haptic system model. Furthermore, the robustness of the position/force feedback control system is studied with respect to the changes in the different virtual object characteristics and scenarios.

4.2 Interaction with a Virtual Object

In Chapter 1, modeling of interaction with deformable objects was studied. In this section, one the modeling technique which is used in the haptic rendering using GHOST API and PHANToM^{TM} is specified. In order to achieve a stable interaction the authors in [4] offered a "god-object" approach, which interacts with the haptic device through a virtual couple. In this approach, the virtual couple is modeled as a dashpot and a spring connected in a parallel configuration. In addition, the Surface Contact Point (SCP) approach which maintains the contact state and the device end-effector position has also been proposed in [4],[7]. In the case of a contact, SCP stays on the surface of the virtual object and the device position point represents the current position of the device end-effector through the object. In this thesis, this approach is used and modeled explicitly.

4.3 Linear Controller Design

The multivariable control system designed consists of three inputs and three outputs to guarantee the desired performance specifications for the haptic system. Below, we first discuss the position/force feedback control loop performance specifications and the control system design methods. The robustness of the position/force feedback control system is

also investigated with respect to the changes in the applied forces. Finally, the performances of the control design methods are compared with one another.

4.3.1 Design Objectives

The desirable performance specifications are detailed based on the default values in the GHOST™ API and the device specifications described in section 3.8. In the work presented here, the position steady state errors for various sets of forces are examined to ensure that desirable displacements according to specifications in Table 4.1 are accomplished.

Table 4.1: The desirable device position (mm) as a function of the force and stiffness

Force (N)	Stiffness (N/mm)	Displacement (mm)
8.5	3.5	2.42
4	3.5	1.14
1	3.5	0.26
8.5	1.05	8.1

4.3.2 Lead-Lag Controller

The first class of a compensator that is designed is a simple Lead-Lag controller, which is applied to both the linear and nonlinear haptic system models. This controller was also used in the previous chapter to determine the friction coefficients of the haptic device by comparing the experimental linear and the mathematical nonlinear system model's steady state error responses. The simplicity of the compensator implementation has been the main reason focus in selecting this classical control algorithm. Two simple discrete-time first

order lead-lag compensator blocks are used in two out of the three force control loops as shown in Figure 4.2. The adjustment of the controller gains and the pole and zero locations were a time consuming process since unfortunately there is no direct approch to optimally select these parameters. The lead-lag compensator is designed for the maximum stiffness of 3.5 N/mm.

4.3.3 LQG Regulator

A discrete-time LQG controller is developed in this chapter that consists of an optimal state-feedback gain and a Kalman state estimator (refer to Figure 4.1). The optimal state-feedback control scheme that minimizes the quadratic cost function [6] in (4.1) is developed for a discrete-time model of (3.37) that is now subjected to a white noise source for the haptic device and a Gaussian noise acting as measurement noise. Also, integrators are augmented to the controllers in order to improve the steady state error responses for tracking the reference forces. The LQG controller is designed for the maximum stiffness and the covariance matrices are set to different diagonal values (e.g. Q = I and R = 10I). However, our extensive search for suitably selecting these parameters has only resulted in only a small change in the transient response. The formal mathematical description of the performance index used for minimization is given by

$$J = \lim_{T\to\infty} E\left\{\int_0^T \begin{bmatrix} x^T u^T \end{bmatrix} \begin{bmatrix} Q & N_c \\ N_c^T & R \end{bmatrix} \begin{bmatrix} x \\ u \end{bmatrix} dt\right\} \tag{4.1}$$

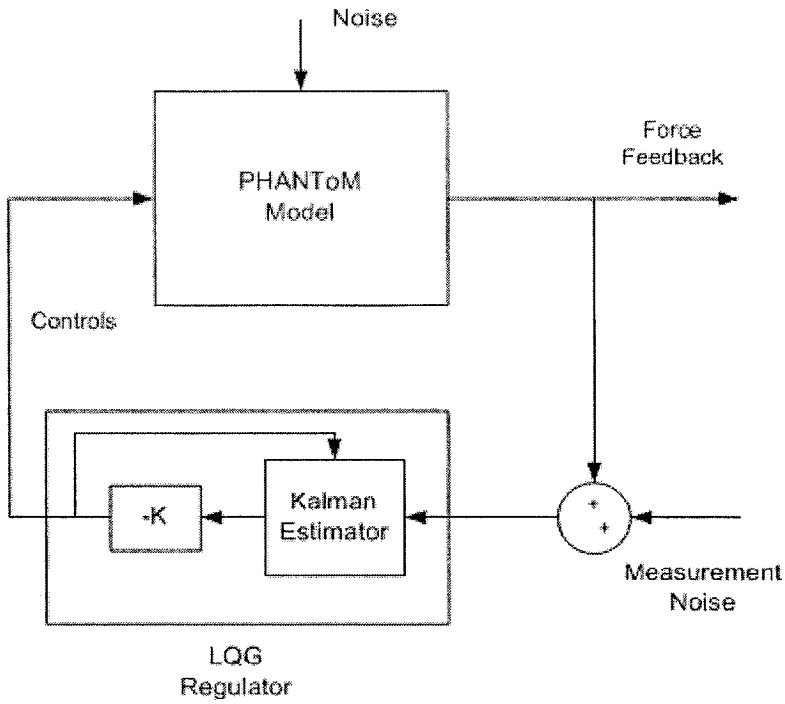

Figure 4.1: The Position/Force feedback control loop using LQG Regulator

4.4 Simulation Results

The schematic layouts of the mathematical nonlinear and the linear models with lead-lag controllers are shown in Figures 3.4 and 3.9. The block diagrams of the mathematical nonlinear and the linear models equipped with LQG controllers are shown in Figures 4.2 and 4.3 and its Simulink schematic layout is shown in Figures A.8 and A.9, respectively. As shown in these figures, there are three force inputs and three force feedback outputs.

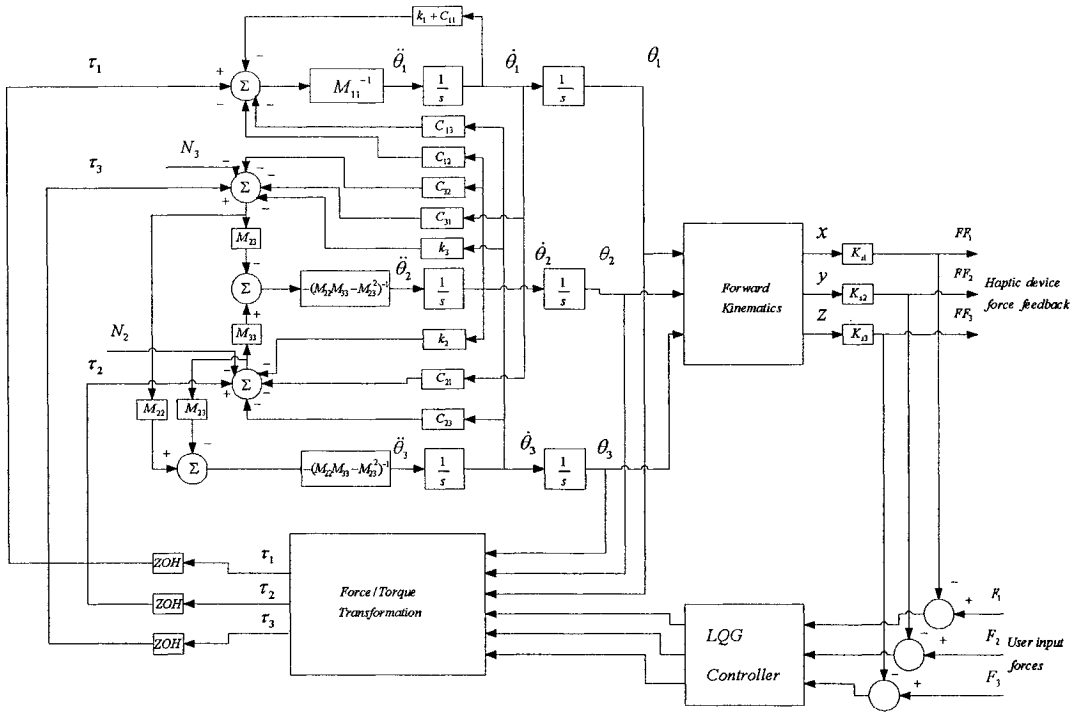

Figure 4.2: The Position/Force feedback control loop with the mathematical nonlinear model and LQG controller

4.4.1 Case A: Using Lead-Lag Compensator and LQG Regulator

The response of the linear model using both the lead-lag compensators and the LQG controllers are shown in Figures 4.4 and 4.5, respectively for the maximum stiffness of 3.5 N/mm and the maximum forces of 8.5 N. The response of the linear and the nonlinear haptic models using the lead-lag compensators and the LQG controllers for different values of input forces are shown in Figures 4.6 and 4.7, respectively. The selected forces are F1 = 1 (N), F2 = 4 (N) and F3 = 8.5 (N).

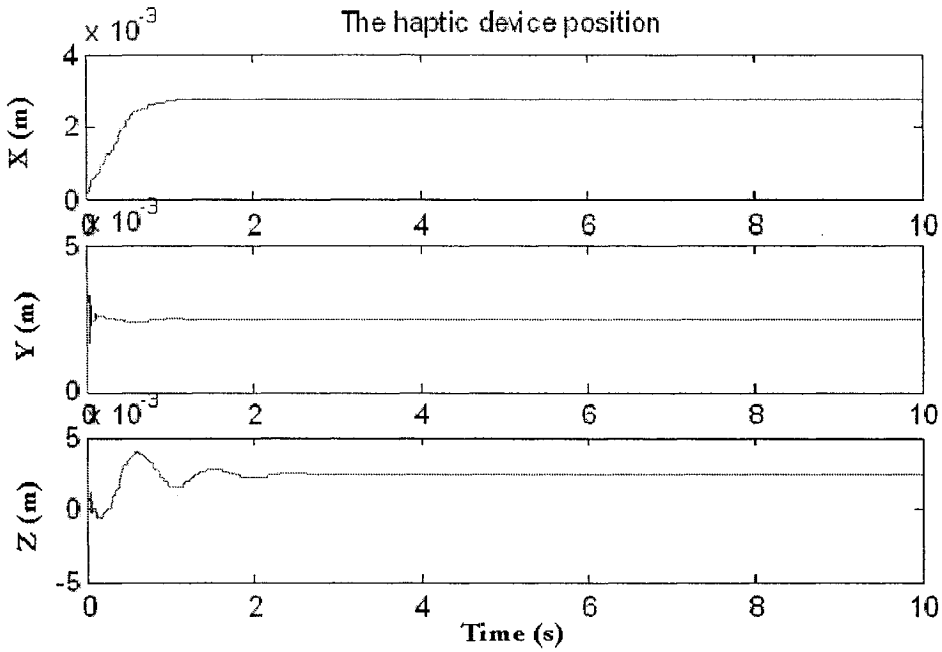

Figure 4.3: Response of the linear model in case A using the Lead-Lag compensator with the stiffness of 3.5 (N/mm)

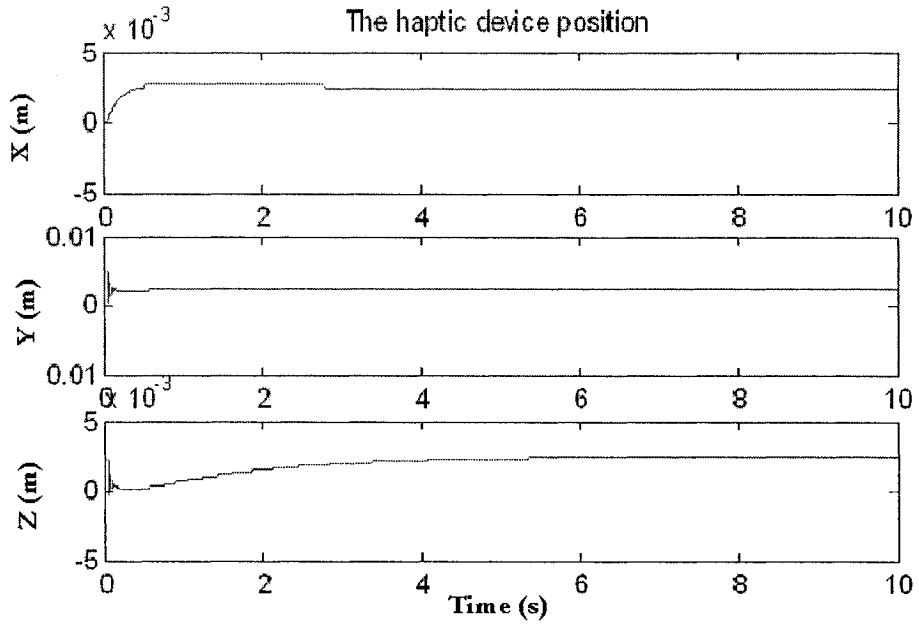

Figure 4.4: Response of the linear model in case A using the LQG controller with the stiffness of 3.5 (N/mm)

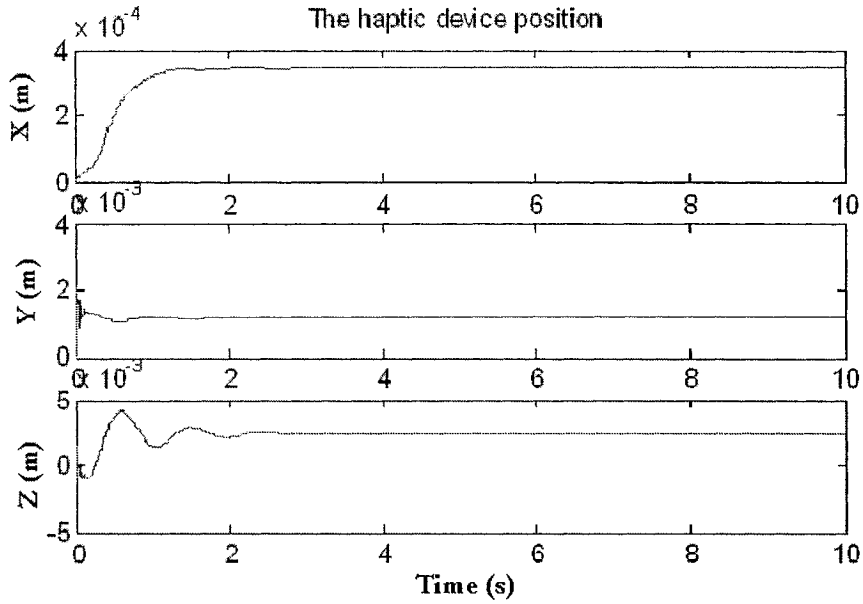

Figure 4.5: Response of the linear model in case A to different forces using the lead-lag controller

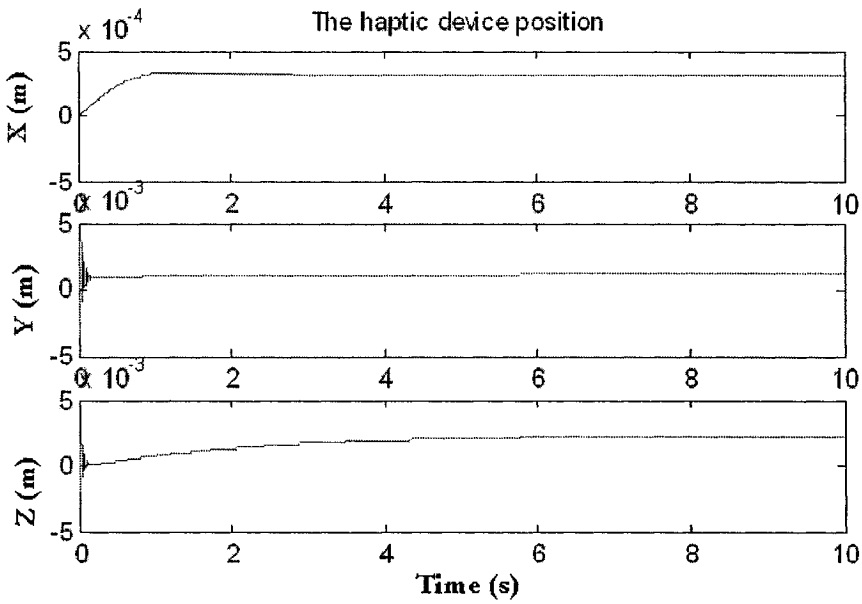

Figure 4.6: Response of the linear model in case A to different forces using the LQG controller

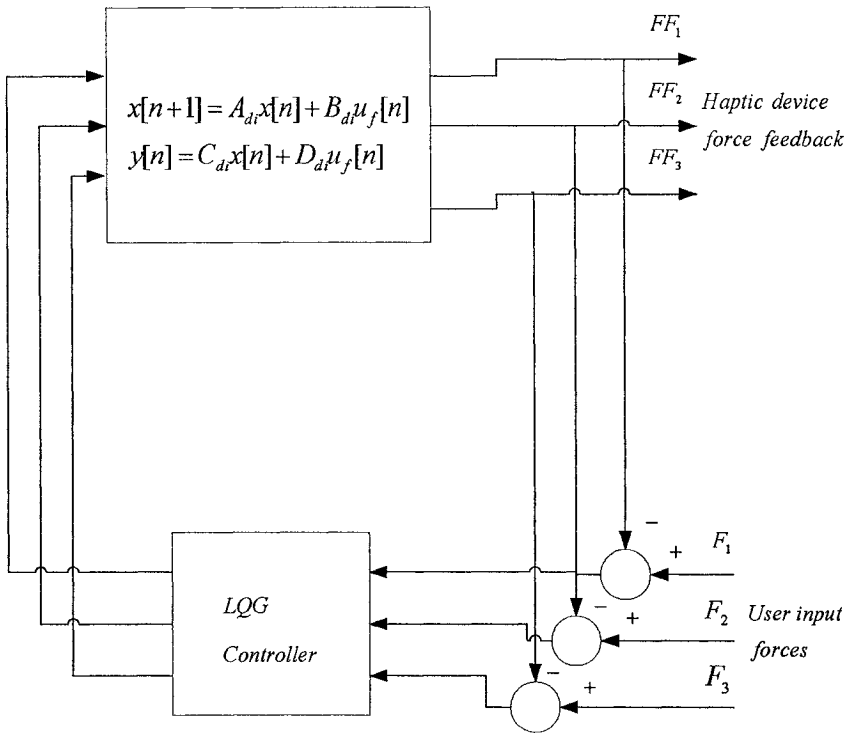

Figure 4.7: The Position/Force feedback control loop with the mathematical linear model in case D and LQG controller

4.4.2 Case B: Using Lead-Lag Compensator and LQG Regulator

The response of the linear model in case B using both the lead-lag compensators and the LQG controllers are shown in Figures 4.8 and 4.9 , respectively for the maximum stiffness of 3.5 N/mm and the maximum forces of 8.5 N. The response of the linear and the nonlinear haptic models using the lead-lag compensators and the LQG controllers for different values of input forces are shown in Figures 4.10 and 4.11 , respectively. The selected forces are F1 = 1 (N), F2 = 4 (N) and F3 = 8.5 (N). The justification for an unstable behavior in case of an LQG regulator can be attributed to the fact that the controller did not explicitly take into account the dynamics due to forward and force/torque transformations in its design, whereas the lead-lag controller was fine tuned with these models explicitly included.

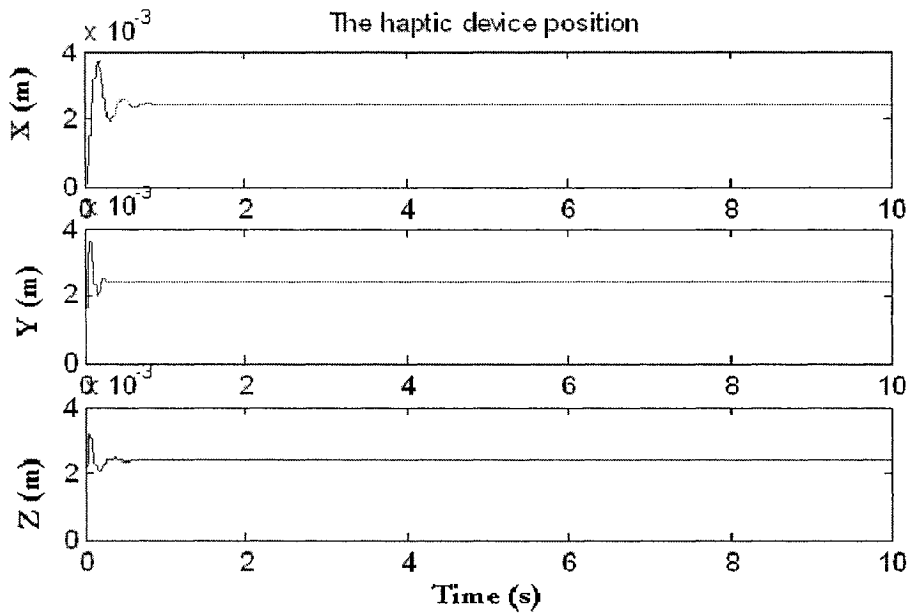

Figure 4.8: Response of the linear model in case B using the Lead-Lag compensator with the stiffness of 3.5 (N/mm)

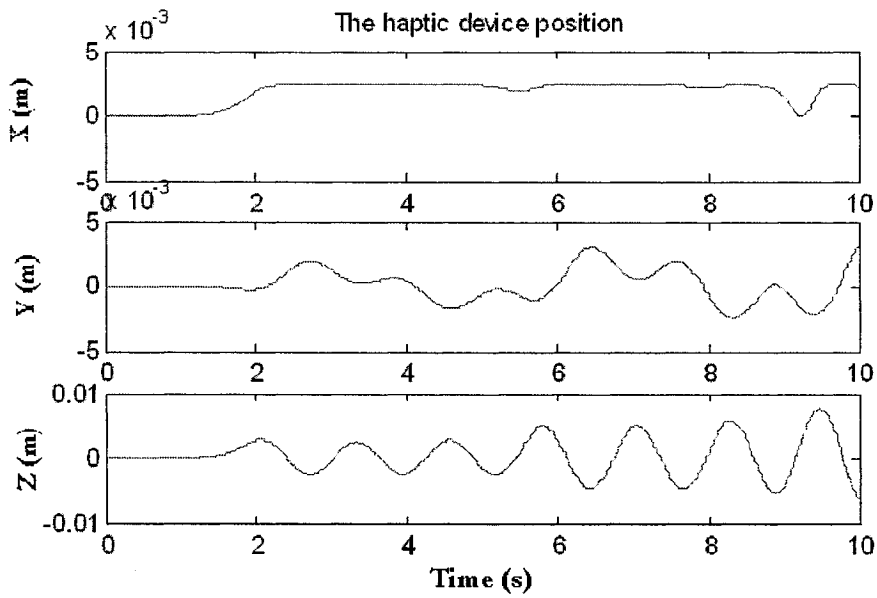

Figure 4.9: Response of the linear model in case B using the LQG controller with the stiffness of 3.5 (N/mm)

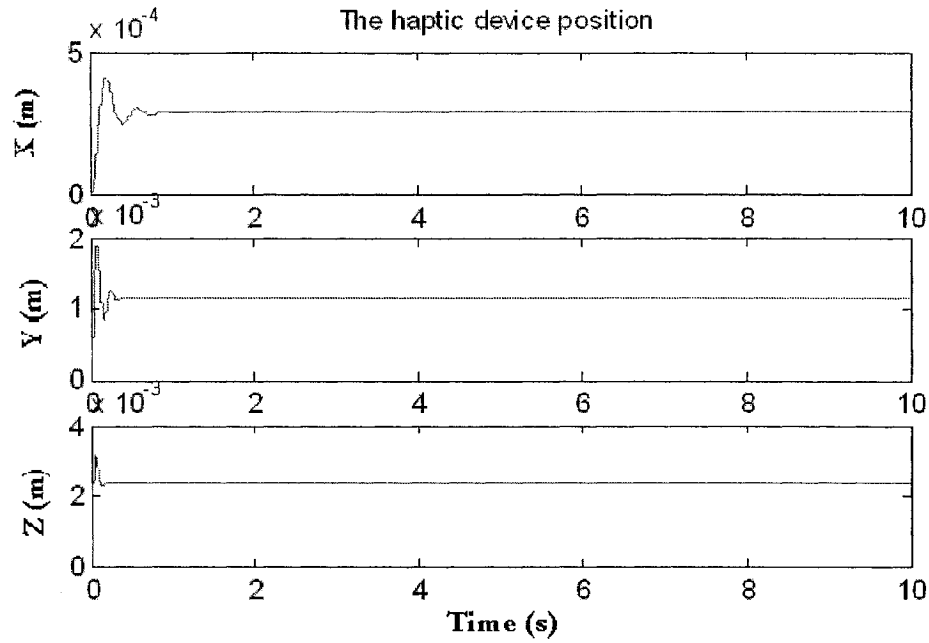

Figure 4.10: Response of the linear model in case B to different forces using the lead-lag controller

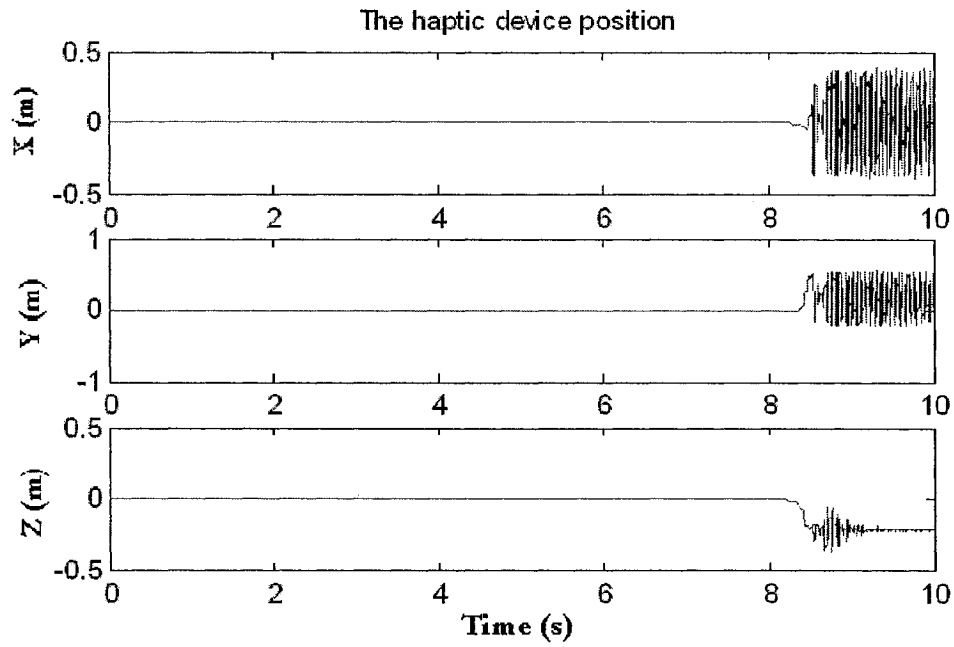

Figure 4.11: Response of the linear model in case B to different forces using the LQG controller

4.4.3 Case C: Using Lead-Lag Compensator and LQG Regulator

The response of the linear model in case C using both the lead-lag compensators and the LQG controllers are shown in Figures 4.12 and 4.13, respectively for the maximum stiffness of 3.5 N/mm and the maximum forces of 8.5 N. The response of the linear and the nonlinear haptic models using the lead-lag compensators and the LQG controllers for different values of input forces are shown in Figures 4.14 and 4.15, respectively. The selected forces are F1 = 1 (N), F2 = 4 (N) and F3 = 8.5 (N). The justification for the steady state error in case of the LQG regulator can be attributed to the fact that lack of integrators to track the input reference for LQG controller. In next case integrators are augmented to the controllers in order to improve the steady state error responses for tracking the reference forces.

4.4.4 Case D: Using Lead-Lag Compensator and LQG Regulator

The response of the mathematical linear and nonlinear models using both the lead-lag compensators and the LQG controllers are shown in Figures 4.16 and 4.17, respectively for the maximum stiffness of 3.5 N/mm and the maximum forces of 8.5 N. The response of the linear and the nonlinear haptic models using the lead-lag compensators and the LQG controllers for different values of input forces are shown in Figures 4.18 and 4.19, respectively. The selected forces are F1 = 1 (N), F2 = 4 (N) and F3 = 8.5 (N).

The response of the mathematical linear and the nonlinear models using the lead-lag compensators and the LQG controllers for the stiffness =1.05 (N/mm) are shown in Figures 4.20 and 4.21, respectively. The forces are selected as F1 = 8.5 (N), F2 = 8.5 (N) and F3 = 8.5 (N).

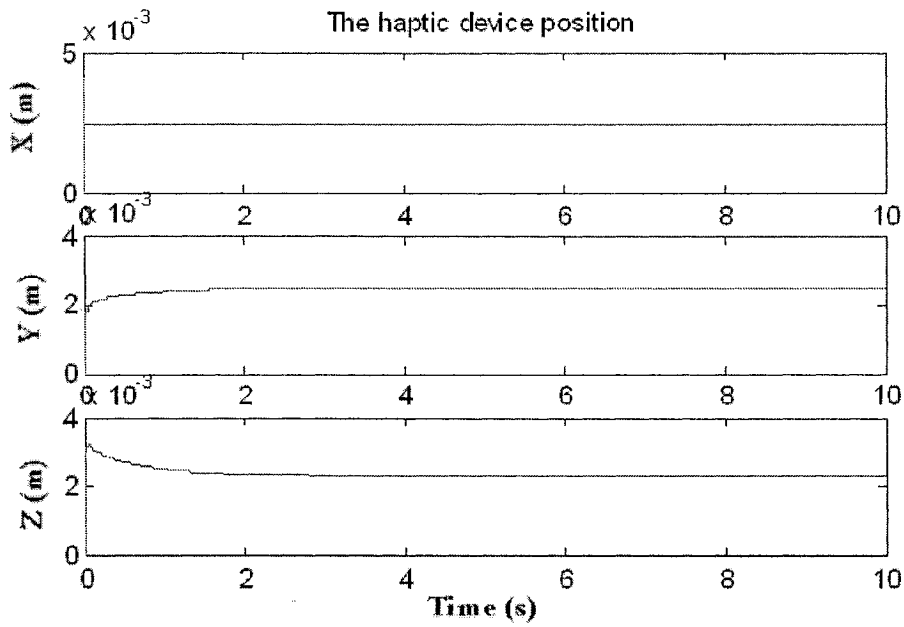

Figure 4.12: Response of the linear model in case C using the Lead-Lag compensator with the stiffness of 3.5 (N/mm)

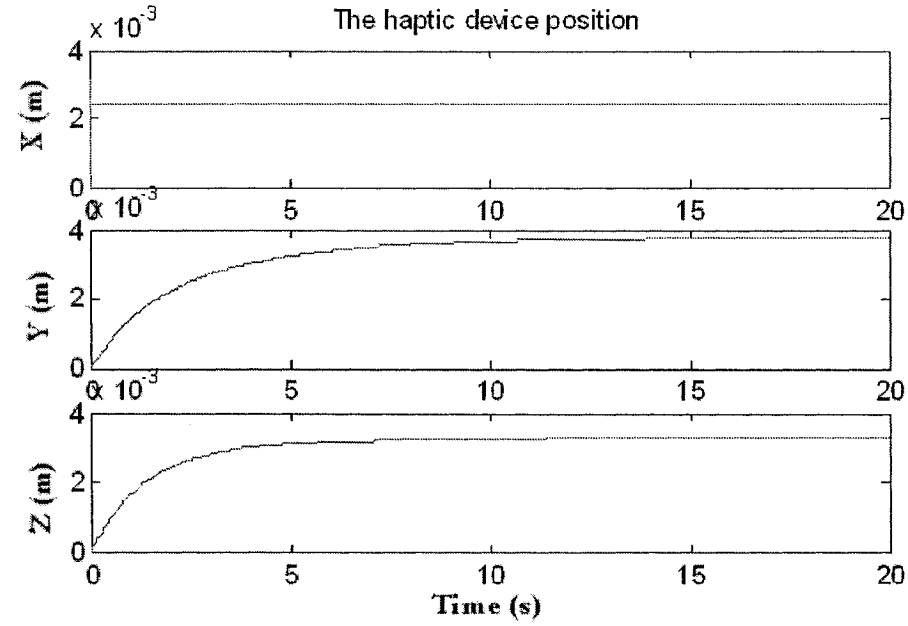

Figure 4.13: Response of the linear model in case C using the LQG controller with the stiffness of 3.5 (N/mm)

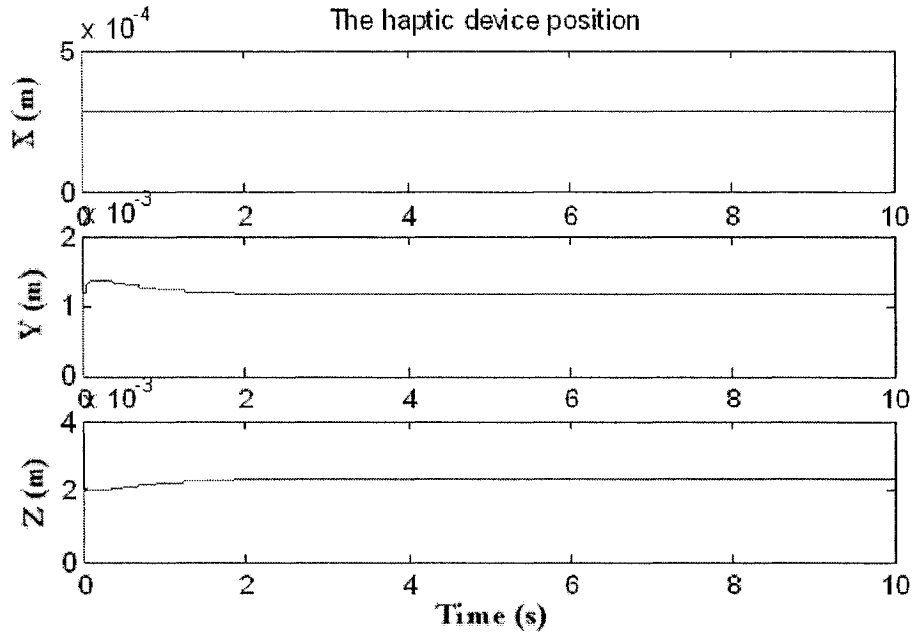

Figure 4.14: Response of the linear model in case C to different forces using the lead-lag controller

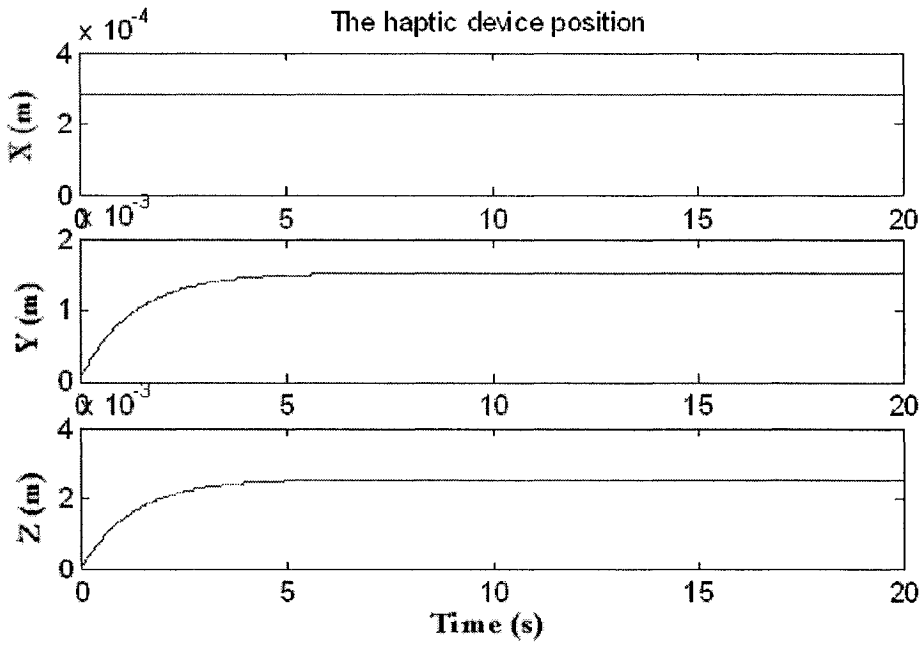

Figure 4.15: Response of the linear model in case C to different forces using the LQG controller

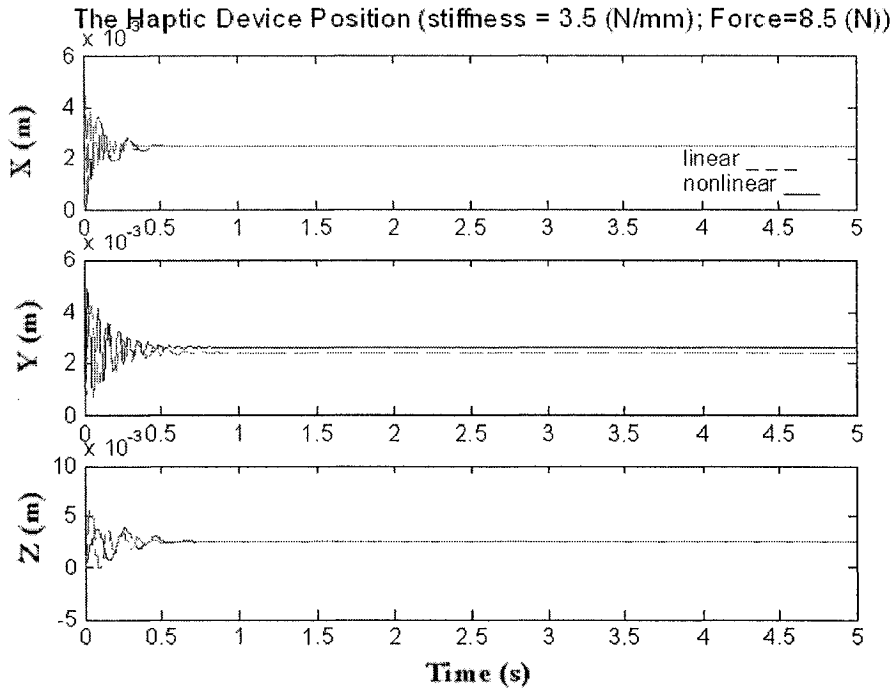

Figure 4.16: Response of the linear and the nonlinear models using the Lead-Lag compensator

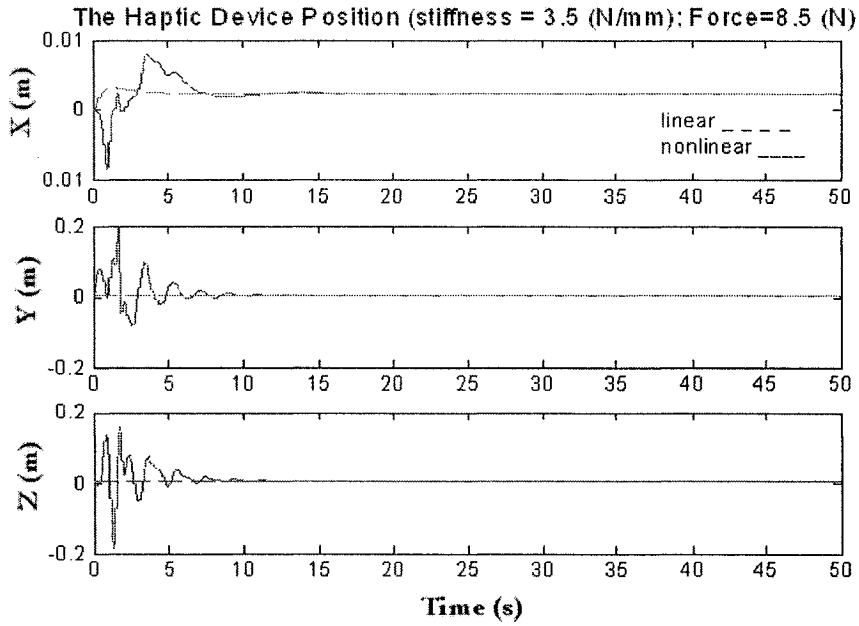

Figure 4.17: Response of the linear and the nonlinear models using the LQG controller

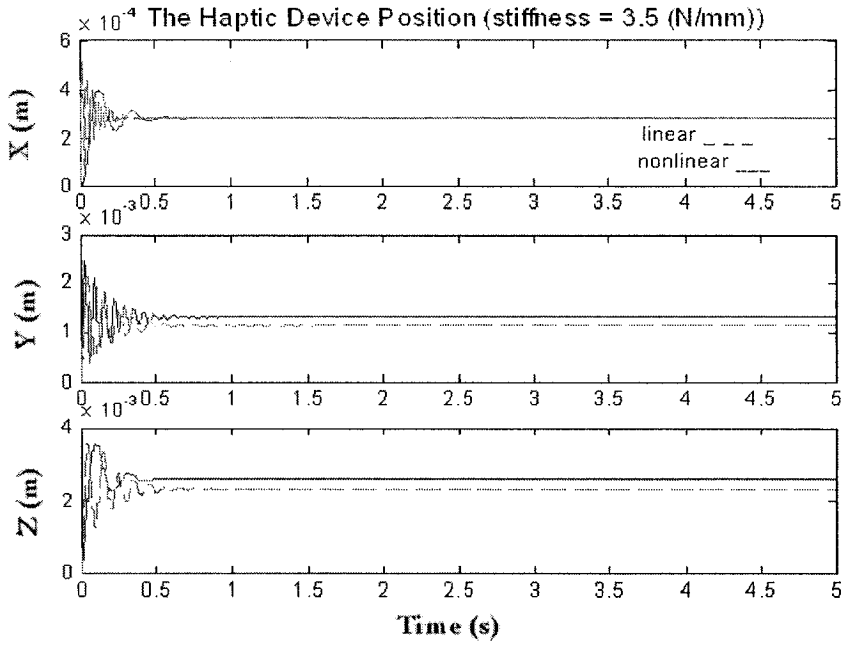

Figure 4.18: Response of the models to different forces using the lead-lag controller

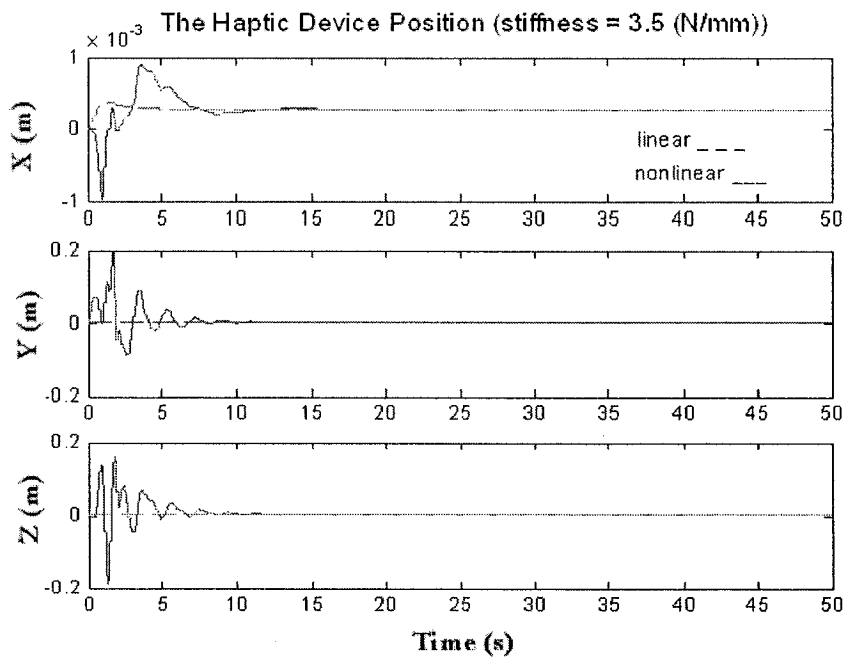

Figure 4.19: Response of the models to different forces using the LQG controller

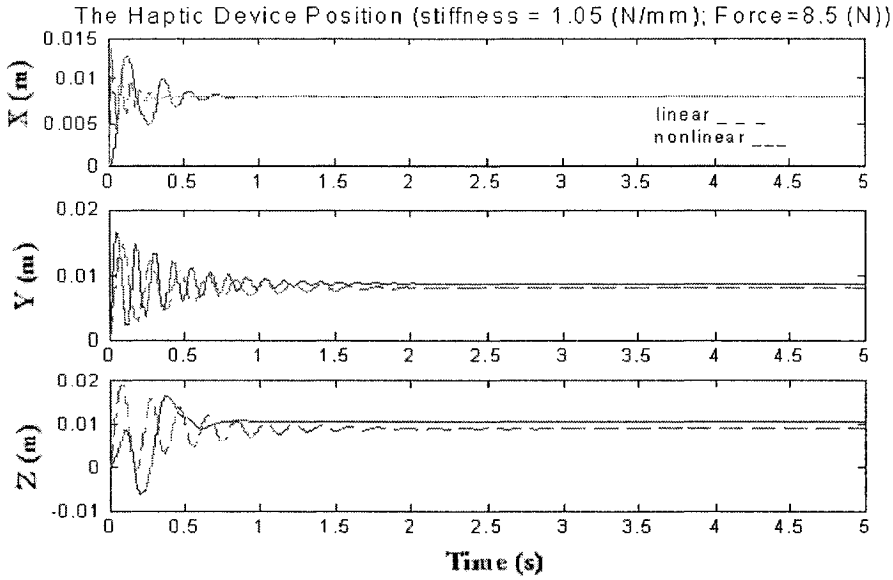

Figure 4.20: Response of the models for a low stiffness object using the lead-lag controller

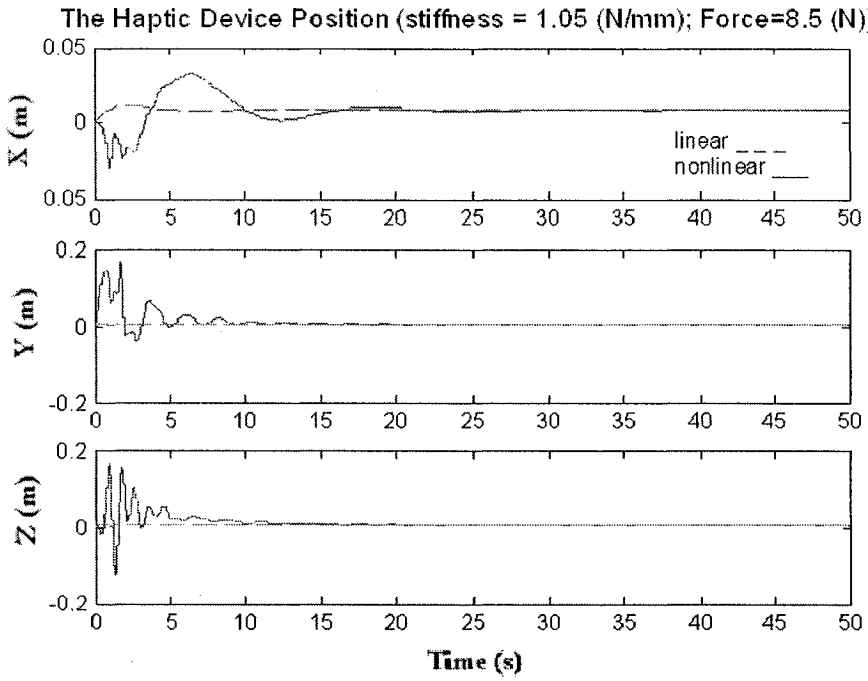

Figure 4.21: Response of the models for a low stiffness object using the LQG controller

4.5 Discussion of the Comparative Results

Based on the simulation results provided in this chapter, the LQG compensator shows a good performance with respect to the steady state error requirements. Although it has achieved a poor transient response for the nonlinear model, the LQG control scheme is sufficiently robust to satisfy the steady state error design objectives stated in section 4.3.1. As shown in Figure 4.21, the closed loop control system using the LQG compensator maintains almost a zero steady state error for different virtual object stiffness values. This controller does perform also well for the maximum stiffness (3.5 N/mm). The closed loop control system using the lead-lag controller as seen from Figure 4.20 indicates that there are some steady state errors corresponding to the low stiffness objects. However, the compensator's transient response is acceptable. Furthermore, the LQG controller demonstrates a good performance to force variations when compared to the lead-lag compensator (refer to Figures 4.18 and 4.19).

4.6 Conclusions

In this chapter various modeling configuration were examined. Finally, the linearized integrated nonlinear model of the system (case D) presented a very robust performance in case of interaction with the objects with different materials (stiffness) and different applied forces. We have shown that the proposed force/position control designs can ensure and maintain desirable forces on the virtual object surface by examining the linear controllers to control the original nonlinear model of the system. However, the LQG compensator design requires to be investigated further in order to achieve improved transient responses. Also

the design of the lead-lag controller could be made more complicated instead of using only a simple first order compensator structure.

Chapter 5

INTERACTING AND SLIDING WITH AND ON DEFORMABLE OBJECTS

5.1 Introduction

In this chapter a stable and robust point-based haptic rendering method is presented for interacting with various types of deformable elastic object varying from low-stiffness (soft) to high-stiffness (high), using nonlinear haptic device model and force/position control loop presented in the previous chapters. The proposed technique offers a high-fidelity 3D force reflecting haptic model for guaranteeing a stable sliding and force feedback field over the surface of polygonal-based deformable bodies with different normal stiffness in each polygonal mesh. The presented control algorithms in previous chapters are examined for maintaining and improving the stability margins and achievable performances for the haptic display with force continuity. The modeling of deformable objects is studied and the solutions to the problems of interaction and sliding motion with the haptic point (end-effector of the haptic device) are investigated. The robustness of the proposed algorithm is studied with respect to the changes in the applied force and deformable object stiffness. For the case of sliding, a method is developed to guarantee a stable contact during sliding over the deformable object with discrete normal forces.

5.2 Modeling of the Deformable Objects

To develop a suitable haptic display for interacting with deformable objects not only the properties for the object such as position, geometry, texture and surface frictions [4],[8] should be described, but the type of the object material should also be taken into account. As mentioned earlier, modeling of the object and its interaction properties, calculating force feedback and defining the object texture and material are easy to accomplish by using polygonal mesh. From a practical perspective, the GHOST API also supports triangular polygons. This software provides the haptic interaction and scene graph support for triangular polygons [7]. The proposed model in this thesis is based on polygonal mesh; however it could be extended to other methods as well. The deformable object is considered as a cube. The haptic point is interacting with one side of the cube. The trajectory of the haptic point initiates from the origin (left corner of the side of cube) and continues on the surface of the cube based on applied forces on the haptic device. The application of a force towards inside of the cube results in certain deformation on the surface of the cube.

5.3 Sliding Motion and Force Continuity

In this chapter, we simulate the case of the interaction and sliding motion of the haptic point with and on a rigid object and with and on a deformable object. Sliding over the surface of a deformable object with force continuity close to the actual force response is one of the main challenges that we intend to address. In the case of sliding motion, tangential forces are applied against the motion of the haptic point to make a stable haptic rendering [8]. The problem that is arising in the case of sliding motion between two

polygons with large differences in the normal stiffness is that the system could easily loose its stability. One approach to cope with this problem is to introduce more friction forces to solve this problem.

5.3.1 Surface Normal and Tangent Stiffness

Normal and tangential forces are employed to represent different kinds and effects of object material and texture for haptic display. A normal stiffness is associated with each polygonal mesh and a tangent stiffness is considered for imposing tangential forces to surface in opposite directions of the haptic point motion. The tangential forces gain the realistic perception of virtual objects and the simulation would then appear close to a real sense of interaction with objects [8]. In our simulation the tangent stiffness is set to 1 N/mm in any direction on the surface of the object. The softness of different parts of the deformable object is simulated using the normal stiffness. A typical normal stiffness for adjacent polygonal meshes is shown in Figure 5.5.

5.3.2 Force Field

In GHOST API a force field technique is used to simulate a smooth force feedback resulting from touching objects in the haptic scene using integration of normal forces [7]. A force field could be defined and specified based on an optional force characteristic of the scene. As a result, the side effects such as buzzing and unstable forces are prevented using the concept of force field [7],[8]. GHOST SDK does an interpolation between normal forces (based on normal stiffness) to achieve a smooth feel at the edges between two adjacent polygons. There are two ways to define normal forces for polygonal meshes. First one is to define a separate normal vector at each corner of the polygonal mesh and

interpolate all to a surface normal. Second one is to define one normal vector for the entire polygonal mesh [7]. In our simulations, a force field is assigned to each polygonal mesh which is proportional to its normal stiffness. As a result, the haptic point is subject to quite different normal forces throughout its trajectory over different polygonal meshes. It is shown that the method is robust enough to maintain a stable force feedback by a necessity of discrete force field (refer to Figure 5.9).

5.4 Desirable Performance Specifications

In addition to the earlier desirable performance specifications stated in previous chapters, the desirable deflections in Table 5.1 are considerd. The surface deflection steady state errors for different values of stiffness are examined to ensure that the values in Table 5.1 are accomplished. For sliding, the objective is a stable trajectory and force feedback that is the result of touching the surface of a deformable object with different discrete normal forces for polygonal meshes (refer to Figure 5.5).

Table 5.1:The desirable and resulted deflection (mm) of deformable objects in the Z direction as a function of the stiffness

Force (N)	Stiffness (N/mm)	Deflection (mm)		
		Desired	Lead-Lag	LQG
8.5	3.5	2.42	2.61	2.41
8.5	1.0	8.50	11.14	8.53
8.5	2.0	4.25	4.93	4.25
8.5	2.5	3.40	3.84	3.4
8.5	3.0	2.83	3.14	2.83

5.5 Simulation Results

The responses of the haptic system using both the lead-lag compensator and the LQG controller are shown in Figures 5.1 and 5.2, respectively for the maximum stiffness of 3.5 N/mm in three directions and the maximum forces of 8.5 N. The responses of the haptic system subject to deflection in the Z direction using the lead-lag compensator and the LQG controller for the stiffness = 1 (N/mm), 2 (N/mm), 2.5 (N/mm) and 3 (N/mm) are shown in Figures 5.3 and 5.4, respectively. The forces are selected as F1 = 8.5 (N), F2 = 8.5 (N) and F3 = 8.5 (N).

5.5.1 Simulation of the Sliding Motion

The responses of the haptic system using the lead-lag compensator are shown in Figures 5.6 and 5.7, respectively for variations of normal stiffness of adjacent polygonal meshes in the surface of the cube (as shown in Figure 5.5) and applied forces in Figure 5.8. Furthermore, the force feedback based on the applied force inputs and mesh's normal stiffness is shown in Figure 5.9. Moreover, the 3D trajectory of the haptic device position is shown in Figure 5.10. The discussion the merit of the performance is presented in the next section.

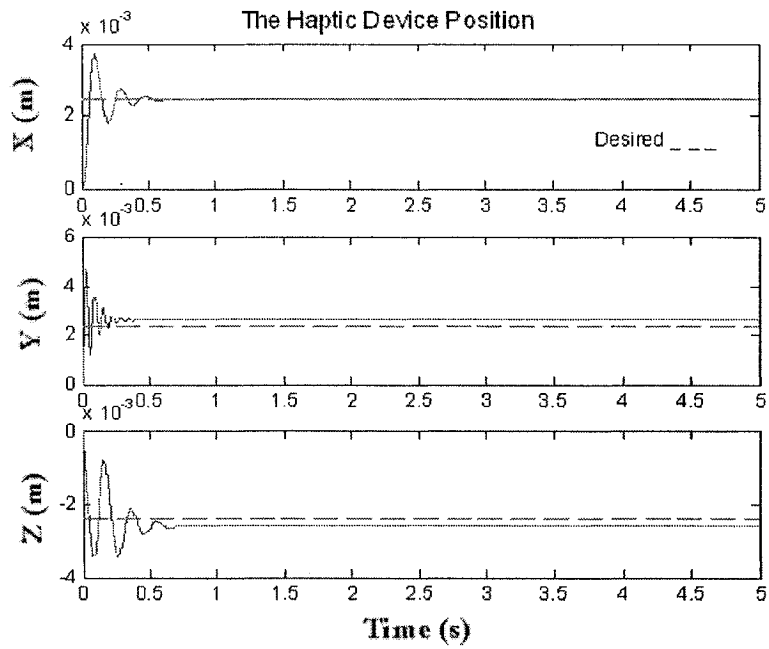

Figure 5.1: Response of the nonlinear model using the Lead-Lag compensator

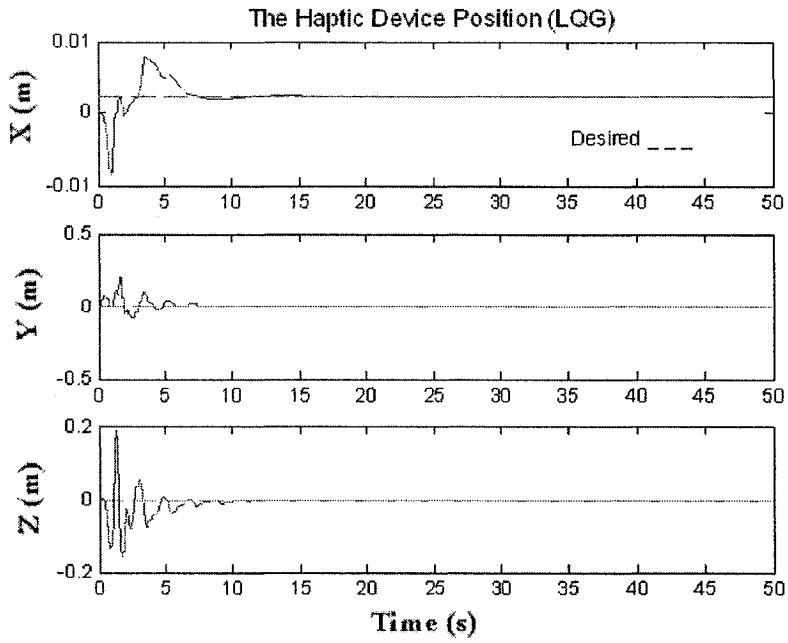

Figure 5.2: Response of the nonlinear model using the LQG controller

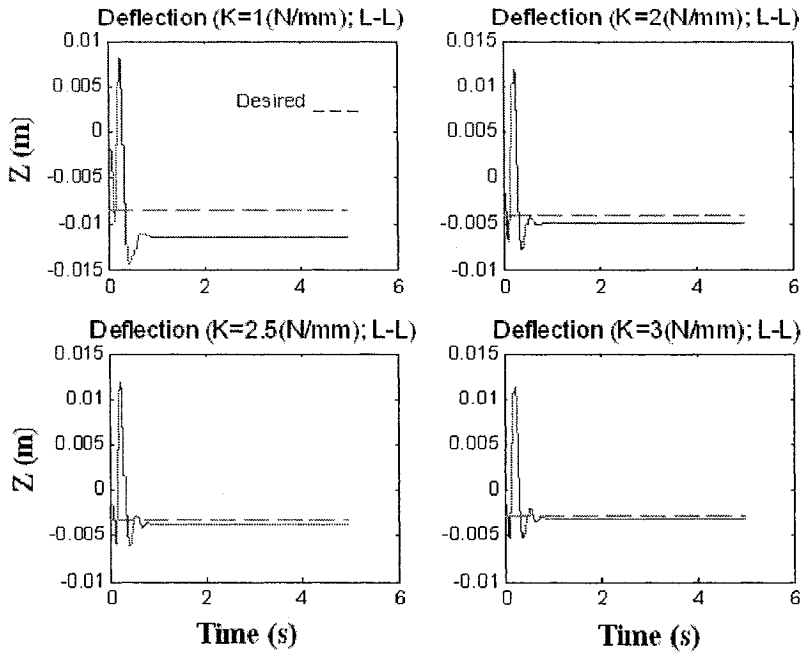

Figure 5.3: Deflection of deformable objects with different stiffness using lead-lag controller

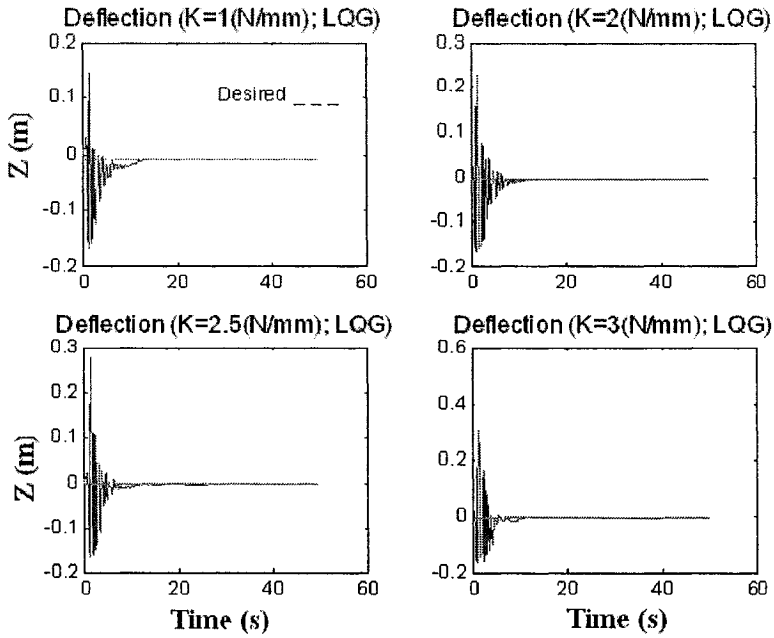

Figure 5.4: Deflection of deformable objects with different stiffness using LQG controller

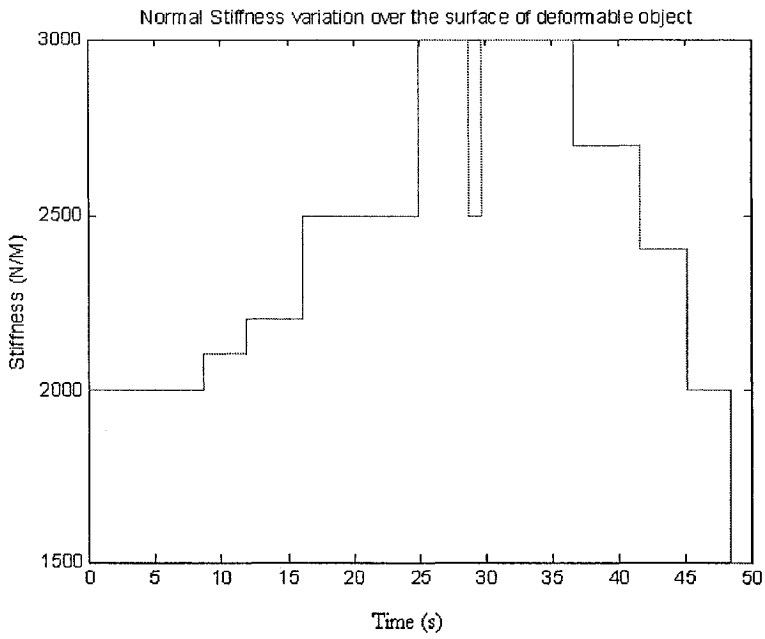

Figure 5.5: Normal stiffness of adjacent polygonal meshes throughout the trajectory in the Figure 5.7 over the surface of the deformable object

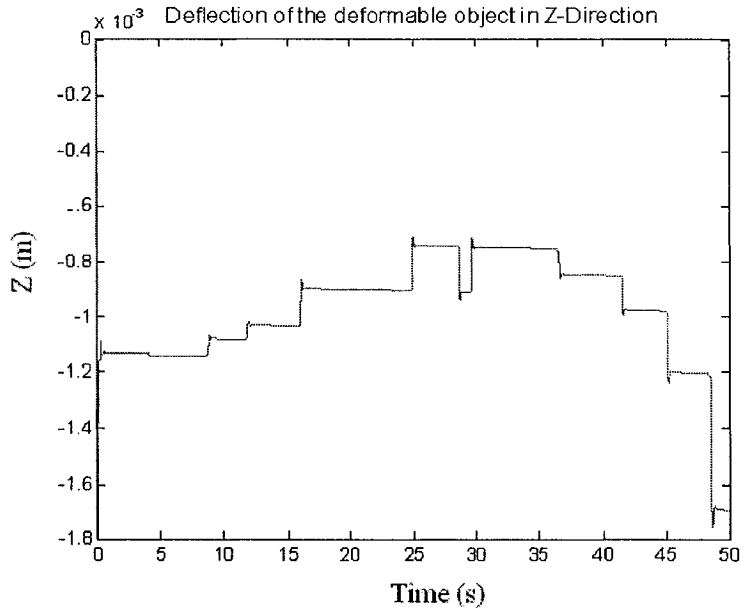

Figure 5.6: Deflection on the surface of deformable object with normal stiffness in Figure 5.5.

5.6 Discussion

Based on the simulation results presented above, the LQG compensator shows a good performance with respect to the steady state error requirement. Although it has achieved a poor transient response for the nonlinear model, the LQG control scheme is sufficiently robust to satisfy the steady state error design objectives that are indicated in Table 5.1. As shown in Figure 5.4, the closed loop control system using the LQG compensator maintains almost a zero steady state error to interact with deformable objects with different stiffnesses. This controller does perform also well for low stiffness (1 N/mm) and the maximum stiffness (3.5 N/mm). The closed loop control system using the lead-lag controller as seen in Figure 5.3 indicates that there are some steady state errors corresponding to the low stiffness deformable objects and that is mostly because the controller was tuned for a 3.5 N/mm stiffness deformable objects. However, the compensator's transient response is acceptable. Furthermore, the haptic system shows (Figures 5.6 and 5.7) an absolute stable behavior in sliding on the surface of the deformable object with small and large variations of the discrete normal stiffness for adjacent polygonal meshes in Figure 5.5. As shown in Figures 5.6 and 5.9, in the case of a large difference between the normal forces (stiffness), transient response plays an important role for having a smooth transient from one polygon to its neighbor. The LQG controller needs to be adjusted to obtain a better transient response. Subsequently, it can be used for the purpose of sliding on the surface of a deformable object.

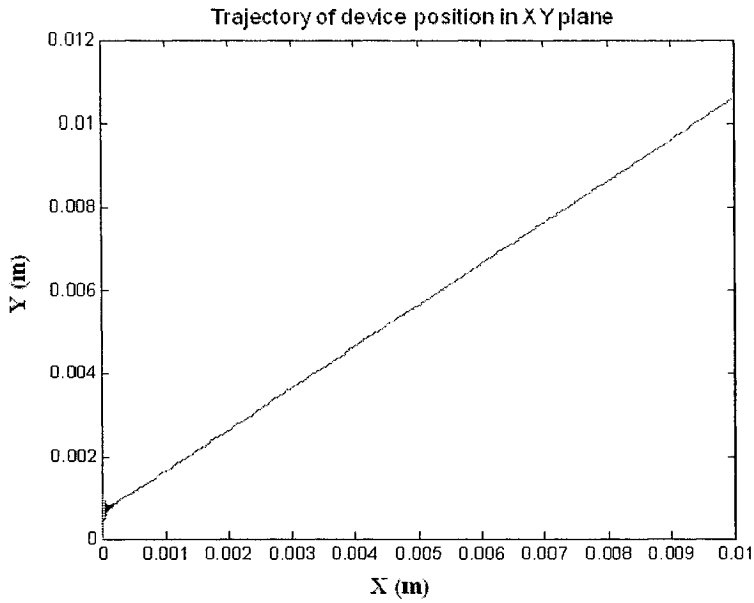

Figure 5.7: Trajectory of the device position over the surface of the deformable object (a cube)

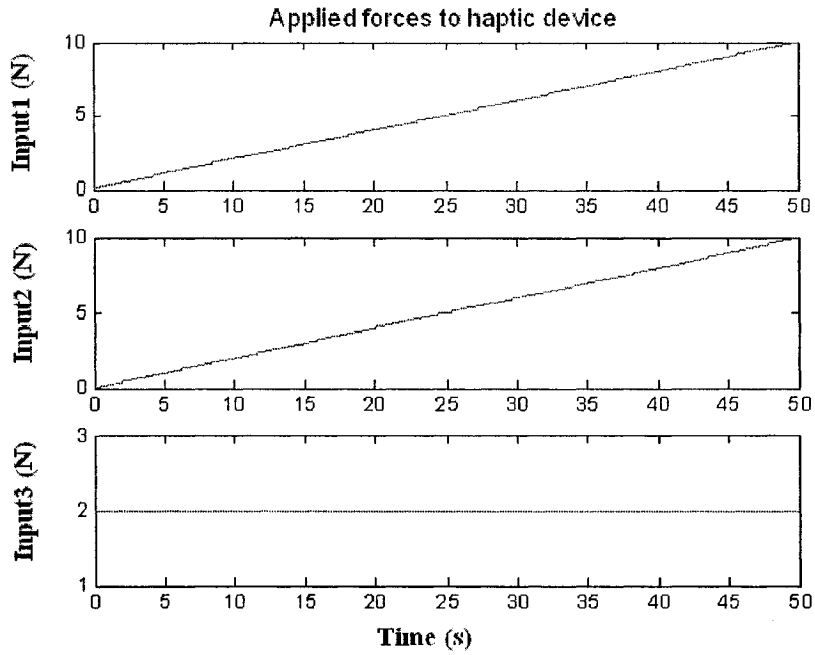

Figure 5.8: Applied forces on the haptic device

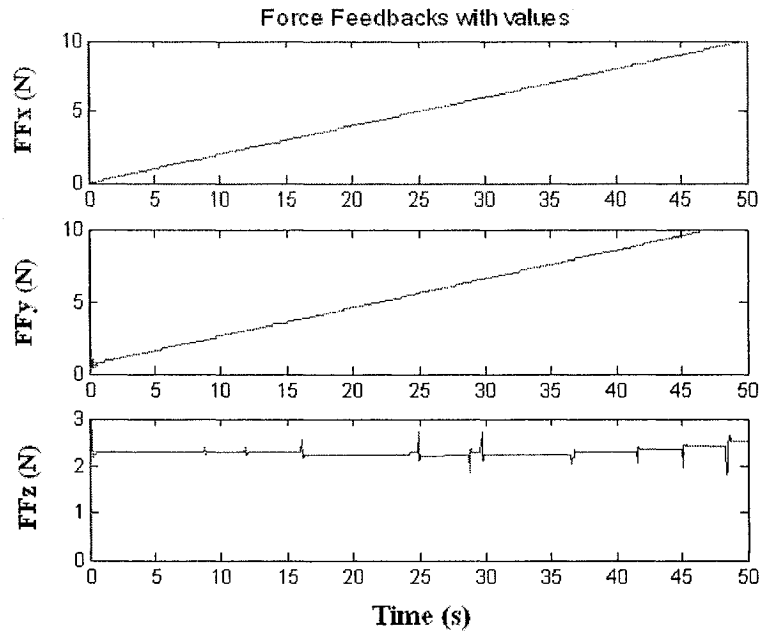

Figure 5.9: Force feedback in different directions of X, Y and Z, separately

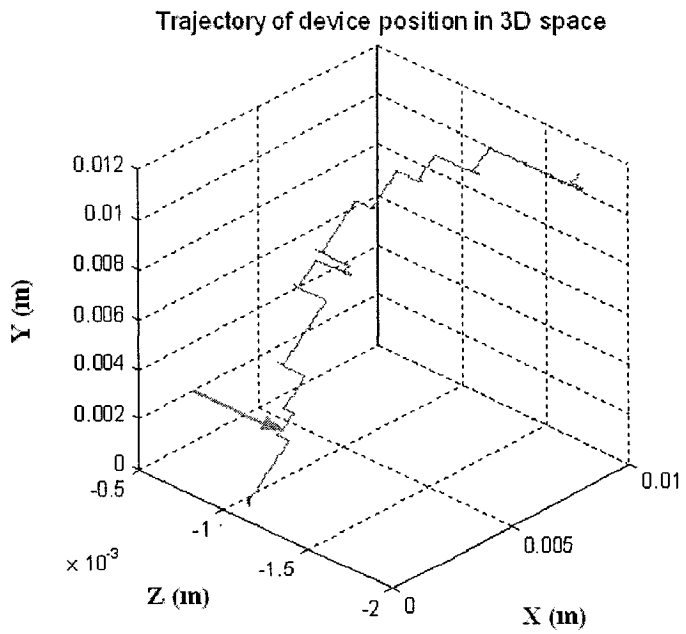

Figure 5.10: The trajectory of the haptic point from a view point behind the deformable object to depict the deflection X (m)

5.7 Conclusions

In this chapter, we have shown that our proposed method can ensure and maintain desirable forces on the deformable object surface. Also, the method guarantees a stable contact during sliding over the deformable object with discrete normal forces for a typical polygonal mesh deformable object. However, the LQG compensator design requires to be investigated further in order to achieve improved transient responses. Also the design of the lead-lag controller could be made more complicated instead of using only a simple first order compensator structure to improve the steady state error. Extending the proposed methods to sliding on the deformable surfaces with less friction forces (tangential stiffness) and to cover a continuous force field for checking the smoothness of the feeling on traversing polygonal meshes with large deformations are the topics of our future research.

Chapter 6

CONCLUSION

In order to utilize the PHANToM™ Premium 1.5A Haptic Device, its kinematics, Jacobian and motion equations were determined and a nonlinear open loop model was developed. The stability of the haptic system was investigated at its equilibrium points. The open loop model responses were not bounded and/or did not converge to the equilibrium points. To achieve a stable haptic display, a pre-closed loop model was presented by adding friction (damping factors) to the nonlinear open loop model of the haptic device. The resulting estimated device friction (damping) factors were fixed in the mathematical nonlinear model. The steady state response of the system with these damping parameters has converged to the set of equilibrium points and the enhanced (contributed) model of the PHANToM™ showed a stable behavior corresponding to these points. Consequently, our first contribution was in the estimation of the friction coefficients which can be considered as a set of valid parameters for the haptic loop with the mathematical nonlinear PHANToM™ model. The second contribution is that it was shown that the linearized and integrated model of the system along with the proposed force/position control design strategies can ensure and maintain desirable forces subject to interaction with virtual deformable objects. However, one of the proposed control schemes, namely the LQG controller design requires further investigation to achieve improved transient responses. The design of the lead-lag controller could also be made more complicated instead of using

only a simple first order compensator structure to improve the steady state error performance. These extensions are the topics of our future research. The third contribution deals with demonstrating that our proposed technique ensures and maintains desirable forces on the deformable object surface and guarantees a stable contact during sliding over the deformable object with discrete normal forces for a typical polygonal mesh deformable object. Moreover, extending the method for sliding on the deformable surfaces with less friction forces (tangential stiffness) and also generalizing the proposed technique to cover a continuous force field for checking the smoothness of the feeling on traversing polygonal meshes with large deformation are the topics of our future research.

BIBLIOGRAPHY

[1] Sensable Technologies Inc. http://www.sensable.com, (current FEB. 24, 2004)

[2] PHANToM™ PREMIUM 1.0A/1.5A Hardware Installation and Technical Manual, 1993-1999, SensAble Technologies, Inc.

[3] Cavusoglu, M. C., & Feygin, D. (2001). *Kinematics and dynamics of PHANToM(TM) model 1.5 haptic interface* (Tech. Rep.). University of California at Berkeley, Electronics Research aboratory Memo M01/15.

[4] Zilles C.B. and Salisbury J.K., "A Constraint-based God-object Method for Haptic Display," Proc.IEEE/RSJ int. Conf. on Intelligent Robots and Systems, Pittsburgh, PA, 1995, pp. 146-151.

[5] Cavusoglu M.C., Feygin D., and Tendick F., ``A Critical Study of the Mechanical and Electrical Properties of the PHANToM Haptic Interface and Improvements for High Performance Control," *Presence: Teleoperators and Virtual Environments*, vol. 11, no. 6, pp. 555-568, Dec. 2002.

[6] Robust Control Toolbox User's Guide, version 2, The MathWorks, Inc.

[7] GHOST SDK Programmer's Guide, version 4.0, SensAble Technologies, Inc. Rev. 1.5 4/23/02.

[8] Salisbury, K., Brock, D., Massie T., Swarup, N., Zilles, C. 1995. Haptic Rendering : Programming Touch Interaction with Virtual Objects. Proc. Symposium on Interactive 3D Graphics, ACM. pp. 123-130.

[9] Wu, X., Downes, M. S., Goktekin, T., Tendick, F. 2001. Adaptive Nonlinear Finite Elements for Deformable Body Simulation Using Dynamic Progressive Meshes. Proc. Eurographics 2001,Vol. 20, No. 3, pp. 349-58.

[10] Zhuang, Y., Canny, J. 2000. Haptic Interaction with Global Deformations. Proc. IEEE International Conference on Robotics and Automation, pp. 2428-2433.

[11] D'Aulignac, D., Balaniuk, R., Laugier, C. 2000. A Haptic Interface for a Virtual Exam of the Human Thigh. Proc. IEEE International Conference on Robotics and Automation, pp.2452-2457.

[12] Debunne, G., Desbrun, M., Cani, M., Barr, A. 2001. Dynamic Real-Time Deformations Using Space and Time Adaptive Sampling. SIGGRAPH, Computer Graphics and Interactive Tech-niques, ACM Press, pp. 31-36.

[13] Cotin, S., Delingette, H., Ayache, N. 1999. Real-time Elastic Deformations of Soft Tissues for Surgery Simulation. IEEE Transactions on Visualization and Computer Graphics, Vol. 5:1, pp.62-73.

[14] Delingette, H., Cotin, S., Ayache, N. 1999. A Hybrid Elastic Model Allowing Real-time Cutting, Deformations and Force-feedback for Surgery Training and Simulation. Computer Animation Proceedings, pp. 70-81.

[15] James, D. L., Pai D. K. 2001. A Unified Treatment of Elastostatic and Rigid Contact Simulation for Real Time Haptics. Haptics-e, the Electronic Journal of Haptics Research, Vol. 2, No. 1.

[16] Mazzella, F., Montgomery, K., and Latombe, J.-C. 2002. The Forcegrid: A Buffer Structure for Haptic Interaction with Virtual Elastic Objects. Proc. IEEE Int. Conf. on Robotics and Automation, pp. 939-946.

[17] Bro-Nielsen, M. 1998. Finite Element Modeling in Surgery Simulation. Proceedings of the IEEE, 86:3, pp. 490-503.

[18] Astley, O., Hayward, V. 1997. Real-Time Finite-Elements Simulation Of General Visco-Elastic Materials For Haptic Presentation. Proc. IROS'97 1997 IEEE/RSJ Int. Conf. on Intelligent Robotics and Systems, Workshop on Dynamic Simulation: Methods and Applications. pp. 52-57.

[19] Zachmann, G., "Real-time and Exact Collision Detection for Interactive Virtual Prototyping", Proceedings of the Design Engineering Technical Conference (DETC) 1997, Sacramento, CA, Sept. 14-17, 1997.

[20] Gottschalk, S., et al., "OBBTree: A Hierarchical Structure for Rapid Interference Detection", Proceedings of SIGGRAPH 96, New Orleans, Aug. 4-9, 1996, pp.171-180.

[21] Lawrence D.A., Pao L.Y., Salada M.A. and Dougherty A.M. "Quantitative Experimental Analysis of Transparency and Stability in Haptic Interfaces" Proceedings of the ASME International Mechanical Engineering Conference and Exposition, DSC-Vol. 58, Atlanta, GA, Nov 17-22, 1996.pp. 441-449.

[22] Lee C.D., Lawrence D.A.and Pao L.Y., "A High-Bandwith Force-Controlled Haptic Interface", Proceedings of the ASME International Mechanical Engineering Conference and Exposition, DSC-Vol. 69-2, Orlando, FL, Nov 5-10, 2000. pp. 1299-1308.

[23] Lawrence D., "Stability and Transparency in Bilateral Teleoperation", IEEE Transactions on Robotics and Automation, Vol. 9, No. 5, October 1993.

[24] Hayward Vincent and Astley Oliver R., "Performance Measures for Haptic Interfaces", Robotics research: the seventh international symposium/Georges Giralt and Gerhard Hirzinger, eds. 1996, pp. 195-207.

[25] Hashtrudi-Zaad K.and Salcudean S.E., "On the use of local force feedback in transparent teleoperation," Proceedings of IEEE International Conference on Robotrics and Automation, pp. 1863-1869,1999.

[26] Colgate J.E., Brown J.M., "Factors Affecting the Z-width of a Haptic Display", Proceeding of the IEEE Int'l Conf. Robotics and Automation 1994., Pp. 3205 –3210

[27] Colgate J.E., et al., "Implementation of Stiff Virtual Walls in Force-Reflecting Interfaces", Virtual Reality Annual International Symposium, 1993., IEEE. Pp. 202 –208

[28] Miller B.E., Colgate J.E., Freeman R.A., "Guaranteed Stability of Haptic Systems with Nonlinear Virtual Environments", IEEE Transactions on Robotics and Automation, September 1999.

[29] Gillespie B. and Cutkosky M.. "Stable User-Specific Rendering of the Virtual Wall," Proceedings of the ASME International Mechanical Engineering Conference and Exposition, DSC-Vol. 58, Atlanta, GA, Nov 17-22, 1996. pp. 397-406.

[30] Ellis R.E., Sarkar N., and Jenkins M.A., "Numerical Methods for The Haptic Presentation of Contact: Theory, Simulations, and Experiments", Proceedings of the ASME International Mechanical Engineering Conference and Exposition, DSC-Vol. 58, Atlanta, GA, Nov 17-22, 1996. pp. 413-420.

[31] Murat Cenk Cavusoglu and Frank Tendick, "Multirate Simulation of High Fidelity Haptic Interaction with Deformable Objects in Virtual Environments", Proceeding of the IEEE Int'l Conf. Robotics and Automation 2000., Pp. 2458 –2465

[32] Luecke G.R., Chai Young-Ho, "Stability and Performance Comparison of the Force Reflecting Haptic Manipulator", Advanced Robotics, 1997. ICAR '97. Proceedings., 8th International Conference.

[33] Prisco G.M., et.al, "Haptic Control of the Hand Force Feedback System", Proceedings of SPIE, Telemanipulator and Telepresence Technologies VI, 1999.

[34] Love Lonnie and Book Wayne, "Contact Stability Analysis of Virtual Walls", Proceedings of the 1995 ASME International Mechanical Engineering Conference and Exposition, DSC-Vol. 57-2. pp. 689-694.

[35] Gibson, S., Mirtich, B. 1997. A Survey of Deformable Modeling in Computer Graphics. *Tech. Rep. TR97-19*, Mitsubishi Electronic research Laboratories, Cambridge,MA.

[36] Fung, Y. C., 1977. *A First Course in Continuum Mechanics* 2nd Ed. Prentice-hall,Englewood Cliffs, New Jersey.

[37] Raamachandran, J. 2000. *Boundary and Finite Elements.* Narosa Publishing House,New Dehli.

[38] James, D. L., Pai, D. K. 1999. ArtDefo, Accurate Real Time Deformable Objects.*SIGGRAPH 99 Conference Proceedings*. pp. 65–72.

[39] Basdogan C., Ho, C., Srinivasan, M.A., Small, S., Dawson, S., 1998, "Force interactions in laparoscopic simulations: haptic rendering of soft tissues" *Medicine*

Meets Virtual Reality (MMVR'6) Conference, pp.385-391, San Diego, CA, January 19-22.

[40] Adams R.J., Klowden Daniel and Hannaford B.,"Stable Haptic Interaction Using the Excalibur Force Display", Proceedings of the 2000 IEEE, International Conference on Robotics & Automation. April 2000.

[41] Adams R.J. and Hannaford B., "Stable Haptic Interaction with Virtual Environments", IEEE Transactions on Robotics and Automation, Vol. 15, No. 3, June 1999.

[42] Adams R.J., Moreyra M.R. and Hannaford B.. "Stability and Performance of Haptic Displays: Theory and Experiments", Proceedings of the ASME International Mechanical Engineering Conference and Exposition, DSC-Vol. 64, 1998. pp. 227-234.

[43] Adams R.J. and Hannaford B., "A Two-Port Framework for the Design of Unconditionally Stable Haptic Interfaces", Proceedings of the IEEE International Conference on Intelligent Robots and Systems, Victoria, B.C. Canada. October 1998.

[44] Brogan W. L. *Modern Control Theory.* Prentice-Hall, Englewood Cli#s, NJ, third edition, 1990.

[45] System Identification Toolbox User's Guide, version 6, The MathWorks, Inc.

[46] Barbagli F., Prattichizzo D., Salisbury K., "Multirate analysis of Haptic Interaction Stability with Deformable Objects", in the Proceedings of the 41st IEEE Conference on Decision and Control, Las Vegas, Nevada, December 2002, pag 917-922.

[47] Spong, M. W. and Vidyasagar, M. Robot dynamics and control. J. Wiley, 1989.

[48] Massie Thomas H., Salisbury J.K.,The PHANToM haptic interface: A device for probing virtual objects, Proceedings of the ASME winter annual meeting, Symposium on haptic interfaces for VE and teleoperator systems, Chicago, IL, Nov 1994.

Appendix A

This appendix contains the detailed schematic layout of the block diagrams in Simulink for the various haptic system models throughout the report.

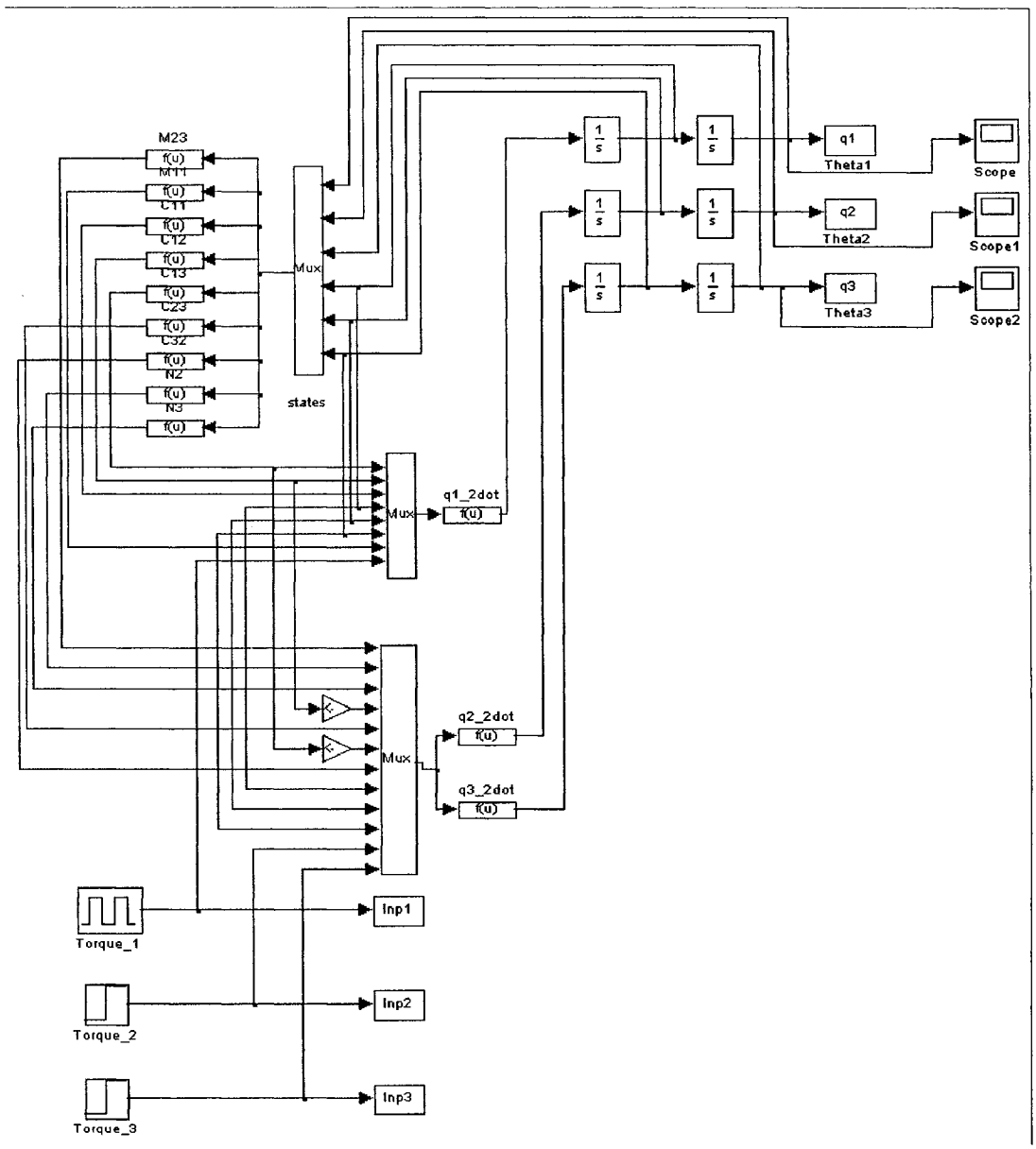

Figure A.1: Simulated model of the PHANToM™ haptic device in Figure 2.10 using Simulink.

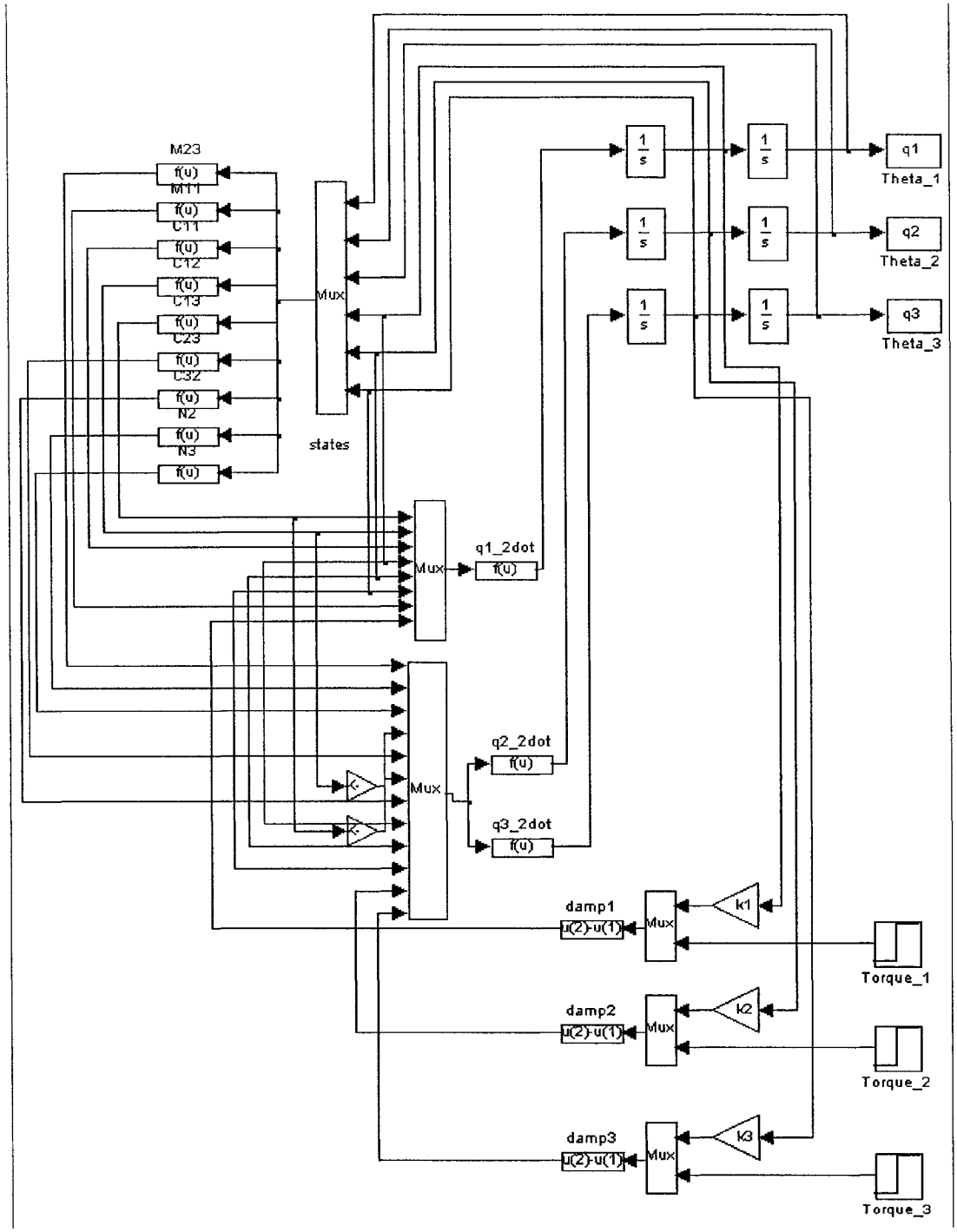

Figure A.2: Simulated model of PHANToM™ with damping factors in Figure 3.1 using Simulink.

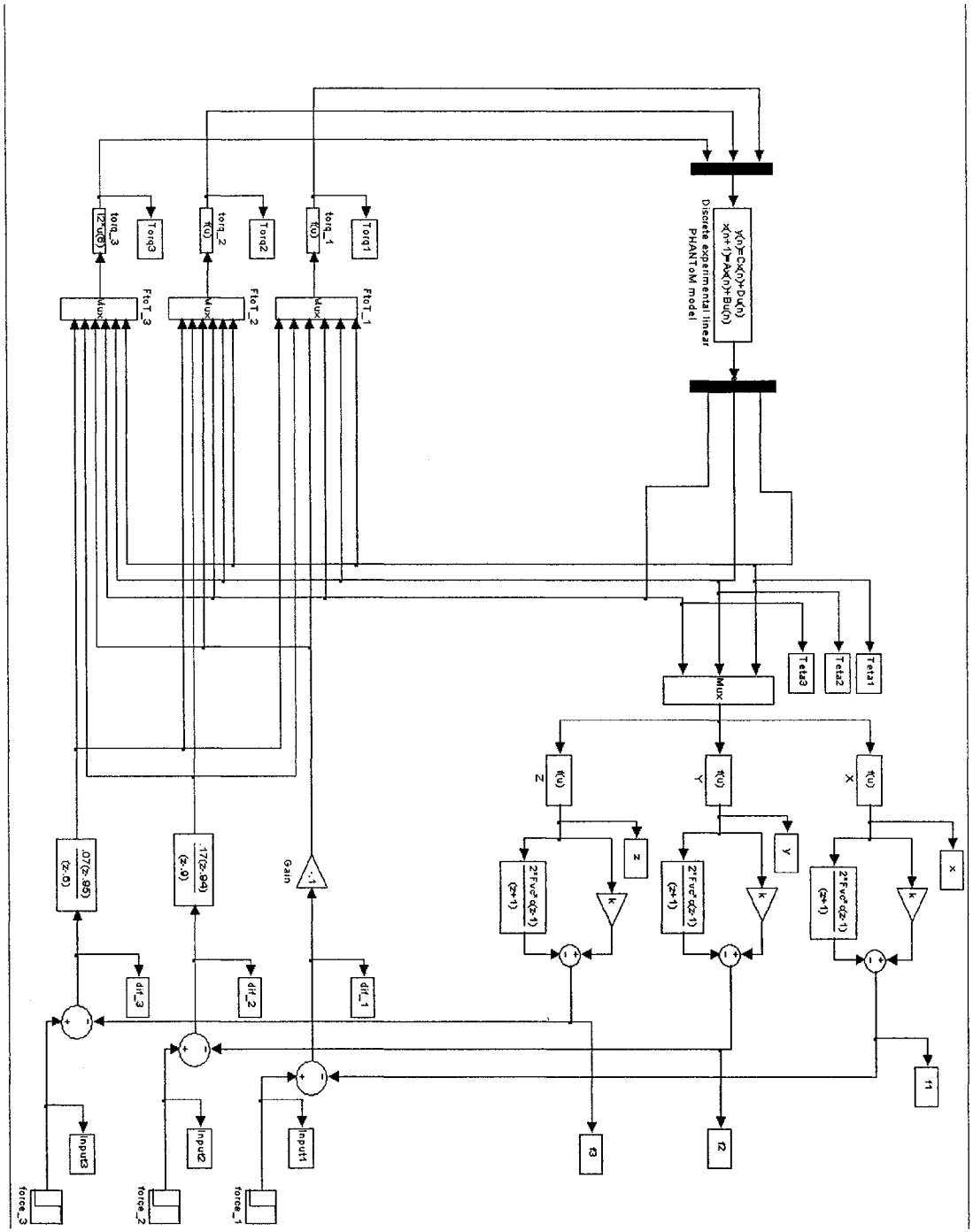

Figure A.3: The Position/Force feedback control loop with experimental linear haptic device model in Figure 3.3 using Simulink.

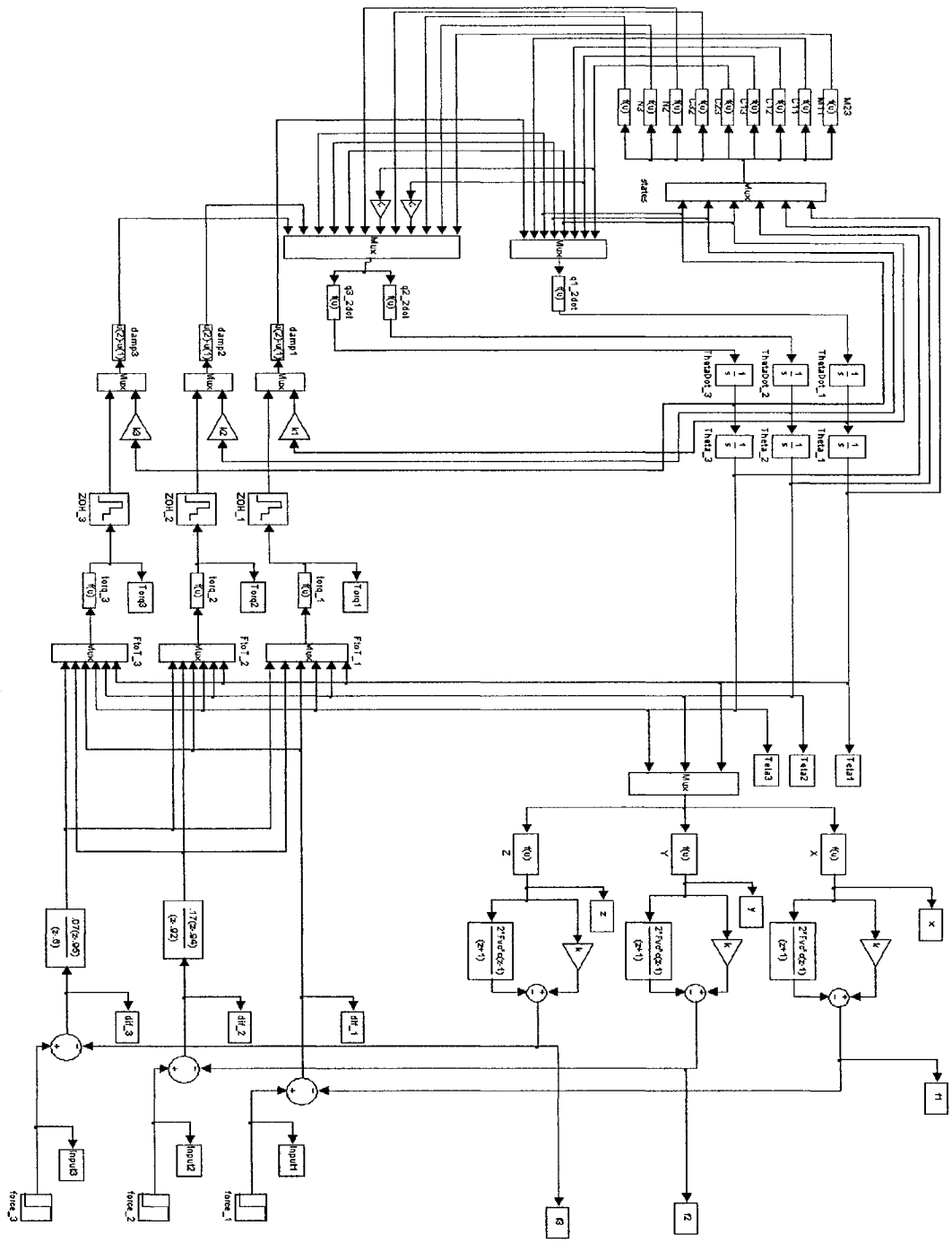

Figure A.4: The Position/Force feedback control loop with the mathematical nonlinear haptic device model in Figure 3.4 using Simulink.

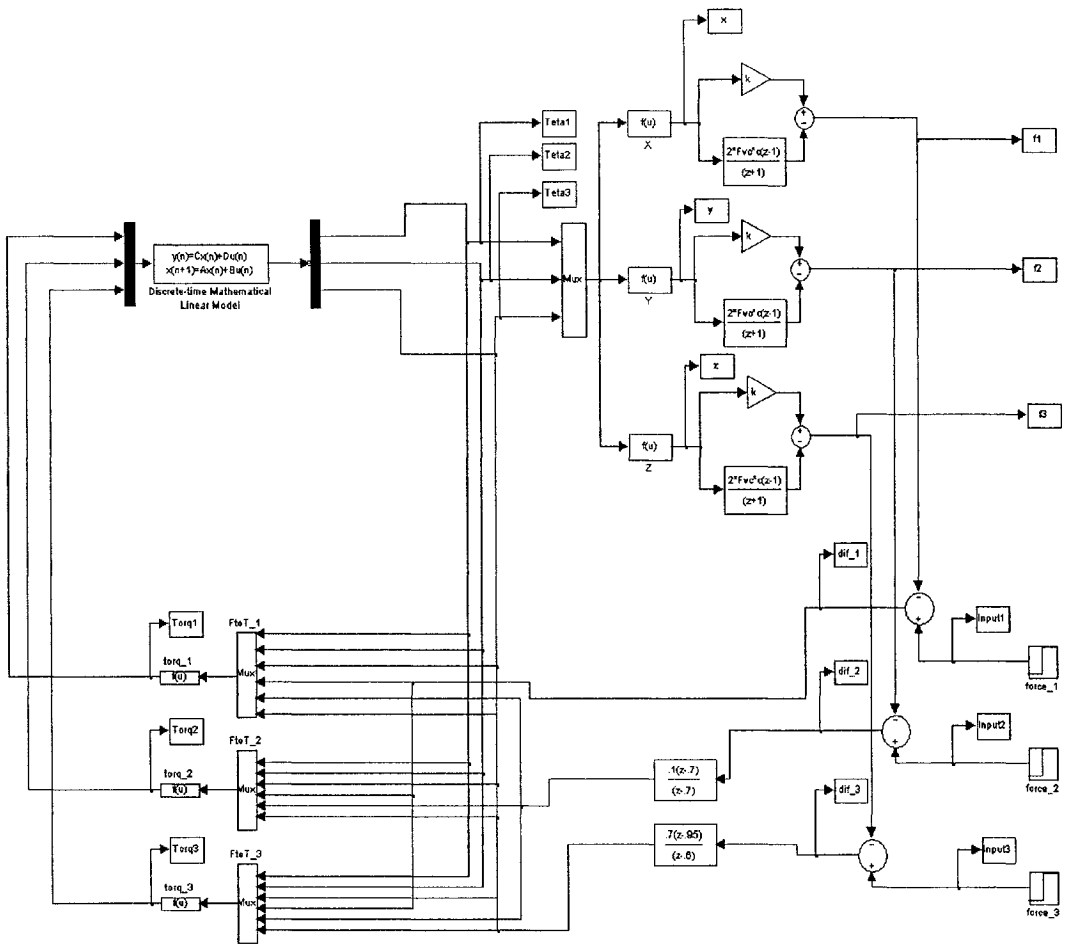

Figure A.5: The Position/Force feedback control loop with the mathematical linear haptic device model in case B and lead-lag controller in Figure 3.7 using simulink.

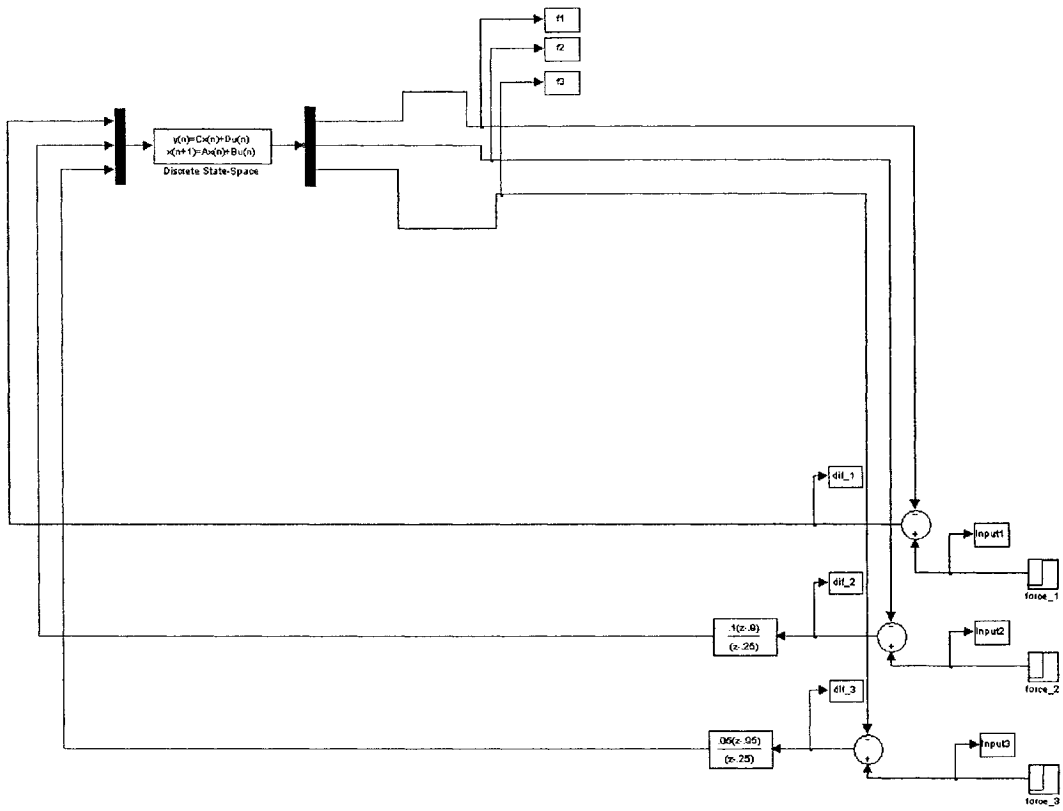

Figure A.6: The Position/Force feedback control loop with the linear model in case C and Lead-Lag controller in Figure 3.8 using simulink.

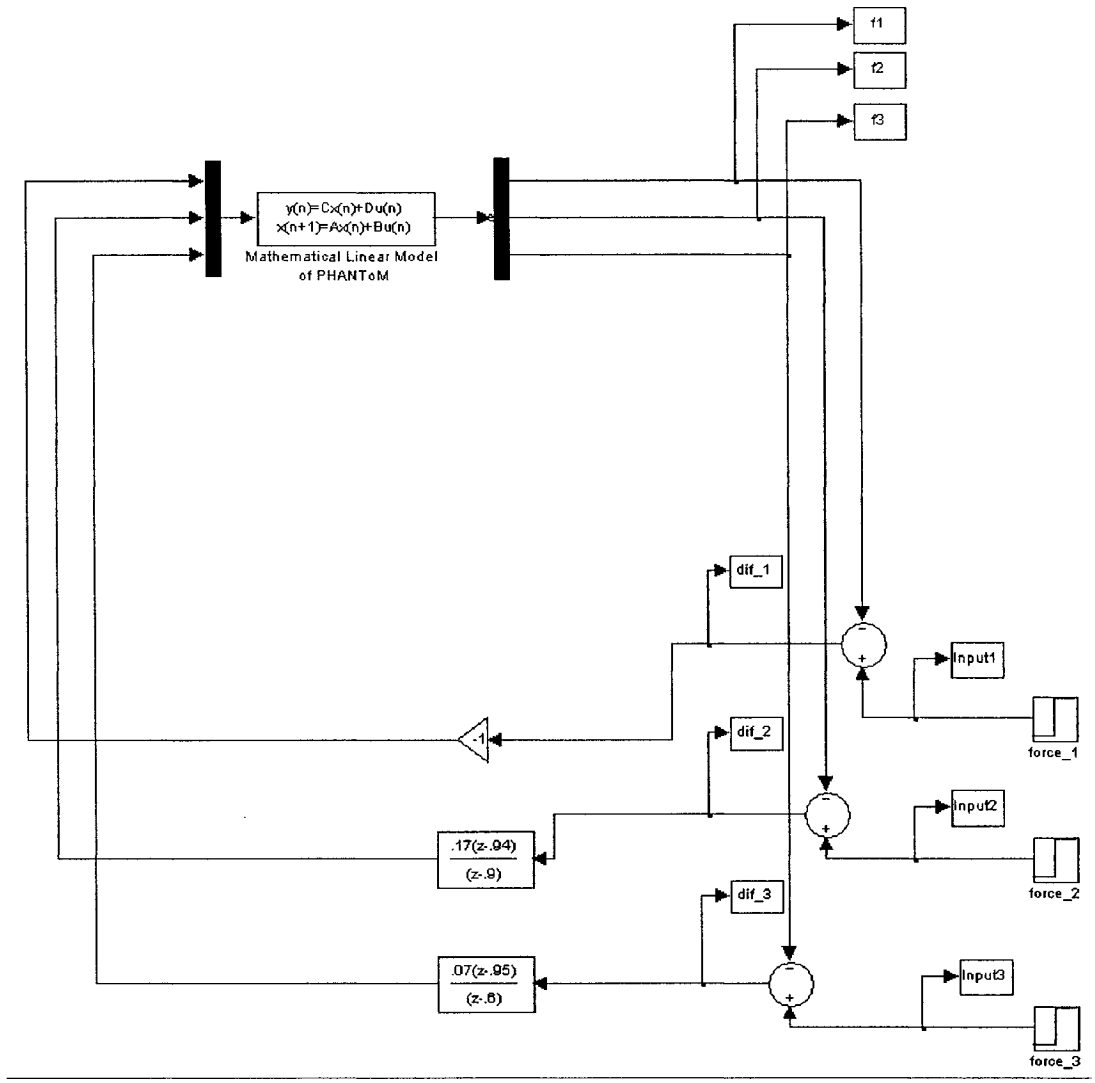

Figure A.7: The Position/Force feedback control loop with the linear model in case D and Lead-Lag controller in Figure 3.9 using simulink.

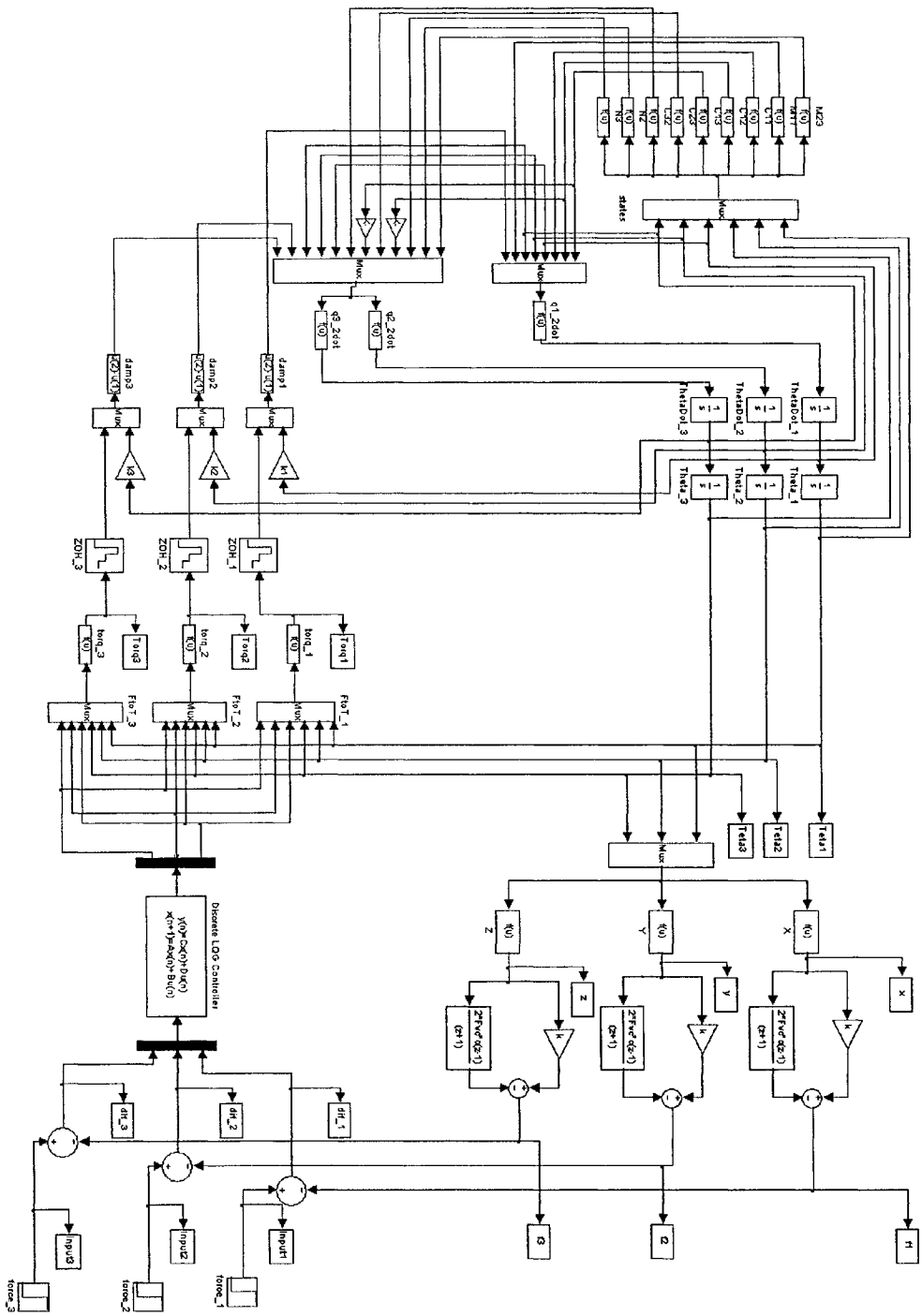

Figure A.8: The Position/Force feedback control loop with the mathematical nonlinear model and LQG controller in Figure 4.2 using Simulink.

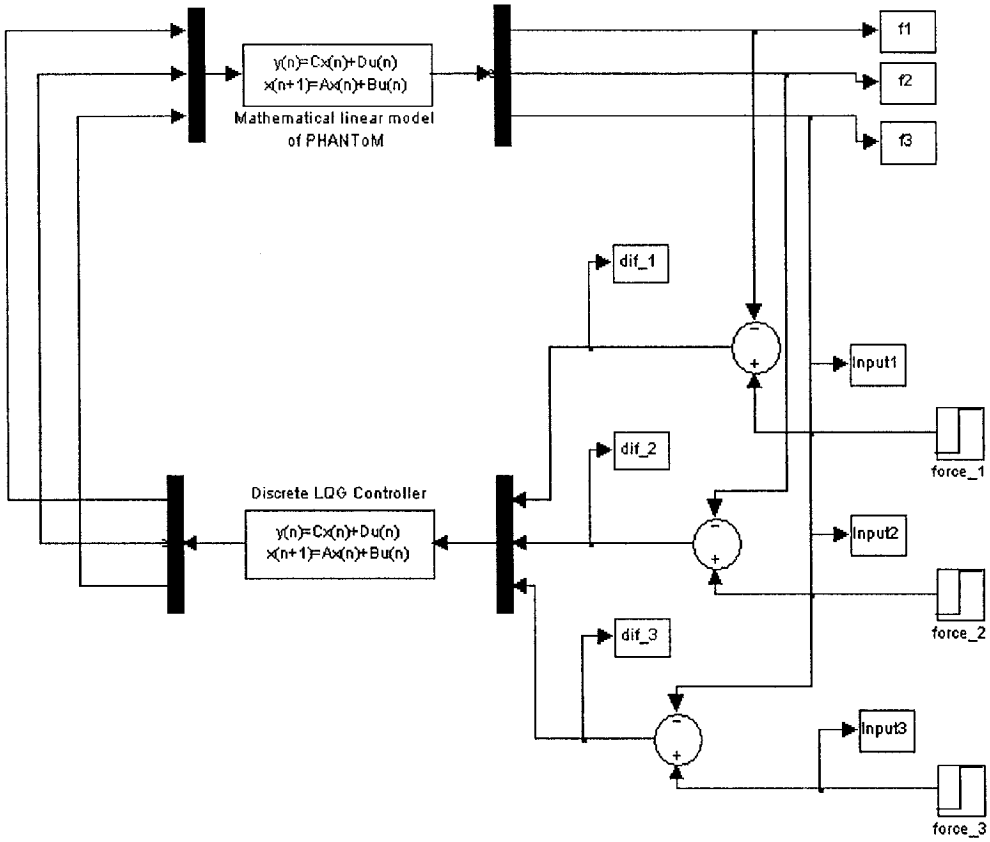

Figure A.9: The Position/Force feedback control loop with the mathematical linear model and LQG controller in Figure 4.3 using Simulink.